POLITECNICO
MILANO 1863

Synthesis, Structural Characterization and Photo-physical Properties of 1D Lead Halide Perovskites Based on Imidazolium Cation

Author: **Davide Ricci**

Student ID: 944189
Advisor: Gabriella Cavallo
Co-advisor: Federico Bella
Academic Year: 2020-21
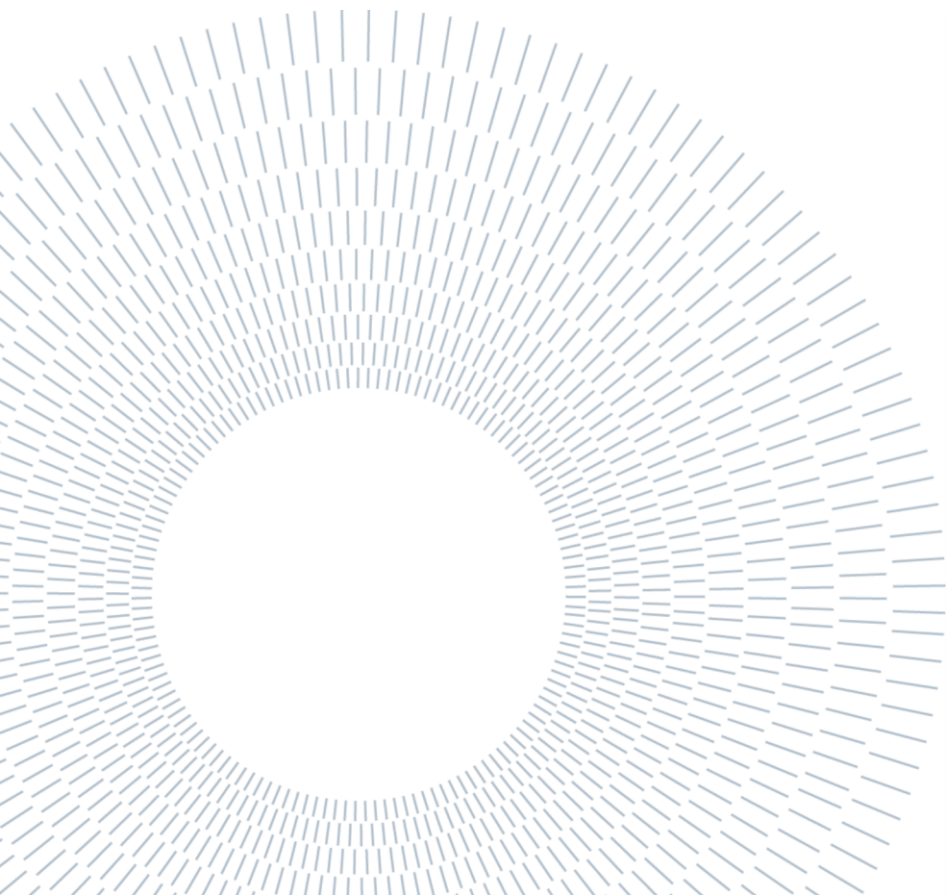
A Tullio e Gianna.

Abstract

Low dimensional hybrid halide perovskites (LDHPs) have emerged as a promising alternative to 3D perovskites for optoelectronic applications. LDHPs show improved environmental stability than 3D HPs and the alternating arrangement of organic and inorganic domains endows LDHPs with unique quantum and dielectric confinement effects and self-trapped excitons. In particular 1D perovskites were investigated as phosphors in optically pumped LED, thanks to tunable bandgap and broad emission. These properties can be further tuned by selecting organic cations with appropriate steric hindrance and specific functional groups able to be involved in interactions with inorganic domains. In this respect fluorination has been exploited to control HOMO-LUMO level and bandgap of HPs. Moreover, the hydrophobicity offered by fluorinated tails gives protection against humidity, boosting material stability. However, conjugated cations containing fluorinated alkyl chains have not been applied yet for the construction of LDHPs. In this work imidazolium cations functionalized with perfluoroalkyl chains of different length were applied for the construction of new LDHPs. Their synthesis and characterization allowed to study effects of perfluoroalkyl chains on structure and properties of perovskites. LDHPs containing 1-methyl- 3-alkyl-imidazolium cations have been also synthesized as comparison. FTIR, TGA and XRD confirmed the incorporation of imidazolium cations in the inorganic framework, suggesting the formation of 1D structures. This was further supported by PL emission. Interestingly, polarized optical microscopy revealed a liquid crystalline behavior for perovskite containing imidazolium with long fluorinated chains suggesting that *fluorous-fluorous* interactions and segregation of fluorinated moieties induce the formation of ordered structures. Finally, perovskite coating was found hydrophobic for fluorinated chains. This property is interesting in terms of moisture resistance.

Key-words: Low dimensional perovskites, Imidazolium cations, lead iodide, optical characterization, structural characterization, perfluoroalkyl chains

Abstract in lingua italiana

Le perovskiti alogenuri ibride a bassa dimensionalità (LDHP) sono emerse come alternativa più stabile per le loro controparti 3D per applicazioni optoelettroniche. Le LDHP mostrano una migliore stabilità ambientale rispetto alle 3D, e l'alternanza tra domini organici e inorganici fornisce alle LDHP effetti di confinamento quantico e dielettrico e alla creazione di eccitoni *self-trapped*. In particolare, le perovskiti 1D sono state investigate come emettitori in LED pompati otticamente, grazie a diversi valori di gap di banda e un largo spettro di emission. Queste proprietà possono essere modificate selezionando cationi organici con opportuni ingombro sterico e gruppi funzionali in grado di interagire con la parte inorganica. La fluorurazione di questi cationi è stata sfruttata per controllare i livelli *HOMO* e *LUMO* e il gap di banda delle HP. Inoltre, l'idrofobicità offerta dalle catene fluorurate offre protezione contro l'umidità, migliorandone la stabilità. Tuttavia, cationi coniugati contenenti catene fluorurate non sono stati applicati per la creazione di perovskiti. In questo lavoro cationi imidazolio funzionalizzati con catene perfluoroalchiliche sono stati utilizzati per la creazione di LDHP. La sintesi e la caratterizzazione di queste perovskiti hanno permesso di studiare l'effetto delle catene perfluoroalchiliche in termini di struttura e proprietà. LDHP contenenti 1-metil-3-alchil-imidazolio sono state sintetizzate come confronto. FTIR, TGA and XRD hanno confermato l'incorporazione dei cationi di imidazolio nel reticolo, suggerendo una struttura 1D. Ciò è stato confermato anche dalle misure di PL. Le misure attraverso il microscopio ottico polarizzato hanno mostrato per le perovskiti con cationi aventi lunghe catene perfluoroalchiliche un comportamento liquido cristallino, suggerendo interazioni fluoro-fluoro e la segregazione delle catene perfluoroalchiliche che ha indotto la formazione di una struttura ordinata. Infine, i rivestimenti con perovskiti con catene fluorurate hanno mostrato un comportamento idrofobico, proprietà interessante in termini di resistenza all'umidità.

Parole chiave: Perovskiti a bassa dimensione, cationi di imidazolio, ioduro di piombo, caratterizzazione ottica, caratterizzazione strutturale, catene perfluoroalchiliche

Contents

1. Introduction

1.1 Perovskite materials

Perovskite materials raised increasing interest in recent studies thanks to their outstanding optical properties. They are under investigation for conversion between light and electrical energy: in literature examples of conversion can be found from light to energy and vice versa, with solar cells, photodetectors, and light emitting diodes.[1]

The name perovskite comes from Perovski, the name of a Russian mineral collector, who found a calcium titanium oxide mineral ($CaTiO_3$) with the called "perovskite structure". This material has an ideal cubic structure (space group Pm3m), with possible tetragonal and orthorhombic variants. This structure is composed by TiO cubic lattice that act as anion, combined with Ca2+ cations. In general, Perovskites have ABX_3 formula, where A and B are cations – generally A larger than B - and X is an anion. All other synthetic crystals with this formula are called perovskites.[2]

The ideal cubic structure (shown in Figure 1.1**Errore. L'origine riferimento non è stata trovata.**) has the B cation in 6-fold coordination, surrounded by an octahedron of anions, and the A cation in 12-fold cubo-octahedral coordination. [2]

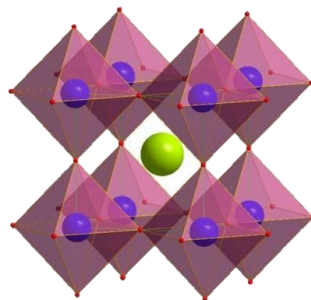Figure 1.1 Schematic 3D representation of the ideal cubic structure of the perovskite crystal cell: blue = B cation, red = X anion, green = A cation.

Perovskites, according to classification proposed from Gao et al.[2] shown in Figure 1.2, can be classified according to their composition: when oxygen act as X anion perovskites are defined as "inorganic oxide perovskites" (ABO_3), since they are

obtained only with inorganic A cations. In other cases, when halogen atoms occupy X sites, perovskites are defined as "halide perovskites (HP)" (ABX₃). These last perovskites are the focus of this work. They have B sites occupied from IV group elements like germanium, tin, or lead. The A cation is a I group element, like potassium, rubidium, or cesium – giving the name of "alkali-halide perovskites" – or an organic molecule – providing "hybrid organic-inorganic halide perovskites". [2]

Perovskite crystalline system

Inorganic oxide perovskites (AMO₃) (BaTiO₂, CaTiO₃)

Halide perovskites (ABX₃)

Alkali-halide perovksites CsPbI₃
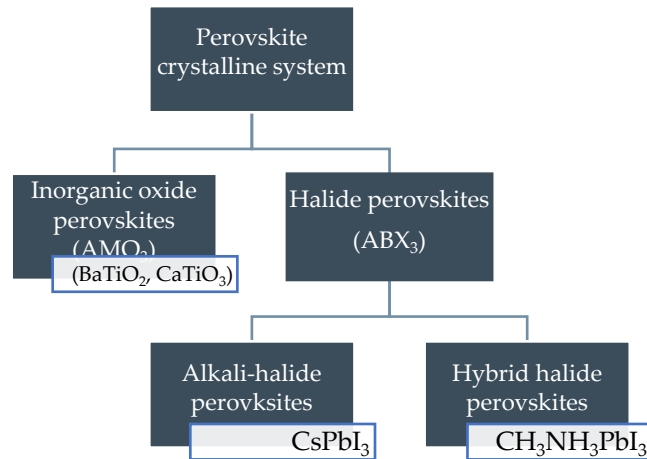
Hybrid halide perovksites CH₃NH₃PbI₃

Figure 1.2. Classification of perovskites based on their composition.

The choice of each of these elements will influence the structure and consequently the properties of the material. For example, selecting a smaller and more electronegative halogen, as X (among Cl, Br and I) will induce a decrease in the lattice parameter and a more ionic character in the B-X bond. So, the electron cloud is less dispersed along the bond and more localized close to the nuclei: this electronic distribution results in shorter bond lengths and higher band gaps with less dispersive electronic band structure close to the band edge. [3] On the opposite, bigger and less electronegative atoms, like Iodine, decrease band gap thanks to more covalent character of B-X bond. Whereas tuning B cation (for example from germanium to tin to lead) increases oxidated state stability. Indeed, lead is typically preferred in terms of stability of the material and efficiency of the device, but it gives concerns about toxicity. So, germanium or tin have been studied as lead-free alternative to conventional perovskites, trying to obtain similar performances. [4]

Finally, A cation is the more tunable component, and it can bring the biggest modifications in terms of structure and properties. For example - as described in the following chapter - it has effect on stability (one of the main concerns about perovskites), on band structure, and on dimensionality of perovskites. [5]

1.1.1   Geometrical parameters

The relative ion size requirements for stability of the cubic structure are quite stringent, so slight buckling and distortion can produce several lower-symmetry distorted versions, in which the coordination numbers of A cations, B cations or both are reduced.

Many physical properties of perovskites depend crucially on the details of these distortions, particularly the electronic, magnetic, and dielectric properties, which are very important for many of the applications of perovskite materials. For example, the distortions caused by cation substitution can be used to fine tune physical properties exhibited by perovskites. [6]

For perovskites, the measure of the mismatch between the average equilibrium A–X and B–X bond lengths is expressed by the semiempirical formula of the Goldschmidt's tolerance factor in Eq. (1).

$$\tau = \frac{r_a + r_x}{\sqrt{2}(r_b + r_x)} \ (1)$$

where r_a, r_b and r_x are the ionic radii of A, B and X, respectively.[6]

The ideal perovskite cubic structure (a phase, Figure 1.3a) requires t to be in the range from 0.89 to 1.11 and ideally close to 1. When $t < 0.89$, a triangle (b-phase, Figure 1.3b) or orthogonal (g-phase, Figure 1.3c) with lower symmetry will appear.
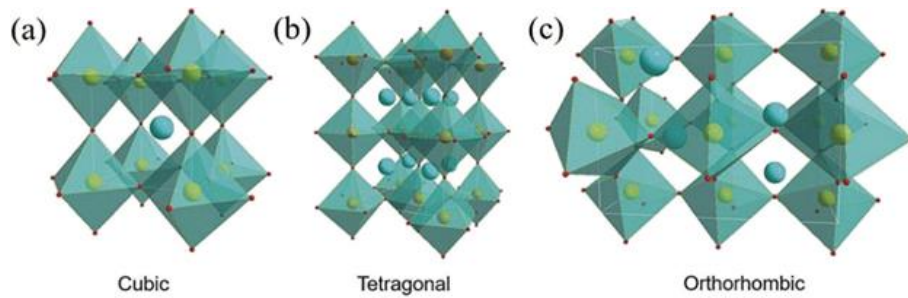

Figure 1.3. The crystal structures of perovskite materials with different symmetries: (a) cubic phase, (b) tetragonal phase, and (c) orthorhombic phase.

The smaller the A-site cation, the smaller the t because of the deformation of the octahedral frame due to the lack of support; in this case, A cation cannot completely occupy the space of the BX_6 cubic octahedron. When the t value is greater than 1, it indicates that the A-site cations are too large to enter in an octahedral framework therefore lower dimensionality perovskites are formed. Figure 1.4 shows the value of tolerance factor as a function of A cation and how lattice is affected. [7]
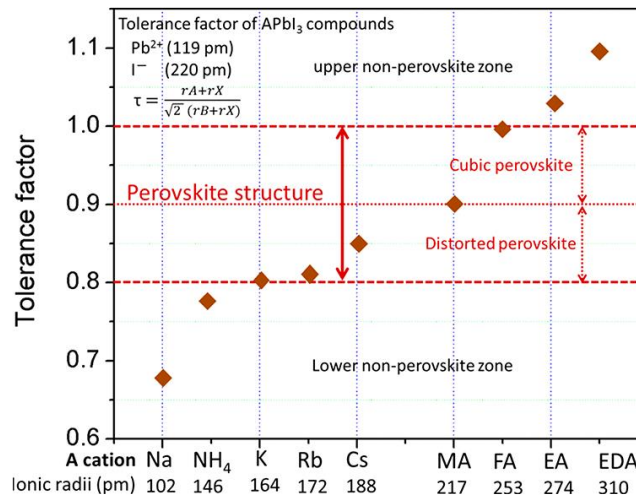
Figure 1.4. Calculated tolerance factors (τ) for different cations (A) in APbI₃ perovskite system.[8]

Therefore, predicting the radii of cations is critical to determine the proper tolerance factor, which allows to estimate whether certain compositions can form a stable cubic perovskite structure. For example, with methylammonium or formamidinium, using $t = 1$ and the largest values for R_M and R_X (*e.g.* $R_{Pb} = 1.19$, $R_I = 2.20$ Å), the limit on R_A is found to be 2.6 Å. Consequently, only small organic cations are expected to fit into the structure. Goldsmith factors outside 3D range results in low dimensional perovskites, that will be analyzed in the next chapters. These perovskites have an ordered lead halide network continuous in 0,1 or 2 dimensions. [9]

But this parameter cannot describe completely perovskites stability, so an additional consideration for formability is the octahedral factor (μ), $\mu = r_B/r_X$. Indeed, it has been reported low dimensional perovskite selecting cations such as imidazole that have t<1.[10] Under these constrains on t and μ parameters cubic perovskite can be obtained, but application of pressure or crystallization temperature can modify structure and properties of these compounds.

In this work, a review about perovskite state of the art of Hybrid halide perovskites is present, together with their applications and limits. Then, low dimensional perovskites were studied as alternative. After a review on organic cations' effect, imidazolium ones were investigated as promising choice

2. State of the art

2.1 3D Hybrid halide perovskites

Halide Perovskites with a 3D lattice order are obtained with the selection of ABX_3 constituents that allows to fulfill the previous requirements. This type of perovskite was investigated for optoelectronic application, thanks to their optoelectronic properties and the possibility of solution processing.[2]

First, halide perovskites have high electron mobility (800 cm^2/Vs) and high carrier diffusion length (exceeding 1 μm). These materials possess ambipolar charge transport behavior, high absorption coefficient (greater than 10^5 cm−1) due to *s-p* antibonding coupling, low exciton binding energy (less than 10 meV), high photoluminescence (PL) quantum efficiency, high carrier lifetime (higher than 300 ns) and low surface recombination velocity.[2]

Second, perovskite can be deposited from a solution of precursors at lower temperatures with a cheaper and easier process, with respect to traditional semiconductors. For example, thin film of perovskite was deposited by inkjet printing, drop casting, doctor blade coating, spin coating or spray coating.[2]

Band structure of typical 3D perovskite (Methylammonium (MA+) and Cesium (Cs+) are characterized by a metal halide structure with low coupling with MA+ or Cs+ cations. Looking at band structure, these cations act mainly as compensating role for vacancies inside perovskite structure. So organic cations interact with inorganic sublattice thanks to ionic interaction, without strongly affecting band structure.

Electronic structure between Cesium and MA perovskites are quite similar, with direct band gap (Figure 2.1). In fact, valance band maximum comes from combination between metal-s orbital and X-p orbitals in antibonding state, while conduction band minimum is made from Metal-p and X-p orbitals in non-bonding state (less affected by lattice distortion).[11] So, band structure is defined only by metal halide structure and perovskite energy gap is defined by:

- Dimensionality of MX_6 network (as it will be discussed in next sections, decreasing dimensionality increases perovskite bandgap)
- Increase of the angle of M-X-M bonds
- Decrease anions electronegativity
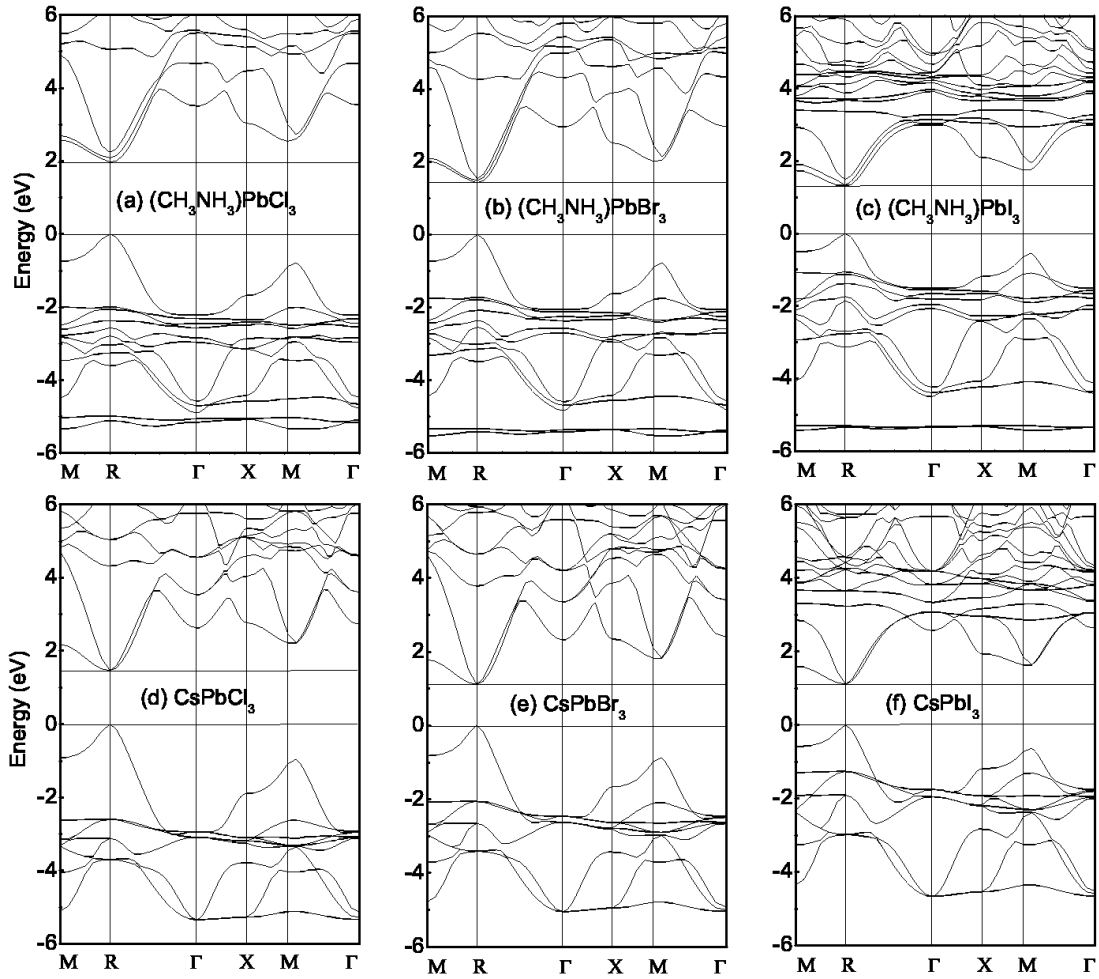- Decrease difference in electronegativity between anion and metal

Figure 2.1. Electronic structures of (CH₃NH₃)PbX₃, where (a) X = Cl, (b) X = Br, and (c) X = I, compared with those of CsPbX₃, where (d) X = Cl, (e) X = Br, and (f) X = I [11]

As described from Prasanna et al. [12], A-site cation can distort the perovskite lattice in two distinct ways: by tilting the MX_6 octahedra (increasing band gap), or by contracting the lattice isotropically (reducing E_g).[12] This effect happens because structural changes that increase M-X overlap will decrease the band gap thanks to destabilization of VB; while structural changes that reduce metal-halide overlap will increase band gap. In addition, substitution of B-site ion with calcium, strontium, or barium increases the propensity to tilt perovskite structure. Also, hydrogen bonding by the A-site cations can stabilize a tilted structure.[13]

3D Perovskites allows band gap tunability made from selection of halide, metal, and compensating cations. As described from Unger et al.[14] bandgap can be tuned from 1.2 eV up to 2.5 eV (Figure 2.2). However, a narrower range for optoelectronic

application was observed caused by photoinduced phase segregation of some compounds (given from halide migration in light that segregates phases), with range starting from 1.7-1.8 for MA and FA perovskites.[14]
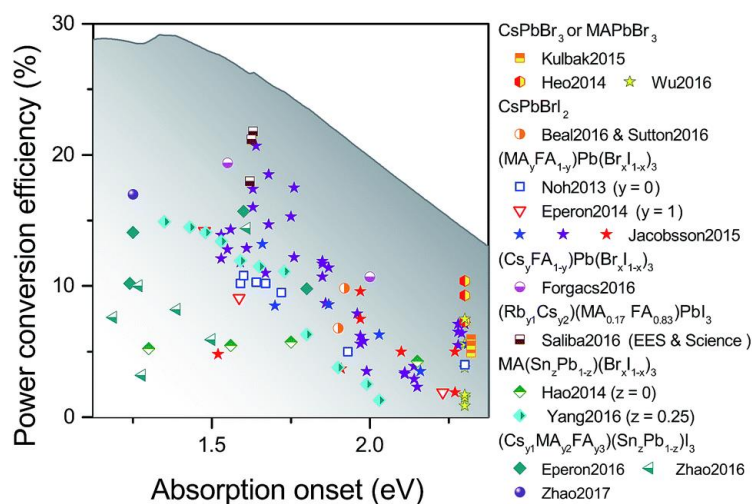

Figure 2.2. Power conversion efficiency values obtained for metal halide perovskite based solar cells as a function of the absorption onset of the perovskites [14]

In addition, perovskites band structure offers a defect tolerance given from shallow traps, electronically inert. They can induce electronic states close to the edge of conduction or valence band (with difference in energies $\leq k_B T$). These are considered not detrimental for the device performances since they mainly affect the charge carrier effective mobility.

They're different from deep trap states that affect bandgap (Figure 2.3). This effect is made from perovskite band structure (simplified in Figure 2.4): Strong antibonding coupling between M-s orbital and X-p orbital expands VB bandwidth and raises VB edge. So, defect states are located within or closer to VB edge. CB edge exhibits an ionic character due to weak coupling among M-p orbitals and X-p orbitals, so energy states are not much affected by external defect levels. [15]

Shallow traps (Figure 2.3 right band diagram), which depend on their oxidation state, can trap a hole or electrons. Electrons exhibits a faster time of trapping and recombination, while holes recombine in slower time, resulting in a fast loss of photo-carriers. So, electrons trapping will result in a deactivation of the trap states, given their very long lifetime, which will result in a lower "effective" density of defects. [15]
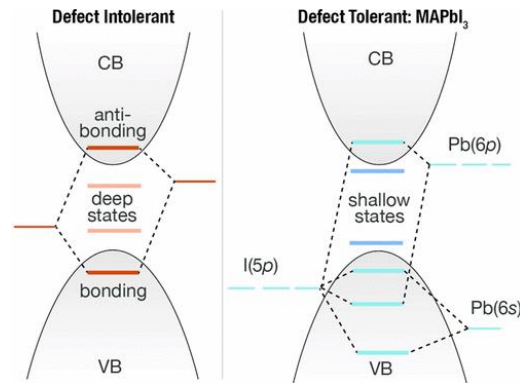
Figure 2.3. Electronic structure of defect intolerant semiconductors and defect tolerant perovskites[16]
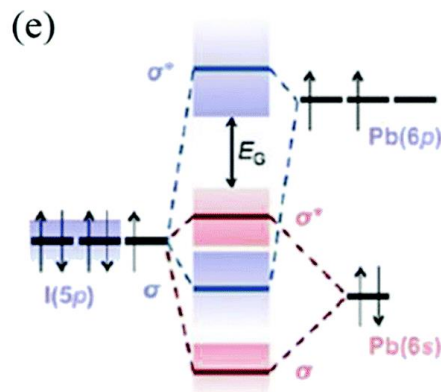
Figure 2.4.Bonding (σ)/antibonding (σ*) orbitals in MAPbI₃ demonstrating the formation of the energy bands relative to the isolated p and s atomic orbital [16]

Main defects responsible for non-radiative recombination and loss of performances of devices can be ascribed to surface defects and grain boundaries, as extended defect site, modifying interaction carriers-lattice and recombination. [15]

There are two kinds of approaches to defect passivation: addition of passivation agents to the precursors which may work on grain boundaries and introduction of interlayers for the surface. These aspects will be explained later.

2.1.1   Optoelectronic application

Perovskite materials have been investigated for different optoelectronic properties, thanks to their tunable bandgap as semiconductors.[14] Here it is reported the main applications (LEDs and solar cells), with a brief overview of other applications.

One application of lead halide perovskites is **PeLED** (perovskite light emitting diodes) thanks to their electro-optical properties, an easy processing, and a high degree of versatility.[17]

Halide perovskites can surmount the limitations of both traditional LEDs (suboptimal color quality) and emerging LEDs based on quantum dots (slow response time) and organic emitters (low maximum brightness) by producing bright, cost-effective, and high-color-purity LEDs. Moreover, solution processing technique (easier thanks to defect-tolerance of perovskites) allows PeLEDs to be competitive in future, thanks to lower costs of raw materials compared to OLED and III-IV semiconductors LED. Then, these materials allow to tune emission wavelength with chemical composition. [18]

For this application the following optical properties of perovskites must be assessed:

1. PLQY (photoluminescence quantum yield): defined as the number of photons emitted as a fraction of the number of photons absorbed or PLQE (photoluminescence quantum efficiency)[19]
2. Electroluminescence and Photoluminescence spectra: they describe wavelength values at which perovskites emit. In addition, FWHM (full width half maximum) is evaluated to understand broadness of light signal in wavelength domain)[19]
3. Relaxation time: it allows to understand carriers' recombination and response of the system)[19]

Perovskite in LED can be used to obtain two different types of devices:

1. Optically pumped perovskite LED: perovskites act as phosphors for down-conversion from UV light[20]
2. Electrically pumped perovksite LED (EL-PeLED): perovskite act as an active layer between HTL and ETL for light emission [20]

In electrically pumped perovskite LED (shown in Figure 2.5), under forward bias, carriers are injected into the perovskite layer through HTL and ETL, respectively, and then the radiative recombination happens.[20]
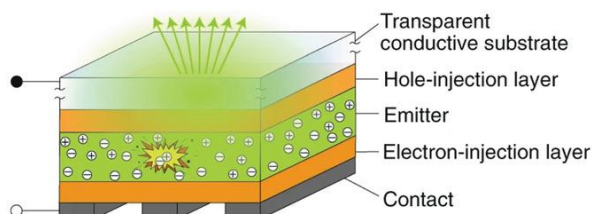

Figure 2.5. Schematic of an archetypical p-i-n PeLED. Note that the electron-injection and hole-injection layers can be interchanged to form an n-i-p architecture[17]

Some challenges remain for EL-PeLEDs use and commercialization[17]:

1. Device stability, given the limited lifetime due to degradation induced by moisture, temperature, photodegradation and bias[17]
2. Outcoupling design, caused by generation and propagation of photons across the device boosted through antireflective phenomena. This also includes a decrease in the parasitic absorption due to light delocalization in non-active layers and an increase in radiative recombination events through light confinement and multilayer-like resonances at the emission wavelength[17]
3. White light emission, difficult because of blue LED instability[17]

Optically pumped LEDs with perovskites have been studied as alternative (with a different architecture made from a InGaN chip as light source and a phosphor, shown in Figure 2.6) for white PeLEDs. In these devices perovskite materials were studied as down-conversion phosphor for a UV light to obtain visible light.[17]
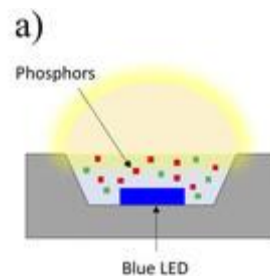

Figure 2.6. (a) Schematic illustration of optically pumped WLEDs[21]

Halide perovskites are regarded as one of the most interesting materials for this application thanks to the high PLQEs and absorption coefficient, wide luminescence spectrum, easy preparation and low production cost.[20] Optically pumped PeLEDs exhibit tunable emission, high brightness, high color purity and wide color gamut (coverage of color spectrum in CIE space).[22]

For perovskite white optically pumped LEDs following parameters are considered:

(1) EQE defined as ratio between number of photons emitted from the LED to the number of electrons passing through the device. This value describes the overall efficiency of LED device
(2) color rendering index (CRI; 0–100), which quantifies the ability of light sources to accurately show the colors of objects that would be observed under natural light[21]
(3) correlated color temperature (CCT; units of K) with higher CCTs describing "colder" or bluer white light, obtained from Planckian locus (Figure 2.7, a graph that converts CIE coordinates in temperature values for white light) [21]
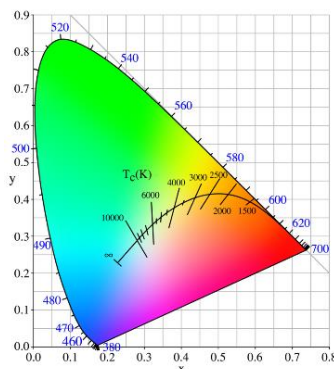
Figure 2.7. Planckian locus for correlation among Temperature for black body and CIE coordinates [21]

(4) luminous efficacy (units of lm W^{-1}) describing the ratio of the luminous flux produced by the electrical power input. [21]

In addition, Perovskite-phosphor optical properties are evaluated with PL measures by exciting them with UV light, with PLQE near unity for single color LEDs. However, different strategies were studied to obtain selected colors (that can be combined for white light) or broadband emission over the visible spectrum.[21]

3D perovskites nanocrystals were used because of their highly tunable narrow emissions over the entire visible region with PLQEs near unity. Two major strategies have been developed to achieve bandgap control of NCs, relying on the manipulation of halide compositions and through quantum-size effects.[23]

Non-perovskite phosphors have often been used together with perovskite NCs to achieve white emission, given the narrow FHMW of these perovskites. Alternatively, dual emission can be realized by doping other metals in perovskite NCs, such as Mn^{2+}, Bi^{3+}, and Eu^{2+}.[21]

However, there are still many issues and challenges to solve, including thermal instability, particle aggregation, anion exchange, ligand dissociation and photostability. To address these issues, various surface treatments have been developed for perovskite: compositional engineering; surface engineering, matrix encapsulation; and device encapsulation.[24]

Low dimensional perovskites, explained in the next chapters, have been studied as an alternative to obtain better white light and improve stability of PeLED. [21,24]

Three dimensional perovskites were mainly investigated for **solar cells** thanks to the optoelectronic properties described before. Initially they were used as light synthesizer, on mesoporous TiO_2 with liquid electrolyte (Figure 2.8a) and then with devices with pores filled with HTL (hole transport layer), reaching PCE (power

conversion efficiency) of 6.54% (Figure 2.8 b).[2] Finally, thanks to demonstration of the use of perovskite with Al_2O_3 scaffolds in dye sensitized solar cells, perovskite electron transport was studied and PCE of 10.9% was obtained (Figure 2.8 c). Further evolution of perovskite structure was obtained with the so called "regular structure", where thickness of absorption layer was increased by infiltrating perovskites in m-TiO2, reaching PCE of 19.3%. [25]

Nowadays studies are focused also on n-i-p heterojunction structure ((Figure 2.8e) with perovskite as intrinsic layer, eliminating mesoporous layer and improving stability and PCE up to 20.8%. Inverted solar cells (p-i-n) (Figure 2.8f) have also been studied, changing HTL and ETL (electron transport layer) materials. [2,25]
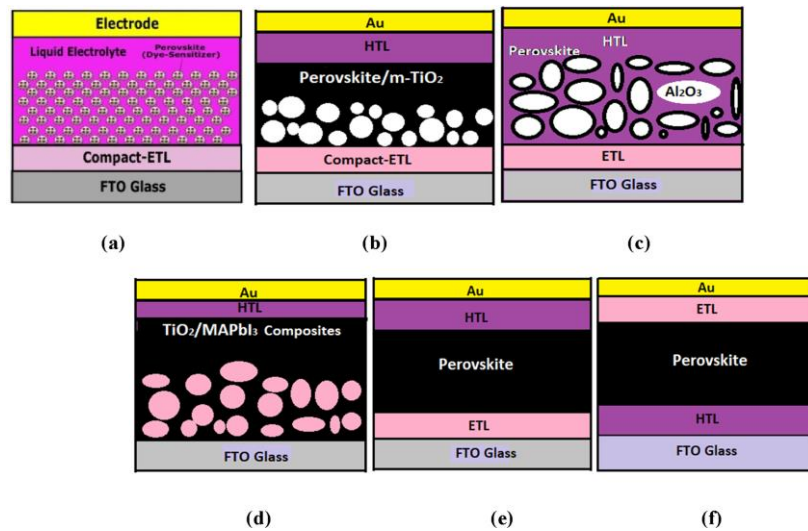
Figure 2.8. Device architecture cross section: (a) DSSC (b) Mesoporous (b) Supermesostructure (c) Regular (d) Planar n-i-p (e) Planar p-i-n (inverted planar) structure.

Bandgap tunability of perovskites allows to maximize the V_{oc} and I_{SC} tuning energy levels with HTL and ETL thanks to different composition of perovskites. In Figure 2.9 the most studied combinations of materials and their band structure for intrinsic or inverted solar cells are summarized. [2]
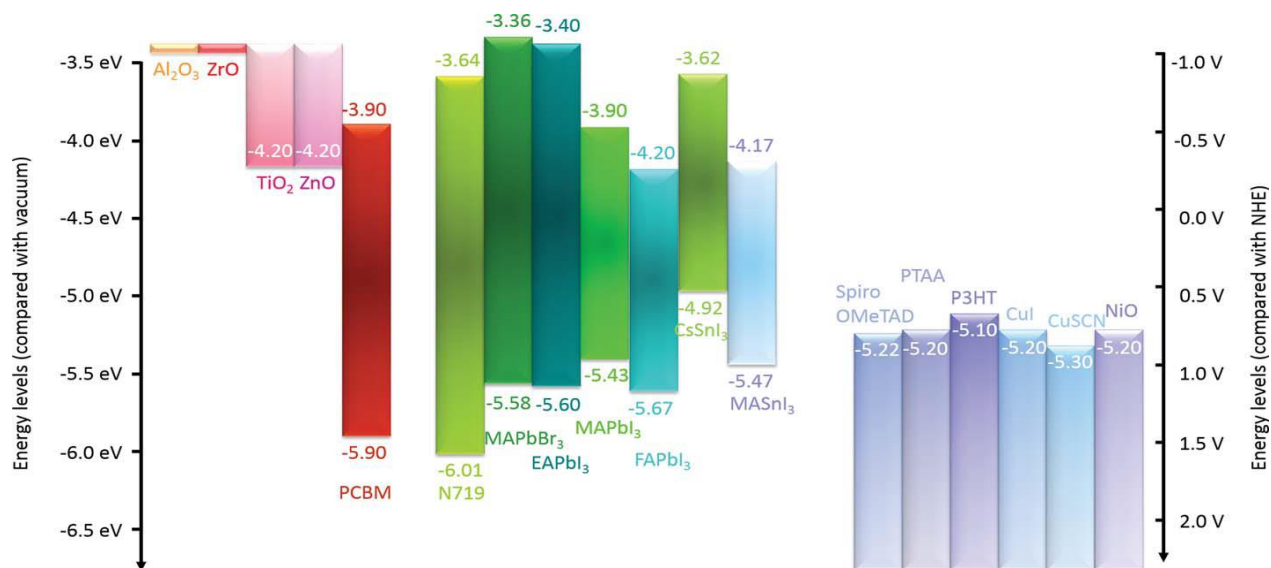
Figure 2.9. Schematic of literature values for energy level alignment for different materials acting as the electron selective contact material (ETM) (left), absorbers (middle) and hole selective contact materials (HTMs) (right) in solar cells. [2]

Another possible use of perovskites in solar cells can be found in tandem solar cells, which are constituted by different stacked light-absorber layers, including almost one made from perovskite. Tandem solar cells can cover entire solar spectrum thanks to the change in composition of perovskite absorber layer (PCE 12.3%) or the use of other absorbers (efficiency around 22%), which keeps a semi-transparent perovskite layer on top.[26-28] Despite these solar cells provide high Voc and PCE, fabrication remains an important issue, provided by different temperature and processing techniques for different layers and their electrical discontinuity at interfaces.[26]

Despite all these advantages, diffusion of perovskite solar cells is limited by some important drawbacks concerning the toxicity of lead and its derivatives and the stability of devices. In fact, one of the main issues related to perovskite solar cells is the intrinsic instability of the perovskite material upon exposure to environmental moisture and oxygen, high temperature and radiation. So, perovskite solar cells have shorter lifetime, ranging from few days to months and maximum up to a year, much lower than 25 years silicon solar cells lifetime. [2,22]

Thanks to the previously described optoelectronic properties, metal halides perovskites have been studied also as easy-processing alternative for **photodetectors**. Picosecond-time exciton dissociation and good ambipolar charge transport, lead to investigation of these materials with good results on the main photodetection parameters. [29]

Perovskite lasers are under investigation by analyzing quantum structures made with 3D perovskites. Optically and electrically pumped lasers have been fabricated but with limitations attributable to Auger recombination and low stability. [30] [17,22]

3D perovskites have been studied also for **X-ray detection**, thanks to the presence of high atomic number elements, with two methods:
1. direct conversion: this method converts x-ray photons directly into electrical charges. Single perovskite crystals give good results, despite some growth limitations on large areas.[31]
2. indirect conversion: with an intermediate step, x-ray photons are converted into visible light by a scintillator prior to conversion into electrical charges by a photodiode. Perovskite NCs have been investigated for this application. [31]

New studies are also investigating the application of perovskite for resistive switching application, thanks to low voltage switching along with high on/off ration and fast switching speed. However, these studies are still at the beginning, even some improvements have been obtained using low dimensional perovskites. [31]

2.1.2   3D halide perovskites issues and limitations

Despite perovskites offer interesting optoelectronic properties some problems are still limiting their use and diffusion for optoelectronic devices.

Toxicity caused by the presence of lead in perovskite materials is one of the main limitations. Despite the presence of other solutions using tin and manganese, their performances and stability are lower. Degradation remains a serious issue of these perovskite. This effect is made from higher stability of Sn^{4+} with respect to Sn^{2+}, leading to an easier oxidation and introducing p-doping in perovskites, increasing recombination and so solar cell efficiency. Moreover, degradation under ambient creates a cyclic effect with creation of iodine as aggressive specie to obtain degradation product such as SnI_4. [2,22,32]

The other main issue related to the use of Perovskite materials in optoelectronic device is their stability. Phase stability tuned with A-cations selection should be considered. Given suitable A cations, other problems are present.

Stability issues can be classified in two main categories (Figure 2.10, According to Jena et al. classification)[8]
1. Structural intrinsic stability
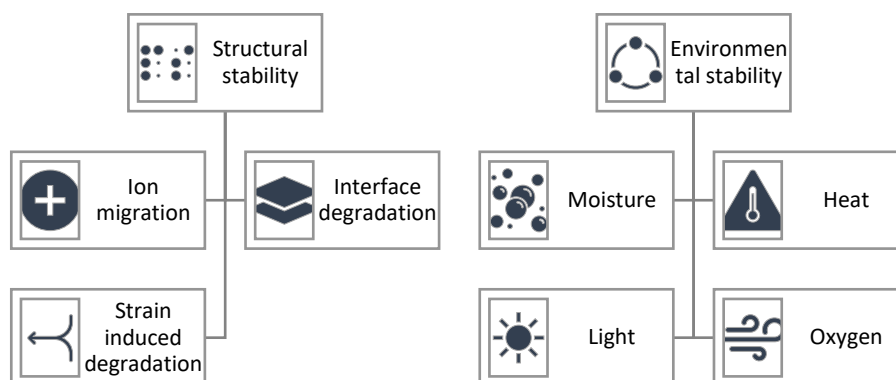2. External/environmental stability

Figure 2.10. Stability issues for perovskites, ri-elaborated from Jena et al. [8]

I. **Structural intrinsic stability** issues concern perovskite structure and their use in optoelectronic devices:

1. **Ion migration:** intrinsic ion migration persists to occur under the influence of electric field, either generated under sunlight or biased externally in dark. [8] This phenomenon is correlated with anomalous J-V hysteresis, phase segregation, and is driven by presence of vacancies in perovskite lattice, with the mechanism described in Figure 2.11. This effect can be reduced thanks to perovskites with mixed organic-inorganic composition or alkali metals in interstitial position. [8]
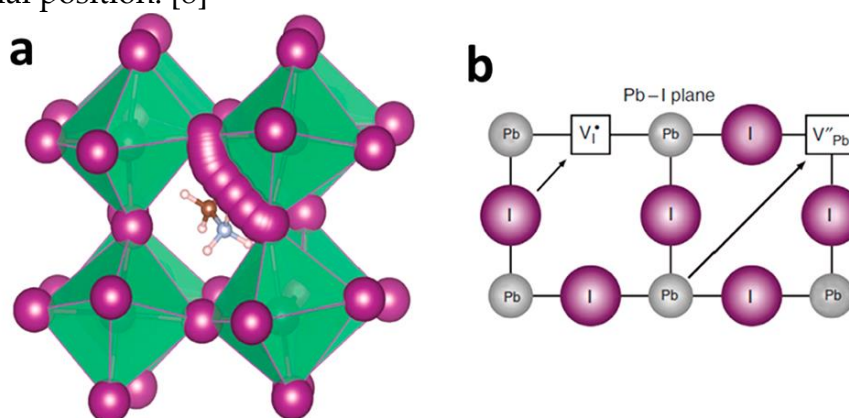
Figure 2.11. (a) Proposed migration path of I- ions along the I−I edge of the PbI64- octahedron in the MAPbI3 crystal. (b) Illustration of the migration paths for I- and Pb2+ ions in the Pb−I plane. [8]

2. **Interface degradation:** In optoelectronic devices, these interfaces between perovskite and other layers play a vital role in the proper charge collection.[8] Undercoordinated halogen atoms at surface distorts the tetragonal crystal

structure and creates pinholes and irregularities at the interface. These irregularities may further serve as recombination sites reducing charge transport.[33] Improving crystallinity can contribute to increase the stability. This can be obtained by using additives to passivate undercoordinated sites.[33] In addition, using confined structures for optoelectronic applications like QDs introduces the problems related to quantum structure stability.[22]

3. **Thermal strain and strain induced degradation** given by annealing or deposition (shown in Figure 2.12). These strains can cause ferro-elasticity, with phase transition under the applied stress. Strain-induced degradation should be also considered in perovskite design for enhancing overall stability of devices.[8]
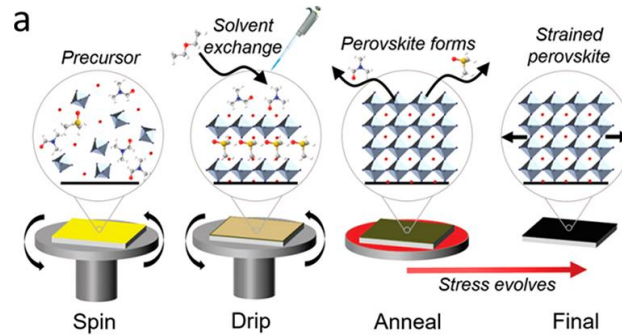
Figure 2.12. Schematic illustrating the stages of film formation and stress evolution in the film.[8]

II.   **External/environmental stability** is more related with interaction with external factor: light, moisture, heat and oxygen. here are described the main phenomena affecting perovskites[8]:

1. **Moisture induced decomposition**: This type of degradation can happen also in dark condition: Water molecules can easily bind to perovskite by hydrogen bonding to form hydrated compounds, which alter local perovskite properties.[8] The losses can be reversed but further entrance of water can cause irreversible degradation of perovskite to PbI2 and other components, as described by the cycle depicted in Figure 2.13. A key step is made from the formation of hydrated compounds more prone to degrade in (CH3NH2), HI, and PbI2. As described below, water hydrates perovskite creating a decomposition in lead (II) iodide and hydrated organic lead halide (reaction (a)). However, this reaction is reversible, but de-hydration of $(CH_3NH_3)_4PbI_3$ will create degradation in initial organic molecule and lead (II) halide (reaction(b)).[33]

This type of degradation is reduced by encapsulation of device to avoid contact. Hydrophobic layers or passivation are new promising strategies.[8]
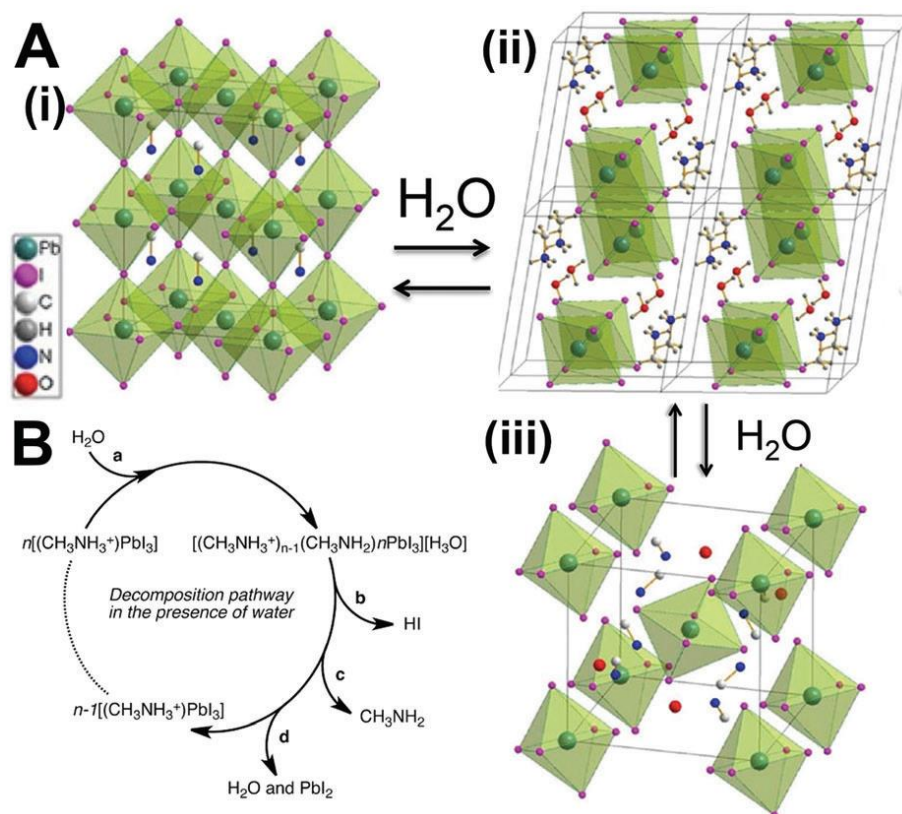
$$(a)\ 4CH_3NH_3PbI_3 + 4H_2O \leftrightarrow 4[CH_3NH_3PbI_3 \cdot H_2O] \leftrightarrow (CH_3NH_3)_4PbI_3 \cdot 2H_2O + 3PbI_2 + 2H_2O$$
$$(b)(CH_3NH_3)_4PbI_3 \cdot 2H_2O \rightarrow 4(CH_3NH_3I) + PbI_2 + 2H_2O$$
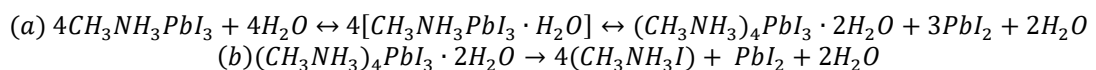
Figure 2.13. (A) The two hydrated structures of the MAPbI3 perovskite and the structural evolutions[34](B) Possible decomposition pathway of MAPbI3 in the presence of water[35]

2. **Oxygen degradation**: oxygen in contact with perovskite is absorbed on the surface passivating the trap state, thus creating an enhancement of luminescence. But, with the formation of superoxide ions in presence of light, perovskites undergo a degradation, through a process made by 4 steps, shown in Figure 2.14 leading to perovskite decomposition in PbI_2, H_2O, I_2 and CH_3NH_2 (Figure 2.14d), with the reaction described below: first light creates superoxide ions, then they interact with perovskite leasing to decomposition:

$$O_2 \rightarrow (CH_3NH_3)_4PbI_3 \rightarrow Light \ (no \ moisture) \rightarrow O_2{}^{\cdot -}$$
$$(CH_3NH_3)_4PbI_3 + O_2{}^{\cdot -} \rightarrow MeNH_2 + PbI_2 + H_2O$$

These products are decremental to charge transfer and can be avoided using less-acid cations, such as formamidinium (FA+) or inorganic cations (Cs+). Good integration of ETL reduces this effect. [36]
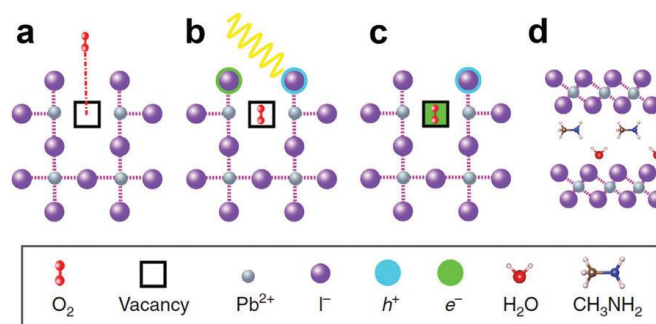
Figure 2.14. Schematic representation of the oxygen-induced decomposition (a) Oxygen diffusion and incorporation into the lattice, (b) photoexcitation of CH3NH3PbI3 to create electrons and holes (c) superoxide formation from O2, and (d) reaction and degradation to PbI_2, H_2O, I_2 and CH_3NH_2[36]

3. **Light induced degradation**: all chemical, physical, or electronic processes are influenced or enhanced by light. Regarding perovskite materials photo-induced phase segregation creates halide-rich region, resulting in low bandgap trap state that affects optoelectronic properties. Light accelerates degradation of perovskite into PbI_2 and HI, as described by the reaction shown in Figure 2.15.[33] Then organic part can be decomposed in volatile compounds with reversible reaction. PbI_2 suffers degradation under light given from decomposition in molecular iodine and metallic lead.[33]

Alternative solutions can be the reduction of grain boundaries or the selection of cations, which reduce volatility. In addition, the reduction of halogen defects decreases the possibility to have these trap states.[8]

Regarding devices, main problems are caused by the degradation between charge transport layers and perovskites, which plays a vital role in charge collection.[33]
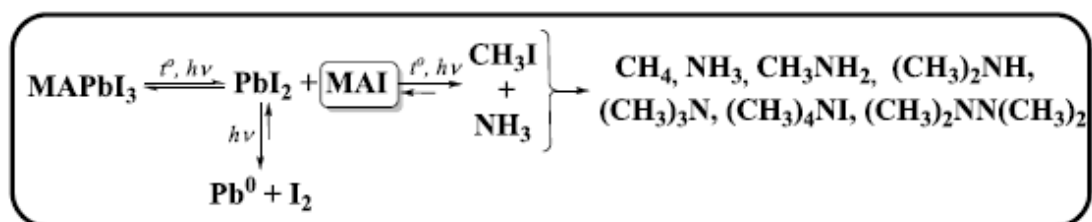
Figure 2.15. Scheme illustrating the photochemical degradation pathway of MAPbI3 films.[33]

4. **Thermal degradation**: Organic–inorganic hybrid and all-inorganic perovskites possess a good thermal stability, with degradation around 200°C for organic part and over 500°C for sublimation of PbX_6 octahedra.[8] However, the

oxygen- and moisture induced decomposition are accelerated and amplified at high temperature. And dehydration/hydration reaction enhances decomposition with temperature:

$$(CH_3NH_3)_4PbI_3 \cdot 2H_2O \rightarrow CH_3NH_3 + HI + PbI_2 + H_2O$$
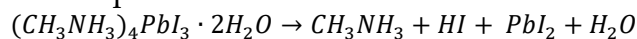
Among all techniques to enhance perovskites stability issues, next chapters will focus mainly on the use of low dimensional perovskites and a brief overview passivation of surface with functionalized molecules.[8,22]

2.1.3   Surface and defects passivation

Perovskite performances in terms of optoelectronic properties and their stability can be enhanced using techniques at different scales. One approach can be made by an accurate design of device, for example with previously described tandem solar cells or using different types of LED devices. Another solution can be optimization of the deposition process to avoid defects related to crystallization processes. A new approach from a chemical point of view consists in interaction engineering, where perovskite and interfaces with different layers are optimized to enhance devices' performances. Also, bulk perovskite structure can be studied and optimized according to this approach.[37,38]

The idea beyond interaction engineering is the passivation of critical sites for recombination in perovskite materials, mainly made from grain boundaries, local lead clusters, undercoordinated species and dangling bonds. Moreover, passivation can enhance charge transport with HTL or ETL.[37]

The strong tunability of halide perovskites favors the employment of this strategy. Interaction engineering can be especially adopted to reduce the problems of device stability due to its very high sensitivity to oxygen and external moisture.[38]

Interaction engineering has been studied for surface passivation, using different type of interaction between organic and inorganic modules in perovskites. Here some examples are described:

1. **Hydrogen bond**: Hydrogen bond (HB) is an important intermolecular interaction, which involves a polar hydrogen-bond donor group D^{d-}–H^{d+} and an electronegative atom A^{d-} as the hydrogen bond acceptor denoted as ''D–H...A''. D and A are electronegative atoms such as   N, O, F, S, or in some cases even C. Hydrogen bond in perovskites can affects phase transitions, ion migration and water interaction. In addition, HB can be exploited for crosslinking across perovskite grains or for interfaces modification in optoelectronic devices.[38] HB has been exploited to passivation by external additives onto perovskite

surface. Thanks to HB, these molecules can bind to surface increasing stability of overall device.[39] Interaction with water can be described by interference of water on HB among MA+ cation and $[PbI_6]^{4-}$ inorganic cage. So, if strength of H-bond among a cation and inorganic octahedral cages increases, perovskite structure is stabilized. [38]

2. **Dative bond:** Lewis's acid-base chemistry has been effectively used for passivation of undercoordinated sites on perovskite's surface. Created adducts are linked by a dative bond (coordinate covalent bond), where two shared electrons come from the same atoms.[37,38]

   Typical defects on perovskite's surface are undercoordinated $Pb^{2+/1+/0}$ and $I^{1-/0}$. In addition, mobile I^- anions, I_2 interstitials, undercoordinated A+ cations and $Pb^{2+/1+}$ cations, and Pb^0 clusters and anti-sites PbI_3^- can be present (Figure 2.16).[37,38]

   Lewis's acids are used because of their capability of accepting a pair of non-bonding electrons. These compounds have the capability to passivate electron rich defects (Undercoordinated I^- and PbI_3^-), which can also be considered as Lewis bases. On the opposite, Lewis bases can donate a pair of non-bonding electrons in order to passivate Lewis acids defects ((that accept one pair of electrons), thus creating a Lewis adduct. Perovskites Lewis acids defects are made of undercoordinated Pb^{2+} or Pb clusters. Usually, they're passivated using compounds containing nitrogen or sulfur functionalities.[37,40]

   The formation of Lewis adducts can reduce the nonradiative charge recombination, improving device performance and stability.[37,40]
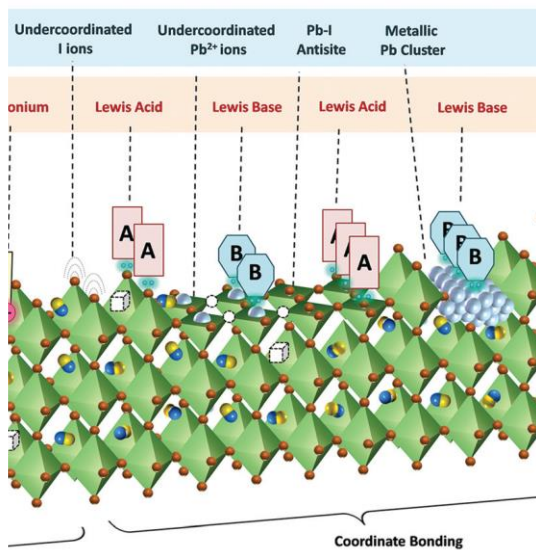
Figure 2.16. Imperfections in OIHP film and their passivation by dative bonding[37]

3. **Ionic bond:** Ionic bonding involves the complete transfer of one or more valence electrons from one atom to another to afford an electrostatic interaction between two ions of opposite charge. Annihilation of trap states can be made with complementary ions. These cations, too big for 3D perovskites, can be added on the surface or inside precursors' solution to passivate surface and grain boundaries. Organic ions can also be functionalized to improve moisture resistance. Zwitterion passivation using molecules possessing positive and negative groups has been explored. These molecules can provide ionic bonding or dative bonding passivation of negatively and positively charged species. [41]

4. **Halogen bond:** Halogen bond is an intermolecular interaction between an electrophilic region associated with a halogen atom in a molecular entity X, (a halogen atom that can produce an electrophilic region made from its polarization induced by surrounding atoms) and a nucleophilic part that generally possesses more than one nucleophilic region (Y). XB occurs between R–X and Y through inter-attractions (Figure 2.17).

Figure 2.17. Schematic representation of halogen bond[42]

There are potential undercoordinated halogen ions during perovskite preparation, which provides the possibility for the formation of XB. Better performances have been reported using halogen bond donor as passivator of undercoordinated PbI_x species [38,42] Abate et al. [43] used iodopentafluorobenzene as halogen bond donor thanks to strong withdrwan of electrons by fluorinated aromatic ring. This reduce bond iodine ions exposed at the grain surface and prevent the formation of dipoles, suppressing hole recombination.[43] Halogen bond is enhanced by fluorinated groups on halogen acceptor, with possible hydrophobic effect.[44]

5. **Other supramolecular interactions**: p effects and Van der Waals interaction has been studied for perovskite passivation and interaction engineering inside perovskite lattice to improve their stability. [38,45]

In the next chapter low dimensional perovskites will be discussed, they were explored as alternative for some optoelectronic applications, and they can be integrated into 3D perovskites to enhance stability and performances. However, also lower dimensional perovskite structure can be tuned with interaction engineering, as shown in the next chapter.

2.2   Low dimensional perovskites

Before going into the details of low dimensional perovskite, it is necessary to clarify at which levels dimensionality is intended for perovskites.

First, the "material-level" low dimensionality is about chemical structure, underlining metal halide octahedra as building blocks, that the individual components should have at least one dimension down to the molecular level. This level can be refereed as electronic dimensionality of these systems, given quantum confinement inside these materials[46]
This term must not be confused with "system-level low dimensionality", for example with 3D perovskite nanocrystals, nanoplatelets or QDs, where dimensionality is given from the final morphologies. These perovskites exhibit quantum confinement but with different mechanism, in this case we talk about structure dimensionality instead of material one.[46]

In this thesis, the term "dimensionality" related to hybrid halide perovskites refers to structural dimensionality guided by the connectivity of the comprising metal halide polyhedral building. Metal halide structure creates quantum confinement inside bulk material, creating electronic continuity at different dimensionalities. While, for "system level" confined structures terms like nanoplatelets/nanosheets, nanowires/nanorods, and nanocrystals are used. [46]

Lower dimensionality perovskites (or low dimensional metal halides or "perovskitoids", as reported in some articles) are obtained reducing lattice symmetry thanks to organic cations' size. Here metal halides octahedra are connected in different ways, leading to confinement effect, as shown in (Figure 2.18). Starting from 3D perovskites, reduced lead halide connectivity can create systems continuous in 2 dimensions (2D perovskites analogous of quantum well), one dimension (1D perovskites, analogous of quantum wire) or octahedra can remain separates (0D perovskites, analogous of quantum dots).[47,48]
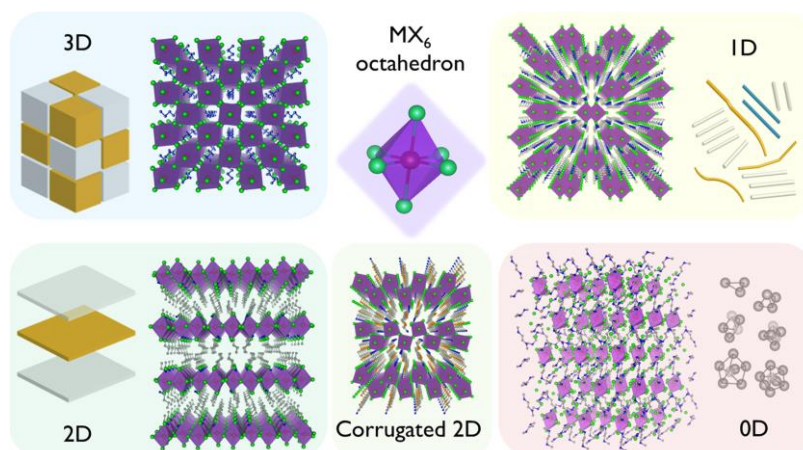
Figure 2.18. Typical low dimensional perovskites structures and their confinement effect - 2D quantum wells, 1D quantum wires, and 0D molecules/clusters [48].

2D hybrid halide perovskites are layered crystalline materials of general formula $A'_m BX_4$ constituted by sheets of inorganic corner-sharing octahedra BX_6 alternated with layers of larger organic monovalent ($m = 2$) or divalent ($m = 1$) cations (A'). 2D perovskites can be imagined as "cleaving" the 3D structure along a crystallographic plane to form sheets, adding halide ions to satisfy the surface metal coordination sites. The cleaving can be along the ⟨100⟩-, ⟨110⟩-, and ⟨111⟩-planes of the 3D structure, giving rise to ⟨100⟩-, ⟨110⟩-, and ⟨111⟩-oriented 2D perovskites, respectively(Figure 2.19b).[49]

Generalizing, the formula becomes $A'_m A_{n-1} B_n X_{3n+1}$, where A' is a large organic cation, A is a small cation (Cs+, Ma+ or FA+) while n indicates the number of inorganic sheets placed between each organic layer and it is directly correlated to the dimensionality of the system.[46,48]

Thus, strictly defined 2D perovskites have $n = 1$, 3D perovskites have $n = \infty$, while all the other intermediate structures with $n > 1$ are properly called *quasi*-2D perovskites and contain both the large bulky organic cation A' of 2D and small cation A (MA+, FA+, Cs+) (Figure 2.19a). More properly, this is the general formula for the common ⟨100⟩-oriented *quasi*-2D crystal (Figure 2.19). [49]
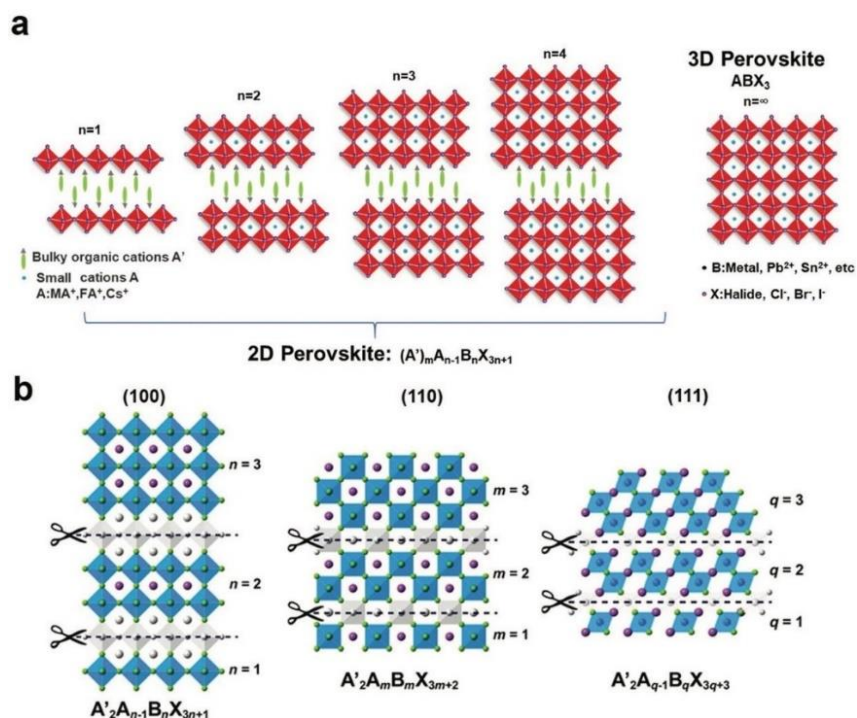
Figure 2.19. (a) Schematic comparing 2D, quasi-2D and 3D perovskite structures. (b) Different oriented families of 2D perovskites.[50]

Decreasing the dimensionality from planes of 2D perovskites structures, the 1D perovskites offers an additional degree of quantum confinement effects, with consequences on optical properties: strong Stoke shift respect to higher dimensionality, with wider selection of cations with respect to 0D systems.[51]

1D perovskites are composed from metal halide chains/wires/tubes surrounded by organic cations arranged by interactions among them and inorganic counterpart. These lead halide structure, as shown in Figure 2.20 can be arranged in different way, from simple chain to double chains. Inside each chain metal halide octahedra can have different connectivity: corner sharing, edge sharing and face sharing as depicted in Figure 2.21.[28,46]
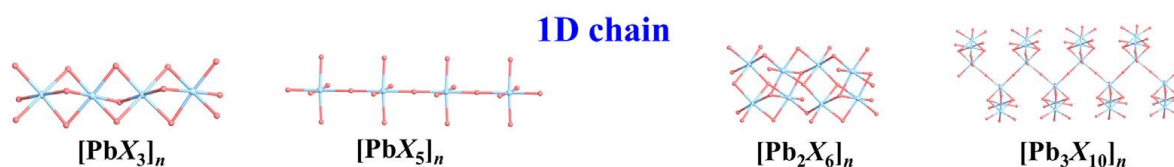
Figure 2.20. Structural diagrams for selected type I $[Pb(II)_aX_b]^{2a-b}$ (X = F, Cl, Br and I) anions.[52]

Chain connectivity and arrangement is templated from organic cations. Inorganic sublattice interaction with organic cations can be affected by halide atoms, steric

hinderance, flexibility and supramolecular interaction of cation functional groups. [53,54] General structure of unit cell is defined on c axis by the Pb-Pb-Pb bond length, while a and b direction are mediated from organic species, that also affect space groups. [55]
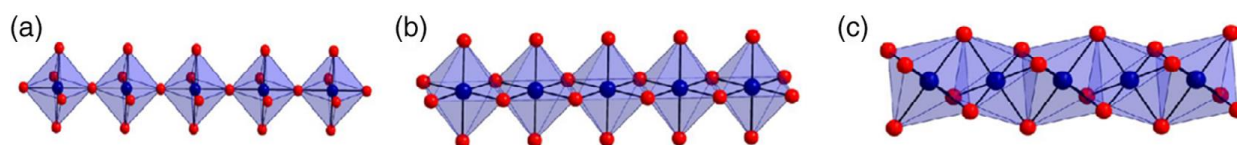
Figure 2.21. Lead halide chains connectivity : (a) corner-sharing, (b) edge-sharing, (c) face sharing [54]

Lower dimensionality perovskites are represented from 0D: these perovskites are composed from single metal halide clusters surrounded by organic cations. Differently from 1D and 2D, 0D perovskites do not have continuity in lead halide sublattice. However, 0D perovskites were usually obtained with inorganic components for example using Cesium, Rubidium or other metals.[56] Hybrid 0D structures were reported with organic cations possessing rigid and bulky substituents. Rigid aromatic or heterocyclic cations if added to these substituents can increase the steric impact allowing the formation of lead halide clusters (Figure 2.22). [51]
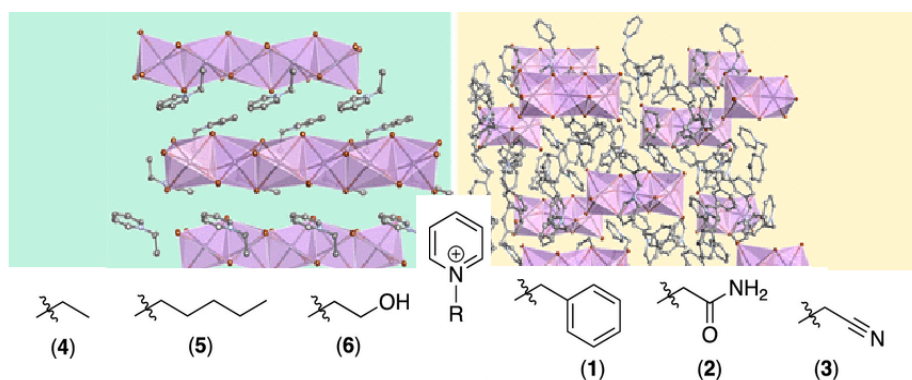
Figure 2.22. Bromo plumbate perovskites,1D with flexible substituent (1) and 0D with rigid substituent (2) elaborated from Febriansyah et al.[51]

Perovskites' dimensionality can be partially predicted from Goldsmith factor, values outside 3D range values (0.8-1.0) as condition for the creation of low dimensional perovskites.[30] However this rule is not always reliable for these perovskites,: following examples will show how dimensionality of perovskites can be affected by factors such as cations' functional group, halogen atoms and stochiometric ratio.

In 2D perovskites A-cation is responsible of level of dimensionality (quasi-2D can be obtained mixing typical 3D-perovskite cations with organic spacers) and it can modify shape and connection of lead halide networks.[57]

Beside steric hindrance of cation predicted from Goldsmith factor, electronic factors play an important role in defining dimensionality, since different intermolecular interactions may occur between organic and inorganic domains. For example, in lead bromide perovskite single crystal structure 3-hydroxiprydinium or pyridinium as cations are different: the first one has a 2D structure (Figure 2.23c and d), while the second one is characterized by lead bromide chains typical of 1D structures (Figure 2.23 a and b).[58]
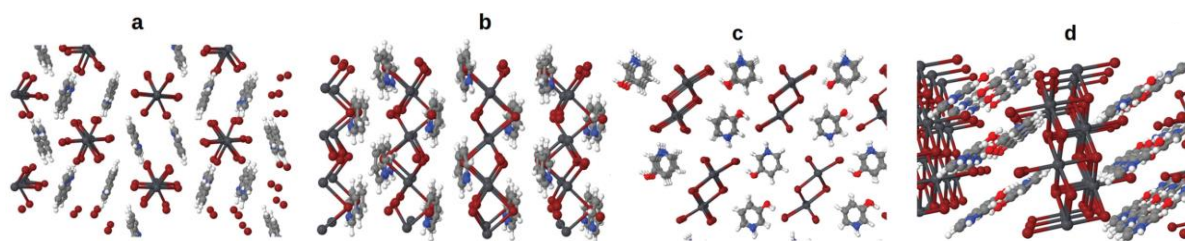
Figure 2.23. Ball-and-stick models of PyPbBr3 (a and b) and 3-OH-PyPbBr3 (c and d). Brown, light-grey, dark-grey, black, blue and red balls are Br, H, C, Pb, N and O atom, respectively.[58]

Hydrogen bond can act between halide atoms and cations and between cations, like other supramolecular interaction. Another parameter to consider is the cation valency. For example, it is reported that ammino-propyl imidazolium with lead bromide affords to a 2D perovskite[59], while other alkylated imidazolium produce 1D structures.[60-62] This effect is obtained thanks to H-bonds templating induced by Br atoms prone to hydrogen bonds. As explained from Smith et al.[59], ammino-propyl imidazolium act as bidentate cation and accommodates better between two inorganic layers allowing the creation of 2D perovskites.[51,59]

Another example of changing inorganic lattice, but keeping same dimensionality is reported from Thi-Mai et al.[63] using 4-ethyl-Pyridine (4EtPy) and 4-aminomethyl-Pyridine (4NPy) with lead iodide (Figure 2.24). 4EtPy crystallizes in the monoclinic system and formed a novel edge-shared triple-chain 1D perovskite, while 4NPy triclinic system and formed an edge sharing 1D perovskite. 4NPy was found to interact with the lead iodide chain through N2…H–I hydrogen bonds. [63]
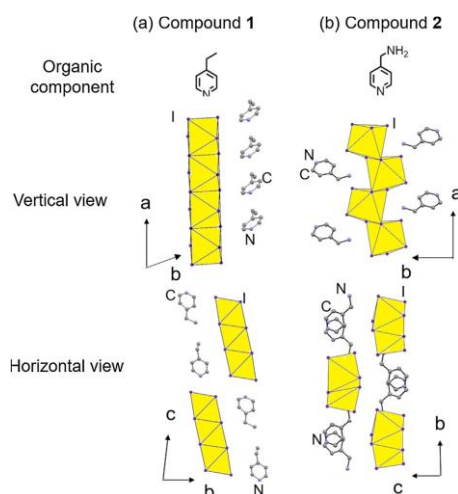
Figure 2.24. Schematic representations of the crystal structures of 4EtPy (1) and 4Npy (2). Hydrogens are omitted for clarity [63]

In addition, steric hinderance of halide anions must be considered for dimensionality. For example, as described by Kevorkyants et al. [64], different dimensionalities were obtained with fluorinated pyridine molecules using lead bromide instead of lead iodide.[64] (Figure 2.25.) A change in lead halide connectivity with variation of organic cations were also reported keeping the same halide atoms. [64]
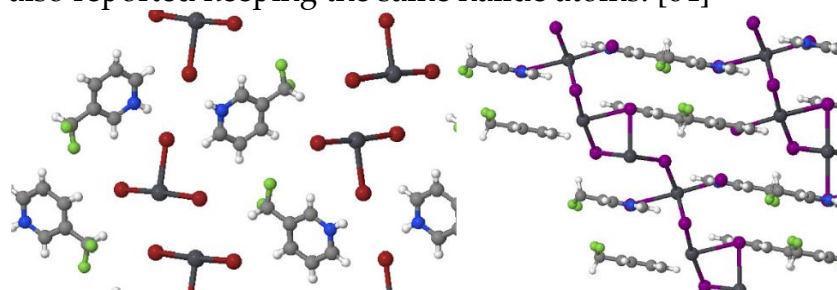
Figure 2.25. (a) Crystal structure of 3-(difluoromethyl)pyridinium lead bromide. (b) Crystal structure of 3-(difluoromethyl)pyridinium lead iodide. Black, purple, grey, blue, green, red, and white balls are Pb, I, C, N, F, Br and H atoms[64]

Lermer et al.[65] reported the synthesis of perovskites with different dimensionality, changing stochiometric ratios of benzimidazolium. This change gives two results: 1D perovskites with $(C_7H_7N_2)PbI_3$ (Figure 2.27), with stochiometric ratio imidazolium and lead iodide 1:1. In contrast a mixture 1D-2D phases with formula $(C_7H_7N_2)_2PbI_4$ was obtained with ratio 2:1 (Figure 2.26b). Crystallographic data and photoluminescence spectra with different broadness of main peaks and different energy gaps underline these differences. In addition, comparison between $(C_7H_7N_2)_2PbCl_4$ (Figure 2.26a) and $(C_7H_7N_2)_2PbI_4$ (Figure 2.26b) shows that perovskite does not change dimensionality changing halide atoms.[65]
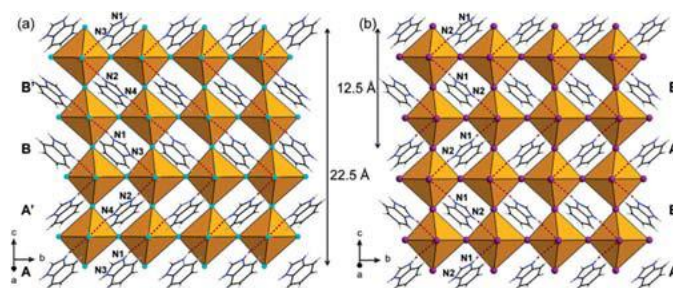
Figure 2.26. Crystal structures of $(C_7H_7N_2)_2PbCl_4$ (a) and $(C_7H_7N_2)_2PbI_4$ (b), view onto the (100) plane Hydrogen bonds are marked with red dashed lines. Nitrogen atoms are labeled exemplarily. C is displayed in black, N is blue H is grey, Pb is orange, Cl is turquoise, and I is purple. [65]
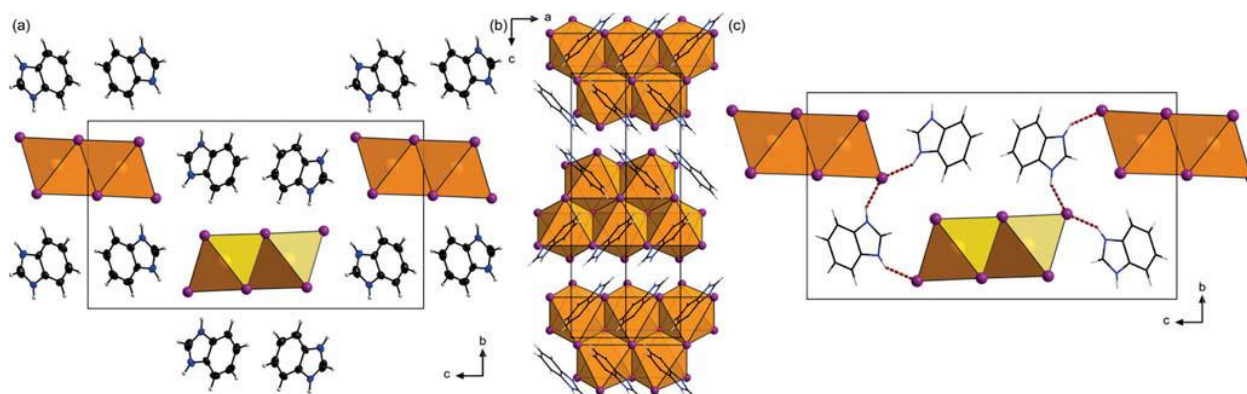
Figure 2.27. Crystal structure of $(C_7H_7N_2)PbI_3$ in projection along [100] (a, c), and [010] (b). Hydrogen bonds are marked with red dashed lines. C is displayed in black, N is blue, H is grey, Pb is orange, and I is purple. Cell edges are marked with black solid lines[65]

So, interaction engineering can be also used to tune low dimensional perovskite structure: different interactions can be added to the ionic one and this allows to create and shape perovskite lattice.

As described in the previous cases hydrogen bonding was the main supramolecular interaction used to tune crystal and electronic structure of low dimensional perovskites. Moreover, new structures were obtained with other type of interaction such as halogen bonding among cations and inorganic sublattice.[66]

In addition, other interaction among cations have been studied, such as covalent bond as crosslinking agent for 2D perovskites or Van der Waals interactions among cations. These additional interactions resulted in an enhanced stability of perovskites.[38]

Aromatic cations can interact among themselves through π effects. Using simultaneously fluorinated and non-fluorinated aromatic cations allows the formation

of strong π- π interactions. This allows to modulate crystal structure, improving optoelectronic properties.[67] Moreover, use of fluorinated functional groups has been reported to give the advantage of a better stability to moisture induced to hydrophobic nature of fluorine parts.[68,69]

In 1D perovskite structure and connectivity among perovskites with same dimensionalities can be modified by different steric hinderance and supramolecular interactions. Regarding steric hinderance in 1D perovskite Goldsmith factor (t) influences type of arrangement, as described from Figure 2.28.
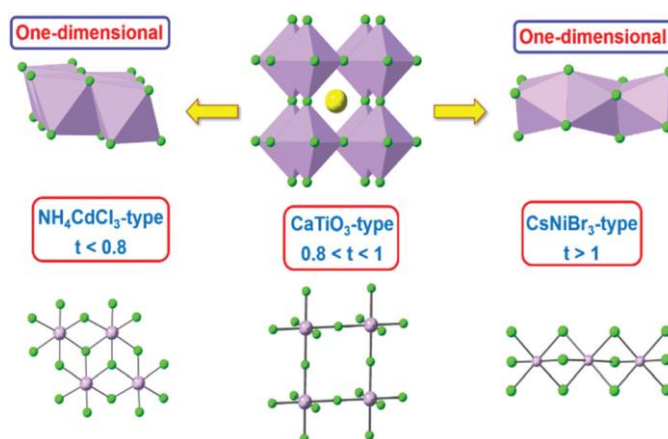
Figure 2.28. Three of the possible structure types with the ABX3 stoichiometry and the tentative tolerance factor relationships within these structures[70]

But these rules can be overcome by supramolecular interactions that template lattice arrangement. For example, imidazolium with t=1 creates a single chain structure CsNiBr₃-type. [71]

Iso-quinolinium and quinolinium organic cation offer an interesting example on how conformation of hydrogen bonding with molecules with same functional groups and steric hinderance can affect space group. These two isomers possess a similar fused ring structure with a change only on position of NH^+ group. However, the inorganic sublattice in case of iso-quinolinium is composed of face-sharing lead halide octahedra chains (Figure 2.29a, b, d), while quinolinium possess a double chain structure (Figure 2.30a, b, d). For Iso-quinolinium a space group Pbca were obtained, while for quinolinium P21/n.[55]

This effect is made from different arrangement of hydrogen bond in perovskite structure that mediates inter-chains interaction in perovskite. Iso-quinolinium structure cannot create H bonds with adjacent organic moieties, there are no direct or indirect H-bonding pathways across the other direction perpendicular to the infinite chain direction. Hydrogen bonds are available, they're stronger with shorter Pb-Br such as Br(1) or Br(3) (Figure 2.30a and c).

Quinolinium has only one hydrogen bond option with Br(1) with shorter length and stronger hydrogen bond acceptor.[55]
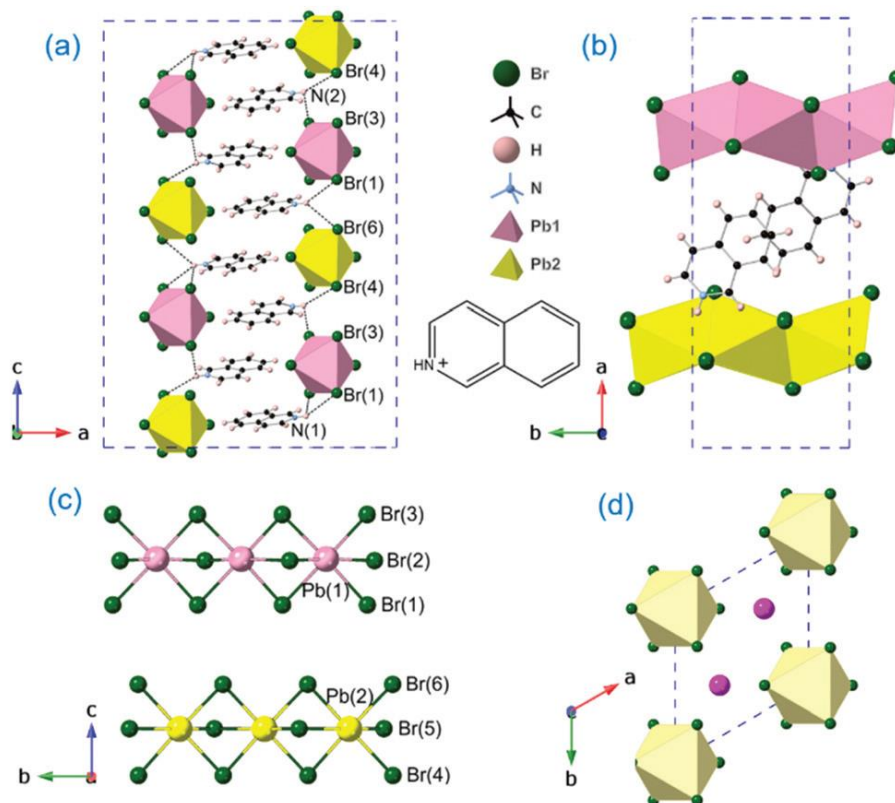
Figure 2.29. The crystal structure of IQPbBr₃ (a) unit cell packing with H-bonding along the b axis (b) along the c axis (c) The two independent 1D face-shared [PbBr₃]∞ single chains along the a axis. (d) The parent 2H structure type [55]
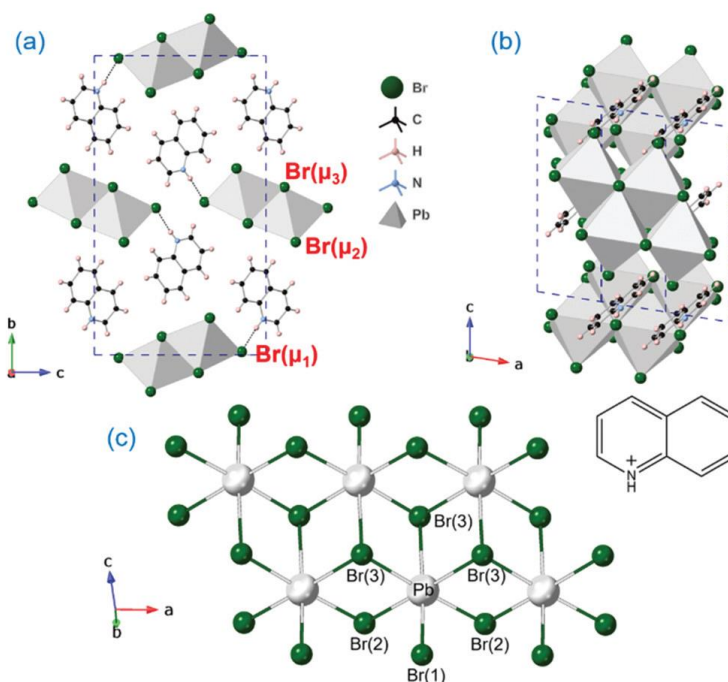
Figure 2.30. The crystal structure of QPbBr$_3$ (a) unit cell packing with H-bonding along the a axis (b) along the b axis, (c) packing diagram of 1D infinite edge-sharing [PbBr$_3$]∞ double-chain for QPbBr$_3$. [55]

Perovskite lattice arrangement is also mediated from type of halogen atoms. Sometimes differences in X atom result in different dimensionalities. One example is given from 3-(R)-pyridinium lead halides (R = CH$_{(3-n)}$F$_n$ (n = 0–3)). Fluorinated methyl groups exhibit 1D structure with lead bromide (Figure 2.31a), while for lead iodide a 2D structure is obtained (Figure 2.31b). CH$_{(3-n)}$F$_n$ group does not interact with inorganic sublattice. So, increasing halogen dimension (from Bromine to Iodine), lattice spacing is modified passing from 1D to 2D structure.[64]
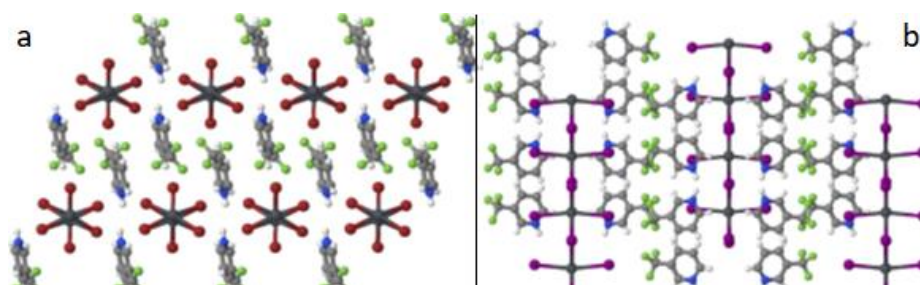
Figure 2.31. (a) Crystal structure of 3-(trifluoromethyl) pyridinium lead bromide (b) Crystal structure of 3-(trifluoromethyl)pyridinium lead iodide. Black, brown, purple, grey, blue, green, and white balls are Pb, Br, I, C, N, F, and H atoms. [64]

Another example of changes in dimensionality given in this case from hydrogen bond with inorganic sublattice is given from aminopropyl-1*H*-imidazolium lead halides with different dimensionalities changing halogen atoms.[59,72]

As described before, 0D structures can be obtained with organic cations possessing rigid and bulky substituents instead of flexible ones. 0D perovskites formation is also controlled by the ratio between bulky organic cations and metal halide.[46,51] This complexity in relation among perovskite dimensionality and cation does not allow nowadays to set rational design rules for low dimensional perovskites. So, a trial-and-error approach is still used. In addition, an overview on structure-property correlation is missing for lower dimensional variants, especially 1D and 0D hybrids.[46]

Before entring in details of optoelectronic properties, it must be remember that materials offer important advantages:

1. **Tunable bandgap** can be obtained by structure modification. The level of dimensionality and geometrical parameters of inorganic sublattice can be tuned by the selection of A organic cations [38]

2. **Different photophysical properties** given from effects such as STEs (Self Trapped exciton, photphysical phenomenon that will be explained later) and exciton binding energy modification given from quantum confinement[46]

3. **Enhancement of perovskite stability,** made from higher formation energy of perovskite (lower formation energy with respect to precursors was reported as dangerous for perovksites stabilty). [73,74] With lower dimensionality perovskites incorporation of bulky cations dynamically stabilize metal halide structures and separate them from environment. In fact organic cation, thanks to their hydrophobic nature act as barrier against degradation induced by oxygen and moisture. In addition, organic moieties enhanced stability by interacting with other components in the crystal lattice at both ground states and excited states. Therefore, intrinsic chemical stability (bigger cations can be less volatile, reducing degradation), strong ionic and other supramolecular interactions, and high formation energy for the bulk crystal, stabilized excited states, are critical requirements to achieve high thermal and photo stabilities of organic metal halide hybrids.[73,74]

4. **Easy processing** like 3D perovskites but with a wider selection of cations[46]

2.2.1 Low dimensional perovskite optoelectronic properties

One of the main advantages of these perovskite is offered from their bandgap tunability, among different dimensionalities or within same one. Bandgap can be affected at **structural level**, with different connection among lead halide units, and at **compositional level**, with effect on selection of metal, halide and organic cation.

In 2D perovskites bandgap is different with respect to quasi-2D structures, given the different number of electronically continuous layers. Decreasing of the number of inorganic layers the bandgap increases and 2D perovskites exhibits the higher value of bandgap. This effect is due to charge confinement in lower number lead halide layers. This effect is visible from the sharp increase of E_b exciton binding energy, (hundred with meV for 2D perovskites) with decreasing dimensionality, given from Wannier-Mott exciton confinement is these systems (Figure 2.32).[75]
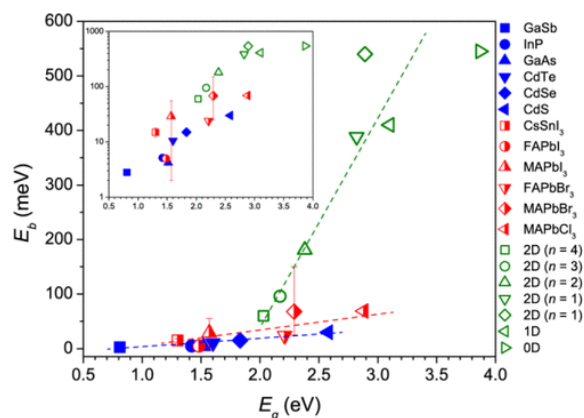
Figure 2.32. Empirical relationship between E_g and E_b in several 3D and LD MHPs and select conventional compounds.[75]

Following this trend, energy gap is increased with lower dimensionalities, passing from 2D to 1D and then to 0D, as shown in Figure 2.32.[75]

At compositional level different contribution must be considered for electronic structure of these materials:

1. **Lead halide composition:** Band edges are mainly determined by the inorganic framework and are produced by the hybridization of Pb and X atomic orbitals. The latter affect the CB edge thanks to their p orbitals. So, passing from Cl to I, bandgap decreases thanks to different electronegativity. In addition, metal with higher electronegativity will result in lower electronic states in band structure. Morevoer, halogen atoms size affects perovskite distortion and orbitals responsible for band structure. It must be considered distortion effect made by increasing dimension from Cl to I, leading a different band structure from

orbitals superposition, as shown in band structure (Figure 2.33) and DOS (Figure 2.34) for Pyridinium lead halides. For example, in pyridinium perovskites changing bromine with iodine results in bandgap from 2.31 eV to 1.57eV. Usually, halogen atom shift is in the order of 0.1-0.8 eV, with different effect made by interaction of organic cations.[53,76,77]
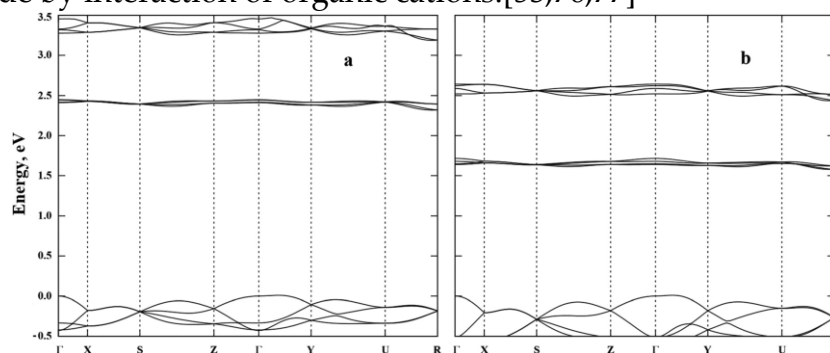
Figure 2.33. Electronic band structures of PyPbBr$_3$ (a) and PyPbI$_3$ (b) [53]
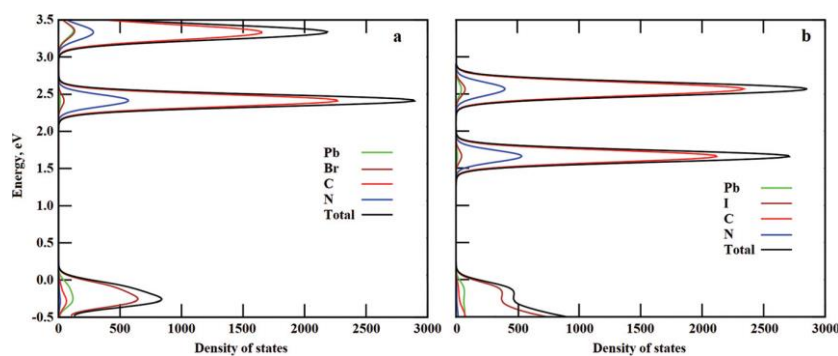
Figure 2.34. Total and projected electronic DOS of PyPbBr$_3$(a) and PyPbI$_3$(b)[53]

2. **Organic cations** affect indirectly perovskite by templating effect on inorganic part. In addition, aromatic organic cations influence band structure and radiative emission of these perovskites.[53,54,58] Organic cations also serve as dielectric moderators that determine the electrostatic forces exerted on the photogenerated electron–hole pairs.[78] In 2D perovkites, carriers' mobility and conductivity can be tuned by the intermolecular coupling between adjacent organic cations, and the energy arrangement between the perovskite transport belt and the oxidation or reduction potential of organic cations.[50]

For example, conjugated organic cations affects the band structure, thanks to the contribution of π-orbitals to the bottom of the conduction bands. As shown in Figure 2.35 a and b, aromatic cations create an intermediate narrow energy level between CB and VB given from antibonding molecular π-orbitals. In

contrast, saturated cations have CB with contribution of halide ions and valence band made from lead's orbitals, with C contribution present in deep conduction band (Figure 2.35c). [53,58]

Functional electron donor or acceptor group can tune the electronic structure of these materials. Some examples are given from OH group linked to pyridinium ring (Figure 2.35d). This group destabilizes the pi-system shifting to low energy narrow unoccupied states.[53,58] However, relation between cation selection and band structure effect is not still clear, affecting bandgap value and direct-indirect semiconductor behavior.[64]
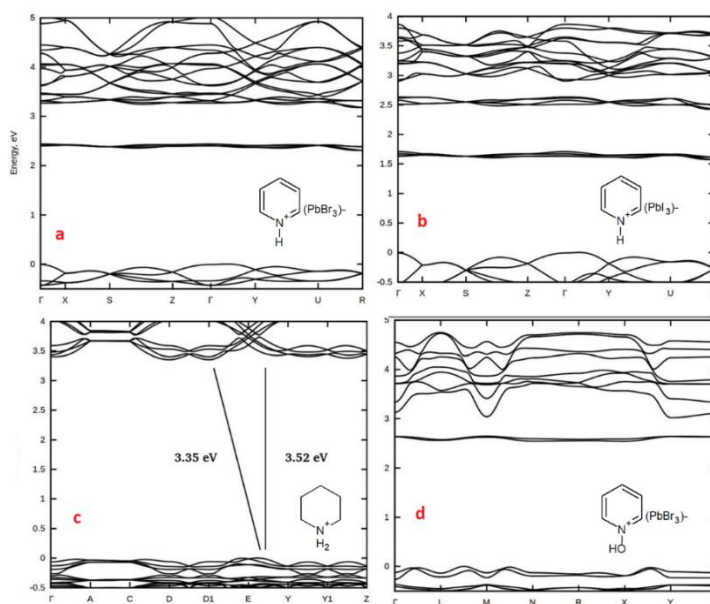
Figure 2.35. 1D perovskite band structure: (a) pyridinium lead bromide, (b) pyridinium lead iodide, (c) piperidinium lead bromide, (d) hydroxy-pyridinium lead bromide[53,58]

So, based on band structure effect, absorption spectra are affected by the distortion of lead halide chains and from the absorption peak of organic species. Inorganic part's distortion affects the bandgap, visible from absorption spectra, where increasing the distortion angle (X-Pb-X), the bandgap decreases.[54] Moreover, emission in low dimensional perovskites can be modified from organic cation's π orbitals and organic sublattice arrangement. As shown in Figure 2.36, typical absorption spectra in UV-Vis contains weak peaks at higher energy given from inter-bands transitions. While absorption peaks slightly lower than absorption edges can be ascribed to excitonic bands. Some differences are present between calculated and real spectra, with absence of peak at high value given from strong interaction between organic cation and halides. Tail in absorption can be related to trap sites made from defects or surface.[54]
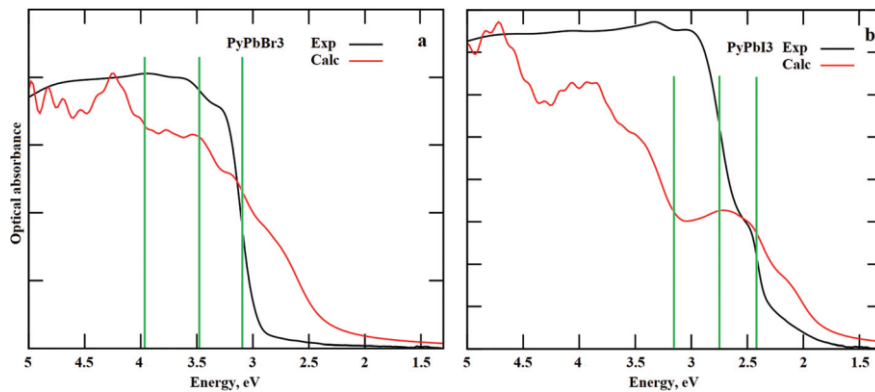
Figure 2.36. UV-Vis spectra experimental and calculated for pyridinium lead halides[53]

Low dimensional perovskites usually have absorption onset around 300-400 nm, with modification of these peaks given from contributions consequences of previously described band structure:

a. halogen atoms (absorption in 300-350 nm UV region for bromine and values shifted to higher wavelength for iodine) (Figure 2.37a)

b. Lead halide sublattice distortion mediated from organic cations: increasing the distortion angle (X-Pb-X), the bandgap decreases[54] (with some examples in Figure 2.37)

c. Intermediate state of organic cations and effect of functional substituents, described from a secondary shoulder in higher wavelength region, as described in Figure 2.37b. These peaks are caused by transition between valence band and pi* states of conjugated cation
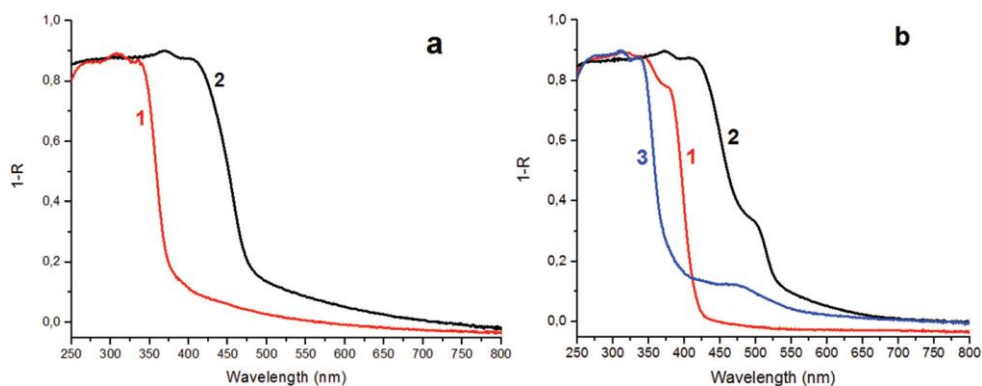
Figure 2.37. Modification of absorption spectra (a) PipPbBr3 (1) and PipPbI3 (2); (b) PyPbBr3 (1), PyPbI3 (2), and 3-OH-PyPbBr3 (3)[58]

In addition, conjugated excitonic peak is modified by interaction with inorganic sublattice. Here, longer wavelengths absorption bands of the perovskites correspond to the electronic transitions from the VB comprised of occupied p-orbitals of halogen anions to the states composed of unoccupied molecular p*-orbitals. [53,58]

In case of saturated compounds, they have absorption in UV region and do not interact with inorganic orbitals. So, they act as silent spectator for the definition of band structure, leading to a higher energy gap based only on lead halide orbitals and their distortion.

Regarding emission of these materials a different photophysical process caused by quantum confinement must be considered with respect to their 3D counterparts. Photoluminescence emission is affected by the creation of self-trapped exciton (STE), made from the interaction of free excitons (obtained from photoexcitation) with lattice vibrational modes (Figure 2.38a)[46,52]

This interaction happens through strong electron-phonon coupling leading to elastic distortions of the lattice in the excited state (Figure 2.38b and c). Different excited states structural distortions are possible due to the soft nature of the lattice leading to multitude of excited self-trapped states. [46,52]

After exciton formation, free charge carriers interact with phonons to form polarons, or self-trapped holes or electrons, that can combine with other electrons and holes to form STE, once the self-trapping energy is larger than half the bandwidth
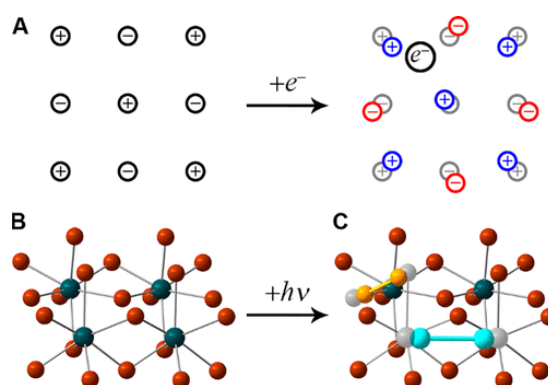
Figure 2.38. A) Schematic of large polaron formation upon adding an electron to an ionic lattice, featuring long-range distortions of the lattice. (B) Fragment of the $PbBr_2$ crystal structure. Green and brown spheres represent Pb and Br atoms, respectively. (C) Schematic of the Br_2^- (orange) and Pb_2^{3+} (turquoise) dimers formed by the self-trapped carriers [79]

Self-trapped excitons are thus like small polarons (charge carriers that induce local lattice distortions made from strong carrier–phonon coupling), although excitons are neutral quasiparticles, and they are uncharged. Self-trapped excitons (STEs) can be

considered as excited-state defects, as they exist only upon excitation, and the lattice distortion disappears following decay to the ground state. STE causes transient lattice distortions without permanent material defects. This can be exemplified by a hard ball (electron/hole/exciton) dropping on a pliable rubber sheet (a deformable lattice). The sheet distorts only due to the presence of the ball, which sinks into a potential minimum it created. Removing the ball returns the sheet to its original state (Figure 2.39).[79]
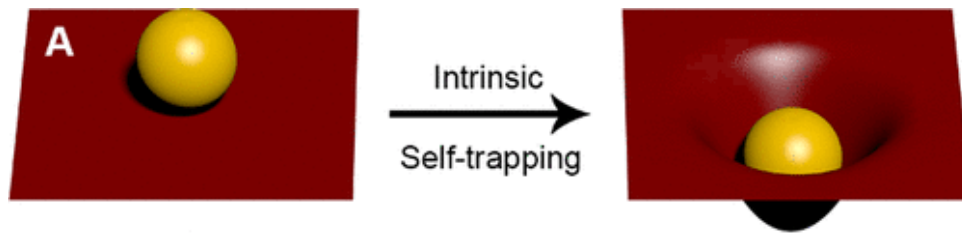
Figure 2.39. Self-trapping represented by a ball interacting with a rubber sheet [79]

So, given multiple minima and free exciton states, population among these states can exchange before decay to ground state (Figure 2.40). [79]
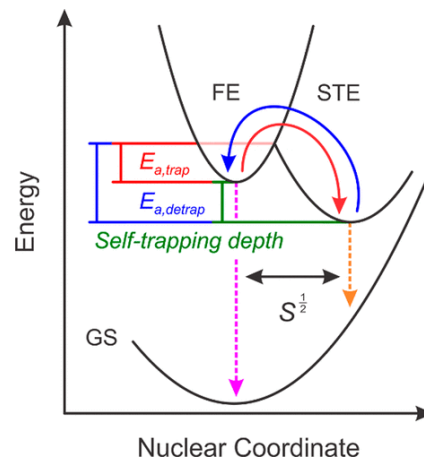
Figure 2.40. Nuclear coordinate diagram for exciton self-trapping (blue) and detrapping (red) in a 2D perovskite (GS = ground state, FE = free exciton state, STE = self-trapped exciton state, $E_{a,trap}$ = activation energy for self-trapping, $E_{a,detrap}$ = activation energy for de-trapping, S = Huang–Rhys parameter). Pink and orange arrows depict FE and STE photoluminescence [79].

This phenomenon results in broadband luminescence spectra different from free exciton emissions the distortion of the self-trapped state with respect to ground state broadens the emission.[46,52]

Both this distortion and the stabilization of the self-trapped state with respect to the un-trapped state (self-trapping depth) contributes highly Stokes shifted radiative emission from STEs to ground state.[46,52]

At very low temperature, the lattice distortion has been reduced, and the STEs would transform back to FEs in the form of ''de-trap'', eventually causing the stronger FE emission.[52] Broadening effect can lead to white light emission or broad color emission in perovskites, that can be useful for lighting application.

Self-trapped exciton in low dimensional perovskite can be described in three regimes:

1. **Low temperature** (usually at T<77K) where trapping and de-trapping mechanism between free exciton (FE) and STE are forbidden with thermal energy lower than binding energy of trapped state, with narrower PL and lower Stoke shift (Figure 2.41g, first graph). The only contribution to STE emission can be given only by tunneling effect independent from temperature.[80,81]
2. **Intermediate temperature**, where only trapping mechanism is activated, so radiative recombination starts from multiple minima of STE, creating stronger Stoke shift and broader PL peak (Figure 2.41g second graph). Here PL signal is dependent from temperature, due to thermal energy required for trapping mechanism. These phenomenon explain spectra for trans-2,5-dimethylpiperazinium obtained at room T, shown in Figure 2.41a with explanation of photophysical process in Figure 2.41d. [80]
3. **At higher temperature** both trapping and de-trapping mechanism are both activated and thermal equilibrium between these two states is achieved (Figure 2.41g third graph). Photoluminescence emission is dependent by temperature, with a decreasing of STEs PL intensity in favor of FE peak at higher temperature, this effect is visible at room T for lead bromide and lead chloride, as depicted in Figure 2.41e and Figure 2.41f. [80,82]

These three regimes start at different temperature depending on trapping and de-trapping energy, values affected from halogen atoms, decreasing this barrier from passing from chloride to iodine. This effect results in different shapes of PL signals as shown in Figure 2.41. This effect could originate from the different deformation potentials of the lattice induced by different M–X bonding. While bandgap decrease with halides dimension influence energy level of free excitons, reducing de-trapping energy. So, passing from Chloride to Iodine, third regime appears at lower temperature, favoring narrower FE emission. On the other hand, interconversion between STE and FE reduce the number of non-radiative recombination leading to a

higher PLQY, but still correlation with composition and structure must be investigated more in depth.[80]
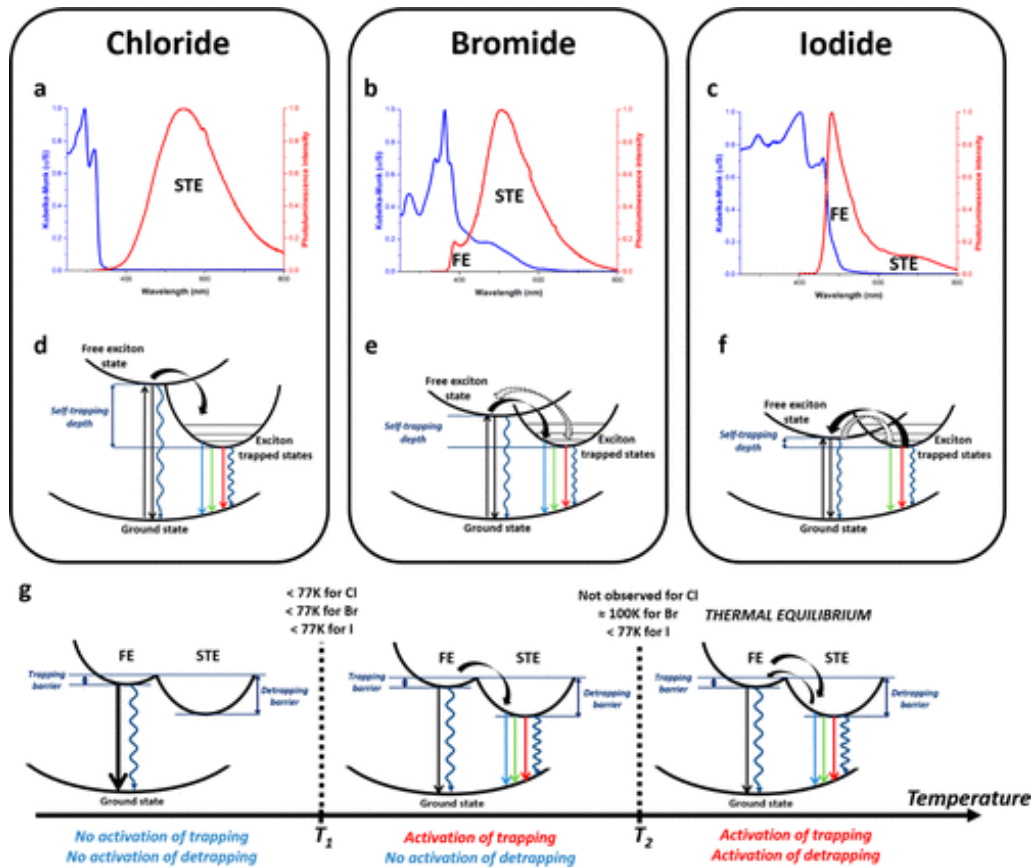
Figure 2.41. Kubelka–Munk absorption and emission spectra at room temperature for (a) chloride, (b) bromide, and (c) iodide compounds Representation of the trapping and de-trapping processes of the excitons for (d) chloride, (e) bromide, and (f) iodide compounds. (g) Schematic evolution of the trapping and de-trapping processes with temperature.[80]

Even 2D materials exhibits STEs, self-trapping and efficient generation of broadband emissions are more effective with 1D perovskite. This phenomenon is explained from the easier distortion for lower dimensional system, which can hinder the formation of free exciton, resulting in an enhanced and broader photoluminescence. However, this smaller dimensional system can suffer defect induced emissions. [46,83]

A condition for self-trapped exciton is given from large trapping energy possible only with soft atomic bonding with low energy of distortion (Ed).[84]

Self-trapped exciton emission in low dimensional perovskite is affected by distortion of lead halide units, that can be quantified with two parameters: Pb-X bond length distortion (Δd, Eq.3a) and X-Pb-X angle distortion (described in Eq.3b). [54]

$$\Delta d = \frac{1}{6}\sum_{n=1}^{6}\frac{1}{d^2}\left(dn-d\right)^2 \textit{(3a)}$$

Δd is calculated from the Pb-X average distance (d) with respect to distance of every Pb-X bond (Figure 2.42), giving a mean parameter of lead halide octahedra distortion.[54]

$$\sigma^2 = \frac{1}{11}\sum_{n=1}^{11}(\alpha n - 90°)^2 \textit{(3b)}$$

σ^2 is calculated from standard deviation of X-Pb-X angle (Figure 2.42) with respect to undistorted value for lead halide octahedron (90°).[54]
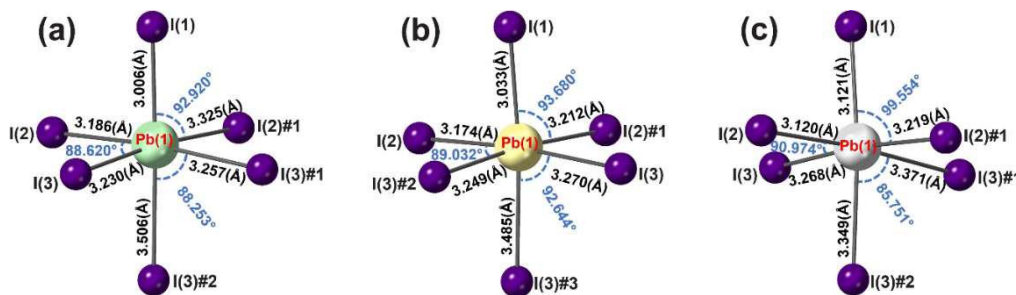
Figure 2.42. examples of distorted Lead halide bond length (black number) and bond angle (light blue dotted arrows)[85]

These values of distortions are related to the type of connectivity and dimensionality, with higher reported values for the 1D face sharing octahedra.[54] Distortion parameters, as observed from Mao, are relate to width of photoluminescence peak. This effect was generalized by 2D perovskites emission, and it's related to lead halide chains distortion with STE emission.[54,86]

Photoluminescence emission has been studied as important optical properties for lighting application and study of carriers' behavior under photoexcitation. In addition, use of conjugated cations can create relaxation path involving pi*states with effect on photoluminescence.
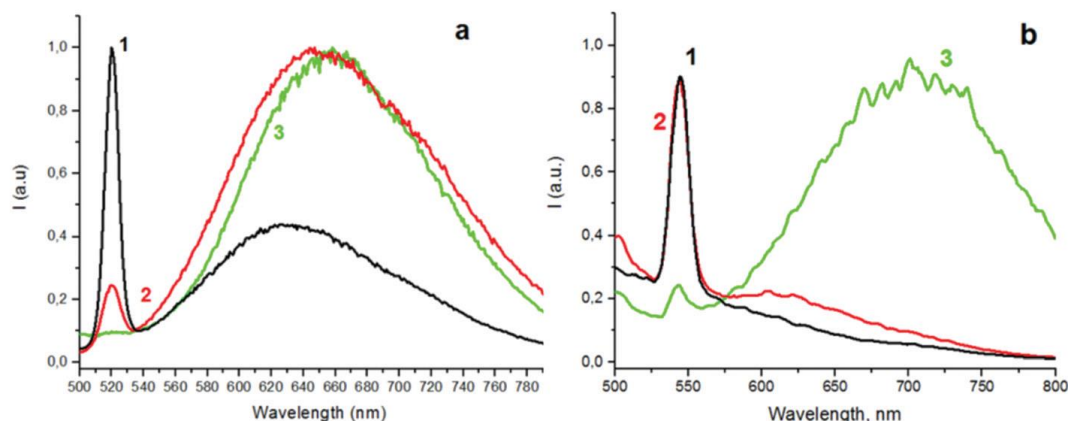
Figure 2.43. PL spectra of monocrystalline PyPbBr3 (a) and 3-OH-PyPbBr3 (b) at T = 77 K; λexc: 390 nm (1), 365 nm (2), 330 nm (3), t = 77 K [53]

For example, PL of pyridinium perovskites at 77K (Figure 2.43 b2 and a2) shows a broad luminescence peak around 650 nm, made from emission related to Self-Trapped exciton. An additional narrow peak is present at lower wavelengths (in the case of pyridinium perovskite at 550 nm), made from emission caused by transition between π^* levels to VB. STE band decreased with longer wavelength while the band associated with π^* transitions increase. [58] Peaks change is made from the emission from π^*-orbitals directly from absorption at lower energy or through non-radiative recombination from the bottom of CB. These spectra are red shifted with functional groups lowering the energy of π^*-orbitals. [58] It must be noticed different dimensionalities of the two perovskites, PyPbBr$_3$ is a 1D structure, while 3-OH-PyPbBr$_3$ is a 2D perovskite. [58]

In some cases, due to strong interaction between organic and inorganic electronic subsystem or the presence of heavy iodine atoms, the PL spectra can be only related to lead iodide chains even with conjugated cations. [53]

So, conjugated cations perovskites feature the following transitions in STE equilibrium regime:

1. Self-trapped exciton, with transition between lead halide chains, affected from distortion and halide atoms, these transitions broaden and shift the peak related to lead halide chains, these effect becomes stronger with 1D perovsktie thanks to lower distortion energy
2. Transitions inside inorganic sublattices in low dimentional perovskites (absorption in UV) and a luminescence spectrum in 550-650 nm

3. Transitions between cation's energy levels and VB, with absorption at longer wavelengths and luminescence at lower wavelengths than STE depending on organic cation [58]

As described in Figure 2.44, cation energy levels can be populated not only directly by wavelengths for direct transitions, but also through excitation of inorganic chains followed by electronic transition from the conduction band to π^* orbitals. These transitions can be tuned with functional groups, for example π^* energy level can be lowered with electron donating OH group. [58]
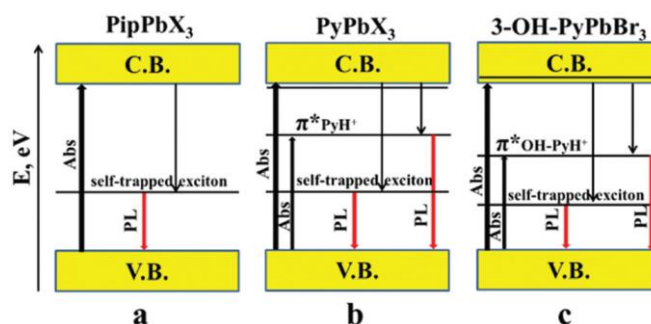
Figure 2.44. The scheme of photophysical processes in 1D- perovskite materials: PipPbX$_3$ (a), PyPbX$_3$ (b), 3-OH-PyPbBr$_3$ (c), here X – Br and I [58]

However, not all paths give radiative transitions related to π^* excited states. Indeed, coupling between vibration of inorganic lattice and pi* relaxation can create non-radiative recombination.[58] In addition temperature effect must be considered to lower this coupling and obtain different relaxation paths.

Photoluminescence of perovskite can also be modulated from pressure application, with induced phase transitions. Pressure application (GPa) reduces non-radiative recombination, localizing STE, with reduced scattering among defects and phonons.[87]

Based on STE emission these perovskites have been studied for light emitting diodes, thanks to presence of self-trapped exciton. In this case to obtain a broad PL peak, distortion of inorganic lattice was increased thanks to arrangement made by intermolecular interaction. Other application like photodetectors, lasers and X-ray scintillators have been studied. 1D perovskite have been found more interesting for this application, thanks to stronger STE effect in respect to other dimensionalities.[46] Before focus on 1D perovskites (section 2.2.2), a brief discussion about fluorination of organic cations was made. These cations were found promising for passivation of 3D perovskites in 2D/3D mixed perovskite with enhanced stability. In this application, conductivity among lead halide planes becomes important for overall device performance. [88]

2.2.1.1 Low dimensional perovskites with fluorinated cations

Fluorination of organic cations offer an interesting strategy to tune low dimensional perovskite and their optoelectronic properties. In case of 3-(R)-pyridinium lead halides (R = $CH_{(3-n)}F_n$ (n = 0–3)) bandgap decreases with fluorination of methyl group. This effect is made from the increasing of electron acceptor stability of methyl group adding fluorine as electron-attractor. [64] So, larger shift in electronic density of pyridinium's π-system towards the fluorinated methyl group, which decreases Pyridinium stability, increasing energy of π-system in VB. Fluorination results in bandgap decrease from 2.24 to 1.77 passing from methyl to trifluoromethyl substituent. Moreover, with steric hinderance of iodide as halogen, bandgap is affected also by change of dimensionality. Indeed, 2D perovskite were obtained with fluorination of R group, as described in section 2.2. [64]

Fluorination was also exploited to change the electron distribution in aromatic compounds, thanks to their strong electronegativity. As computed from DFT calculation of Wang et al.[69], degree of fluorination and position of fluorine in aromatic cations create different electron distribution in phenylethylamine (PEA), as shown in Figure 2.45. These results in different packing of these cations in 2D perovskite layers on 3D perovskites. Better results in terms of PCE and stability for solar cells were obtained with fluorination, thanks to strong dipole moment that reduce charge recombination. Moreover, moisture is enhanced by hydrophobicity induced   by   fluorine   atoms.[69]
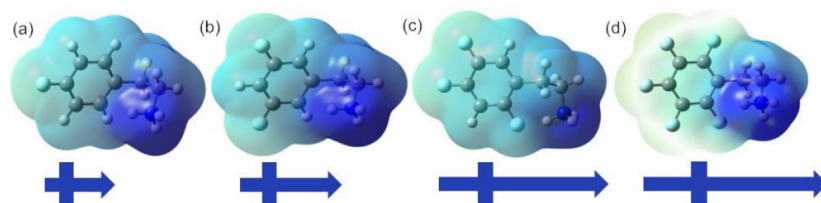
Figure 2.45 . DFT calculation results of the ammonium salt, with electrostatic surface potential of PEAI (a), F_2PEAI (b), F_3PEAI (c), and F_5PEAI (d) (blue arrow length is the molecular dipole moment)[69]

Effect on fluorine substituents on aromatic ring were investigated for *Ortho-*, *meta-*, *para-* and *per-*fluorinated benzylammonium 2D perovskites. They exhibit different structural symmetries and packing, due to the larger steric hindrance between adjacent cations, together with enhanced phase transition temperature and changed polarization. *Ortho-*substitution and *per-*fluorination showed large piezoelectric response and excellent ferroelectricity, due to the changes in intermolecular forces and dipole moments.[89,90]

Zhang et al.[88] compared in 2D perovskite 4-fluorophenethylammonium (F-PEA) instead of phenethyl ammonium (PEA). Fluorination results in a different electron density distribution over aromatic cation. This effect results in a different intermolecular packing of aromatic cations, with slip-stacked rings induced by fluorination effect on π interactions (Figure 2.46b). While phenethyl ammonium cations are organized in edge-to-face order (Figure 2.46c). As a result, conductivity between lead iodide planes was enhanced, also given by perovskite sheets alignment.[88]
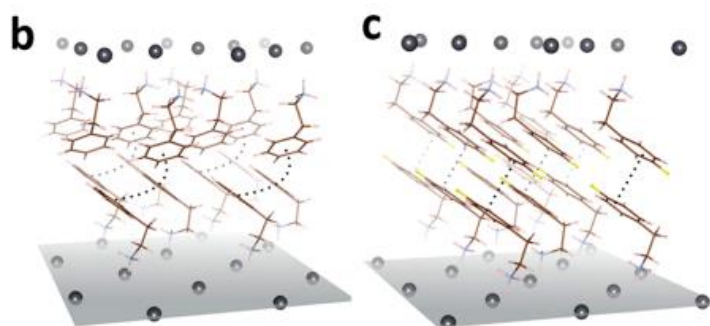
Figure 2.46 Structures of (b) $(PEA)_2PbI_4$- and (c) $(F-PEA)_2PbI_4$- single-crystal [88]

Moreover, fluorinated aromatic rings with halogen atoms were used to exploit halogen bond in perovskite, thanks to the strongly electronegative fluorine atoms. They attract the delocalized electronic cloud of the aromatic ring and induce the formation of a region of positive potential along the same direction of XB bond, rendering the interaction highly directional.[66,91]

Perfluoroalkyl chains with linked an ammino group (Figure 2.47) does not act directly on 2D perovskites bandgap value (given the absence of π effect and different induced polarization). However, using linear chains instead of branched CF_3 groups, energy gap decreases. This effect was made from packing of these chains that shapes lead iodide distortion, with additional rigidity. [92] Moreover, different distortion of lead halide sublattice results in bandgap openings with fluorination.[68]
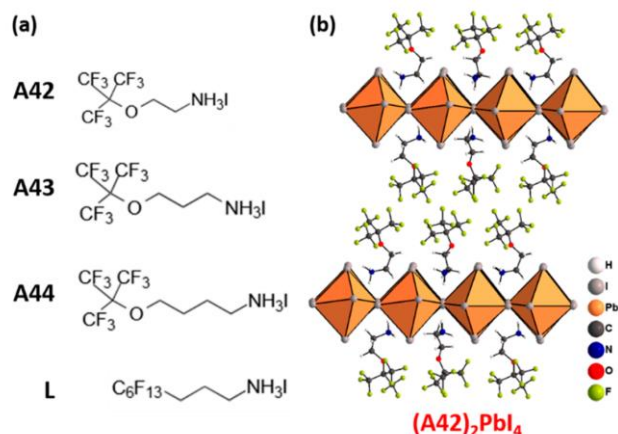
Figure 2.47. (a) Molecular structure of fluorosis cations with abbreviated names(b) Schematic structure of 2D hybrid perovskite[92]

These perovskites can take advantage of hydrophobic effect made by fluorinated chains. This effect was reported as beneficial in terms of moisture resistance. Therefore, devices' performance stability was enhanced using fluorinated cations.[68]

However, effect of perfluoroalkyl chains with aromatic cations has not been studied yet.

2.2.2 One dimensional perovskite optoelectronic properties and related application

One dimensional perovskite optoelectronic property can be described with previous observation on low dimensional perovskites, with some properties modified by lead halide chain structure inside their lattice.

First it must be noted that band structure and optoelectronic properties in 1D perovskite are affected by lead halide chains thanks to their distortion and connection among octahedra, with different effects based on halide atoms[53,54]

Passing from corner sharing to face sharing, perovskite bandgap increases. From a geometrical point of view higher the X-Pb-X bond angles in the hybrid perovskites narrower is the band gaps. Although the number of hopping pathways for carriers between neighboring Pb ions increases, the paths become less favorable. This result in an increase of bandgap, as shown in Figure 2.48. [53,93]
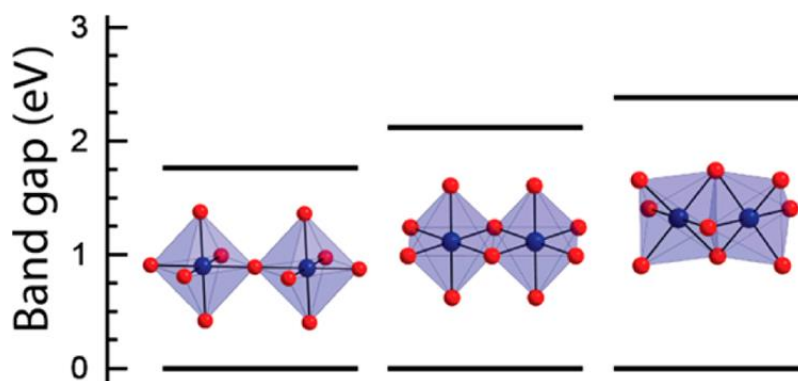
Figure 2.48. Approximate Band Gaps (eV) of with Different Connectivity and Dimensionality of lead halide chains[93]

In 1D perovskites, electronic transitions proceed from the occupied p-orbitals of halogen anions to the vacant p-orbitals of lead cations and halogen anions of 1D inorganic chains, responsible for onset of absorption.[58] Then peaks at very low wavelength (200-300 nm, far UV, as shown in Figure 2.49) can be ascribed to organic cation, while the peak slightly lower than absorption edge is related to exciton binding energy of the system. [54]
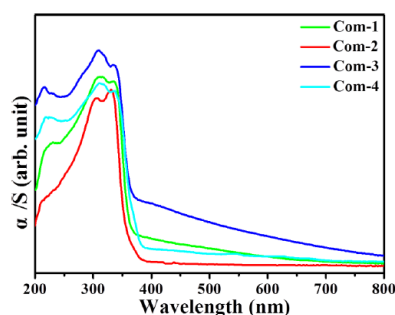
Figure 2.49. Absorption spectra of APbBr3, com-1 1,8- diazabicyclo[5.4.0]undec-7-ene; com-2, 5,5-dimethyl-1,4,5,6-tetrahydropyrimidine, com-3 1,5-diazabicyclo[4.3.0]-5-nonene; com-4 ethylpiperidine) [54]

In one-dimensional perovskite lattice distortion is easier with respect to higher dimensionalities, creating a more stoke-shifted emission that covers broader wavelengths. [84] Stoke shift allows to emit visible light upon UV excitation with a broad band, while PLQY can change based of distortion degree and lattice arrangement. [84]

These materials exhibit a broad band emission under UV photoexcitation (Figure 2.50a). Effects of different parameter (i.e., T or perovskite composition) have been studied in terms of FHMW (full width half maximum), intensity and wavelength of PL signal (Figure 2.50a).
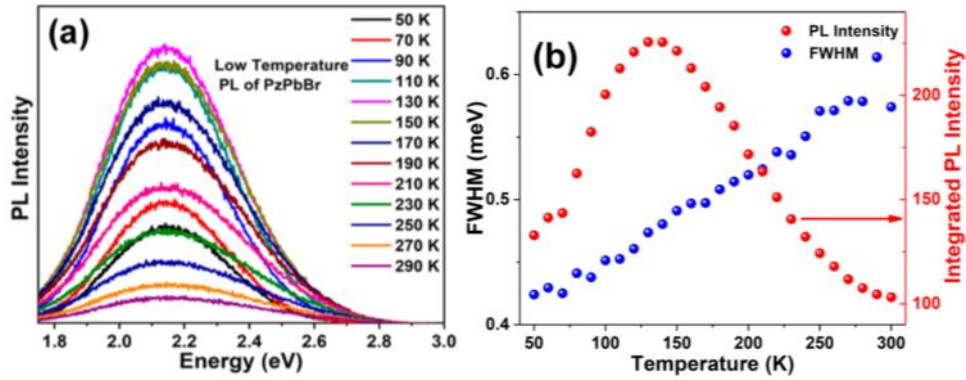
Figure 2.50. (a) Steady state low temperature PL of PzPbBr; (b) temperature
dependence of PL intensity and bandwidth.[81]
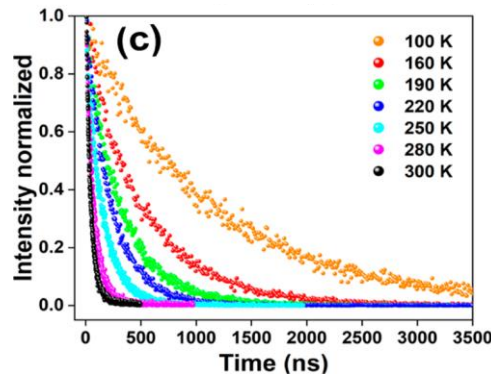
Figure 2.51. temperature dependent lifetime of PzPbBr [81]

Moreover, some articles reported a deeper study of PL signal evolution with relaxation
time. At room T, PL lifetimes between 0.1 and 10 ns indicates the faster exciton
recombination rate and higher contents of nonradiative decay in the exciton decay
process, that can be tuned with different organic cations. Given the fact that PL
intensity and PL lifetime are related to STE emission, both parameters are usually
enhanced at low temperatures (Figure 2.51).[54,81]

From broadband light emissions of hybrid low-dimensional perovskites it has been
demonstrated that the electron-phonon coupling will enhance with decreasing
temperature and simultaneously results in narrowing of band width. This
phenomenon can be described with eq.1

$$\Gamma(T) = \Gamma 0 + \Gamma_{phonon}(e^{(\frac{E_{LO}}{k_bT})} - 1)^{-1} + \Gamma_{inhomo}e^{(\frac{-E_b}{k_bT})} \ (1)$$

Where $\Gamma 0$ is the FHWM at 0 K or a reference temperature. Γ_{phonon} represents electron
phonon-coupling term, which is mediated, in case of 1D perovskites, by the
temperature through E_{LO}, the energy contribution of longitudinal optical phonon

mode. Strong electron phonon coupling is confirmed by fitting data, with reported value around 145 cm^{-1}, frequency of lead halide stretching in Raman. Γ_{inhomo} represent inhomogeneous broadening of STE, that is mediated by binding energy of trapped states (E_b).[81,94]

However, differently from band structure, PLQY is not directly correlated with lead-lead distances. For example, PLQY was reported in 40-60% range both with corner sharing and face sharing structures. But distortion of the individual metal halide unit (bond length distortion, bond angle distortion, degree of off centering distortion) affects emission efficiency.[46] As described before, thanks to thermal equilibrium between self-trapped exciton and free exciton states, different minima for radiative recombination are created, with an effect of stoke-shift and broader PL emission, that can be useful for white-light phosphor.[46]

However, STE is the necessary condition for the creation of a broader band for photoluminescence spectra in 1D perovskites, but the creation of a broad band is made from the creation of Jahn-Teller octahedral distortion for excitons (with the removal of degenerate energetic state with the distortion). In other configurations, the relaxation of photoexcited state is given from non-radiative recombination (Figure 2.52). [95]
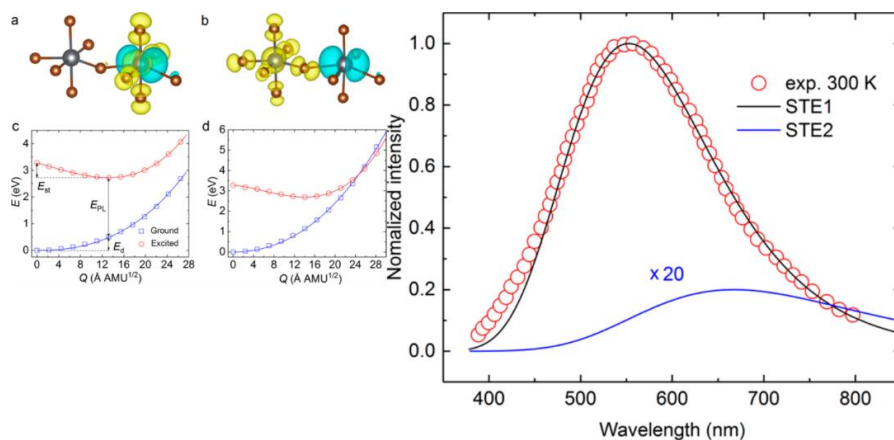
Figure 2.52. (a) Jahn-Teller and (b) non-Jahn-Teller distortions, with energy diagrams (c) and (d), with (e) difference among photoluminescence spectra[95]

1D perovskites binding energy of trapped states passes to lower values with respect to higher dimensional perovskites thanks to easier distortion of lead halide chains.[46] On the other hand, dimensionality also affects temperature effect on self-trapped exciton located in inorganic sublattice. Regime of thermal equilibrium between trapping and de-trapping mechanism, energy is described with Arrhenius plot. (eq.2)[81]

$$I(T) = \frac{I_0}{1 + Ae^{-\frac{Ea}{kbT}}} \quad (2)$$

Where A represent the ratio of the radiative to nonradiative lifetime at high temperatures, and Io the integrated signal at threshold temperature for this regime. Activation energy (Ea) is obtained with interpolation, and it represents the energy to crossover non-radiative path. In case of 1D perovskites, values were reported between 150 and 200 meV, higher than perovskites with more extended dimensionalities, thanks to exciton self-trapping and radiative recombination were favorable in this regime. [82,96]

As described in general for low dimensional perovskite, use of aromatic cations can change optical properties with temperature in 1D perovskite due to effect to transition involving pi* orbitals of cations.

According to Wan et al.[62], decreasing temperature inside the thermal equilibrium regime, not only increase photoluminescence, but also increase the value of peak related to π-π^* transitions at temperature lower than 100 K (as shown in PL spectra in Figure 2.53b). Over 100K this peak is quenched by non-radiative internal conversion. Under 100K the dynamic motion of the cations resulted in the excited state relaxing to the ground state through the non-radiative internal conversion, which is frozen at temperatures below 100 K. This phenomenon results in a different color according to CIE diagram in Figure 2.53d.[62]
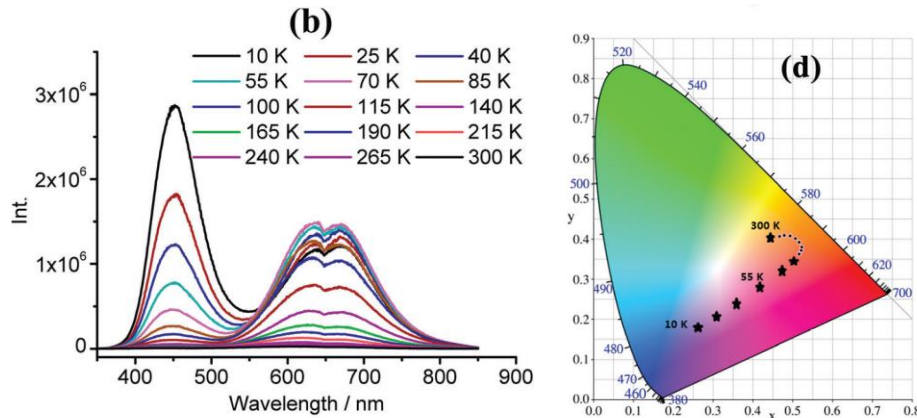
Figure 2.53. (b) emission spectra of 1-hexyl-3-methyl-imidazolium lead bromide, (d) CIE chromaticity diagram showing the fluorescence color at selected temperatures[62]

Despite the research about 1D dimensional perovskite is mainly focused on the investigation of structure-property relation, some application based on previously described properties have been started to be explored.[46]

As described before, 1D perovskite can give values of PLQY as phosphors up to 60-40% depending on different cases. So, PLQY values are not optimized because of design rule that must be investigated for these devices. Moreover, different colors LED

were reported for these perovskites However, thanks to self-trapped exciton process and coupling with free exciton at room temperature, PL emission results broader than perovskites with higher dimensionalities, keeping these materials interesting for white light application, even if PLQY is still low. To broaden emission of these materials strategies such as doping with Mn^{2+} was used, obtaining PLQY around 28% and different colors (Figure 2.54b and b). [46]
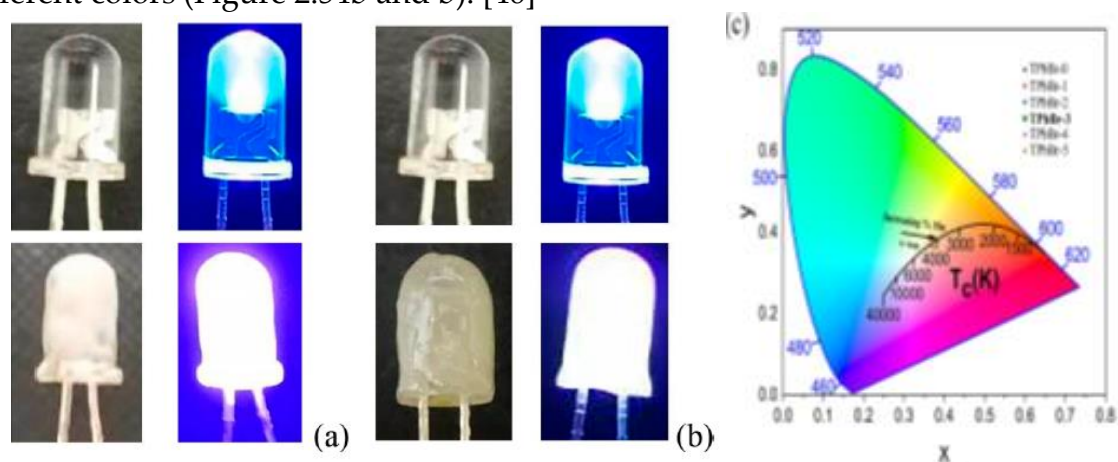
Figure 2.54. Photographs of the blue LED and WLED device fabricated with 1,3-bis(4-pyridyl)-propane (BPP) (a) lead bromide and (b) lead chloride (c) CIE coordinates for trans-2,5-dimethylpiperaziniium lead iodides with different Mn doping[46,97]

Given the explored possibility of a broadband emission from solution processable materials, 1D perovskite main application is related to the fabrication of LED. The previously described PL spectra suggested the use of these perovskites as single component phosphors for UV-pumped white LEDs, thanks to broad emission originated from STE and quantum confinement. White-light-emitting from a single emitter layer simplifies the device structure and avoids problems, such as self-absorption and color instability in hybrid emitters and multiple emitters.[98]

This solution allows to obtain broadband optically pumped white LEDs, with a change in emission color tuning organic cations properties, as obtained from Sun et al. [97] but still with PLQE around 5-8% (Figure 2.54c). So, investigation of organic cations selection becomes a fundamental point for new perovskite devices.[97]

Moreover, thermochromism of 1D perovskites with aromatic cations must be fully understood to study possible application of these materials as thermometer at low temperature thanks to this property. [62]

1D perovskites have also been studied as absorber material for solar cells. However, Xu et al.[99] obtained very low PCE (0.3%) using pyridinium lead iodide perovskite. This effect is given by high bandgap of material and low mobility that results in a Jsc of 0.94 mA/cm². In addition, energy level of solar cells materials must be further

investigated to prevent loss by high offset. But from this experiment a higher stability of perovskite solar cell has been proven in ambient condition with respect to other 3D solar cells. [99]

Starting from this advantage, Ma et al.[100], studied mixed solar cell, with 1,4-benzene diammonium lead iodide (BDAPbI₄), mixed with methyl ammonium as organic cations. Here, inorganic chains serve as isolation among 3D domain composed from Methyl Ammonium perovskite (Figure 2.55b and d), as described from the lower wavelength of absorption spectra and lower carrier confinement described from Time resolved PL. Absorption and emission spectra (Figure 2.55a) were modified by 1D perovskite but not significantly, while XRD prove different peaks by incorporation of various quantity of BDA as cation (Figure 2.55d) [100]
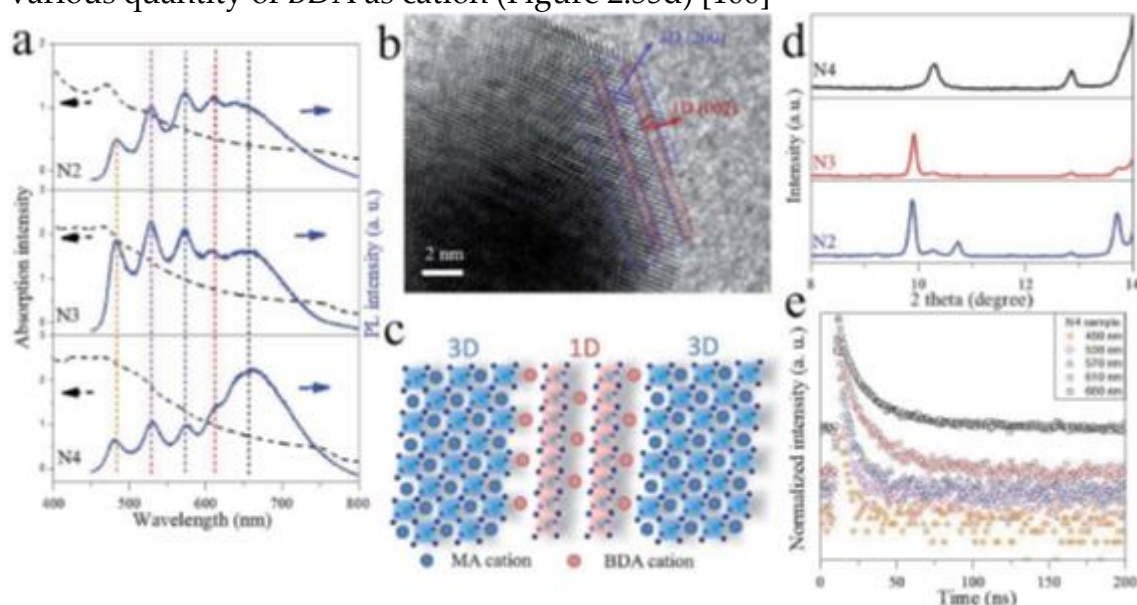
Figure 2.55. (a) Absorption (dashed lines) and emission (solid lines, excited at 380 nm) spectra of N2, N3, and N4 perovskite thin films. (b) HRTEM image of the N4 sample. (c) Schematic illustration of the proposed isolation effect of 1D perovskite. (d) XRD patterns of N2, N3, and N4 perovskite thin films. (e) trPL decay profiles from N4 perovskite thin films. [100]

Despite the quantum confinement effect obtained, performances of solar cells with composition BDAPbI₄: 4 MAPbI₃ shown efficiency up to 14%, while with lower ratio MA-Perovskite/BDA perovskite a significant decrease in PCE was measured. [100]

In addition, the use of 1D perovskites stabilized performances of solar cells under illumination and heating with respect to all-3D perovskites, proved from reported stable PCE under illumination and higher temperatures (Figure 2.56). [100]
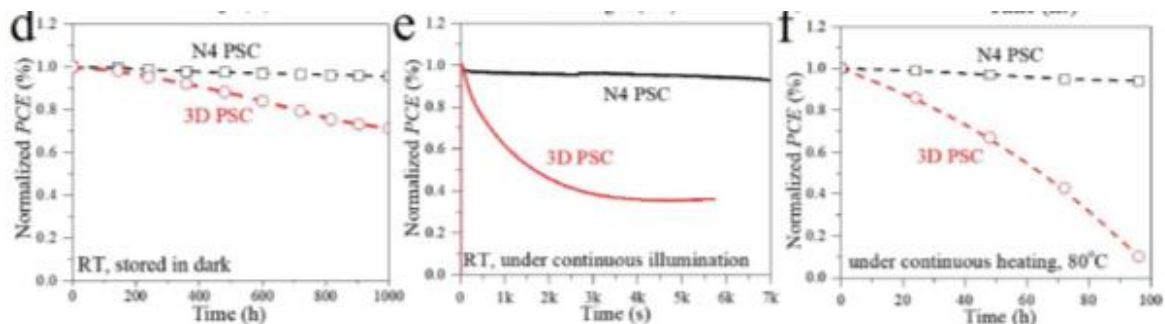
Figure 2.56. (d) Storage stability measurement (e) Operational stability measurement of under continuous illumination and maximum power-point at RT with encapsulation f) Storage stability measurement continuous heating at 80 °C and 85% RH with encapsulation [100]

New application of 1D perovskites have been studied, however they're only at preliminary stage and they should be better understood. For example, 1D perovskites was studied as photodetectors and scintillator. [31,101] 1D perovskites offer a faster decay and larger stoke shift with respect to higher dimensionality. These features were used for study of scintillator for X-rays and alpha particles, with high light yield. These applications required high quality single crystals in wider area, difficult nowadays to be obtained.[31]The scope for applications of 1D hybrids perovskite need to be widened to include luminescent sensors, remote thermography, anti-counterfeiting, and energy storage platforms.[46]

In addition, some studies report water and acetone detectors based on low dimensional perovskites, thanks perovskites phase transitions. Given perovskites phase transitions, resistive switch application can be a future application of these materials.[98]

However, before a complete integration of 1D perovskites in optoelectronic and down conversion application a deeper study of structure-properties relationship must be carried out. Then further step will interest large integration in LEDs devices to understand total PLQE of these devices.

2.3   Imidazolium in perovskite

This work investigates effect of incorporation of different imidazolium cations in perovskite structures a Before going deeper in literature on this topic, general characteristics of these molecules are discussed along with how they have been used in perovskite's field.

2.3.1 Imidazolium overview

1-alkyl-methyl-imdiazolium iodides are a well-known family of ionic liquids with alkyl chain length higher than 2. [102] Increasing the length of alkyl chain in position 1 it is possible to tune thermal and functional properties of such materials. In fact, with alkyl chains longer than 11 carbon atoms it is possible to obtain a liquid crystalline behavior.1-dodecyl-3-methyl-imidazolium (C_{12}ImMetI-) iodide exhibits a liquid crystalline behavior with a smectic A phase (melting point 80°C) due to dodecyl chains interdigitation. These materials thanks to their good conductivity and good thermal stability have been reported for electrolyte in DSSC, thanks to alignment of alkyl chain that creates a path for iodine ions (Figure 4.3). On opposite ionic liquids cannot be used for DSSC solar cells thanks to difficult charge transfer of charge made by their disorder and low mobility.[103,104]
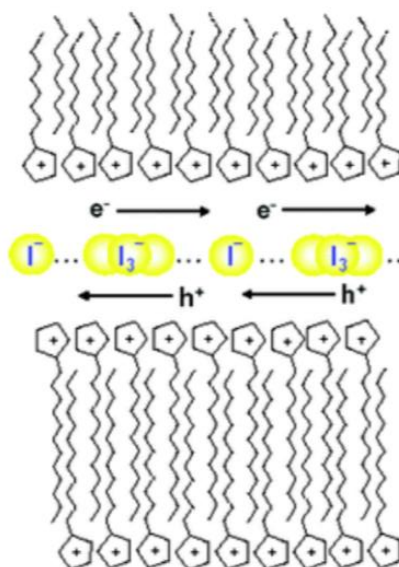
Figure 2.57. Smectic phase model for conduction in C_{12}ImMetI- LC phase [103]

Another interesting alternative is given from perfluoroalkyl-methyl-imidazolium salts. Inside this category, 1-Methyl-3-tridecafluoroctyl-imidazolium iodide Figure 2.58(a)) and 1-Methyl-3 tridecafluorononyl-imidazolium iodide (Figure 2.58(b))

undergo to a phase transition to smectic phase respectively at 94°C and 86°c as described in Figure 2.58.[105,106] These transitions were attributed to an increase in order for these structures induced by fluororous-fluorous interaction of perfluoroalkyl chains. Therefore, these materials offer a thermotropic liquid crystalline behavior mediated by interdigitation of fluorocarbon chains. [106]

Solid→94°C→Smectic phase A→224°C→isotropic liquid

Solid→86°C→Smectic phase A→198°C→isotropic liquid
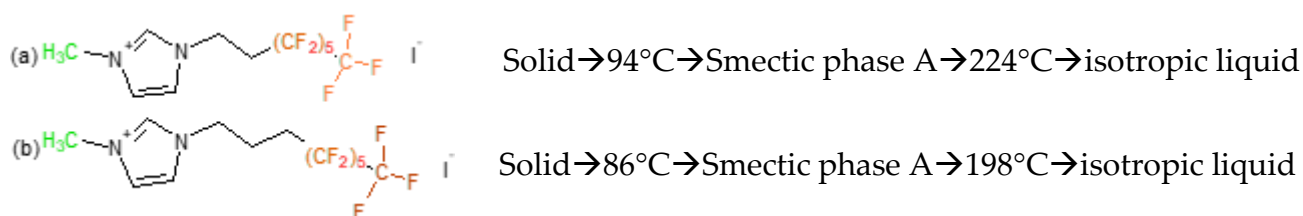
Figure 2.58. 1-Methyl-3-tridecafluoroctylimidazolium iodide ($C_8F_{13}ImMetI-$) and 1-Methyl-3-tridecafluorononylimidazolium iodide ($C_9F_{13}ImMetI-$) and their phase transitions. [105,106]

Conductivity was enhanced order induced by these chains, also in liquid crystal phase (orientation was obtained after cooling for these materials). Moreover, HOMO and LUMO are affected from perfluoroalkyl chains effect. [88,107] This effect with an ordered liquid crystal phase improves the charge transfer dynamics at the TiO_2-dye/electrolyte interface and the transport in the electrolyte solution. These results make perfluoroalkyl functionalized imidazolium interesting cations. [105,106] However, perfluoroalkyl imidazolium cations in perovskite have not been studied yet.

2.3.2 Surface and defects passivation with imidazolium salts

Imidazolium iodide has been studied as passivating agent for 3D perovskites, thanks to possibility of passivation given from N atoms that act as Lewis's base to passivate undercoordinated Pb. While substituted imidazolium salts were used thanks to their positive charge able to passivate defects with negative charge. In addition, a better charge transport and grain size were reported thanks to H bonds formation with halogen atoms in case of imidazolium. This effect also reduces iodine ions migration, important problem in perovskite solar cells. With a controlled amount of imidazole inside methyl-ammonium lead halide perovskite and enhancement of stability was obtained by Tomulescu et al.[108] with $MA_{0.94}IM_{0.06}PbI_{2.6}Cl_{0.4}$ perovskite. Moreover Salado et al.[109] demonstrated higher time for relaxation of photoluminescent adding 5% of imidazolium, with improved and more stable PCE (from 18.6% to 20%), thanks to effect on vacancies and grain boundaries. [109]
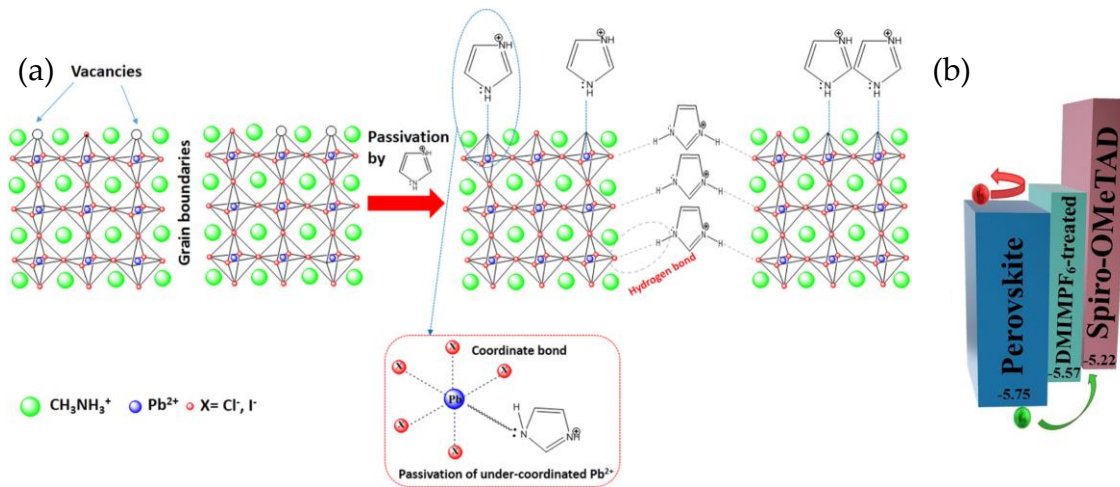
Figure 2.59. (a) Mechanism for passivation of $MA_{1-x}IM_xPbI_{2.6}Cl_{0.4}$ defects by IM doping (b) Energy band diagram of the perovskite device passivated with $DMIMPF_6$[110][108]

Imidazolium salts has been used as passivator of 3D lead iodide perovskite, thanks to their nature of ionic liquid that can passivate (with their counterions) perovskite surface defects. This passivation keeps good conduction between layers, with good matching of energy levels, as shown in Figure 2.59a.[110]Alkylated imidazolium salt, such as butyl-methyl imidazolium tetrafluoroborate, propyl-methyl imidazolium bromide or dimethyl imidazolium hexafluorophosphate ($DMIMPF_6$), were used to passivate 3D perovskite surface to enhance stability and efficiency of solar cells.

On one hand passivation of surface defects reduces trap-assisted recombination. This effect combined with good conduction of imidazolium salts increases charge transport with charge transport layers. This result in an increase of power conversion efficiency for controlled amount of these salts. [111] On the other hand, hand these ionic liquids possess hydrophobic alkyl chains that protect from moisture degradation, as confirmed by stability of power conversion efficiency over longer time with these passivating salts, even at higher temperatures.[112]

In addition, these salts give higher values with respect to pristine perovskites of photoluminescence and photoluminescence time of relaxation. This phenomenon indicates suppression of charge recombination, as described for imidazolium iodide.[94]

Another solution for passivation was investigated with imidazolium cations with fluorinated chains. In the work of Xindong et al.[71], methyl-imidazolium with perfluoroalkyl substituent in position 3 was studied as salt with tetrafluoroborate (Figure 2.60). Different length for fluorinated part were investigated, obtaining a hydrophobic effect over perovskite surface. Then, for 1-methyl-3-(3',3',4',4',4' pentafluoro-butyl) (MFIM-2) imidazolium tetrafluoroborate, better results in terms of

crystal growth, lower PbI$_2$ impurities and performances of solar cells were obtained. The main effects of these cations are made from passivation of undercoordinated sites and hydrophobic stable phase that enhance device lifetime. As previous passivation cases, PL was enhanced in terms of PLQY and relaxation time.[71]
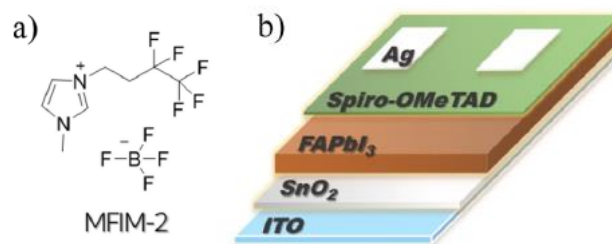
Figure 2.60. (a) Molecular structure of ionic liquids MFIM-2 (b) Schematic architecture of the device, elaborated from [71]

2.3.3 Imidazolium in low dimensional perovskites

Imidazolium (and its related salts) has been studied also as organic cation in low dimensional perovskite. Despite a computed value of Goldsmith factor of 1 (upper limit for this value) Among these cations, due to its large (258 pm) and propitious ionic radius.[113]

Imidazolium perovskites usually exhibited 1D structure, with face sharing lead halide octahedra surrounded by imidazolium cations. Some exceptions are given from imidazolium and ammino-propyl-imidazolium le ad bromides that create 2D perovskites, because of strong templating effect of double ammonium group with lead bromide sublattice. In addition, butyl-methyl-imidazolium lead bromide has a cluster 0D structure templated by hydrogen bonds among butyl chains. [71]

As reported by Seth et al. [96], Imidazole reaction with PbI$_2$ creates a 1D perovskite (C$_3$N$_2$H$_5$) PbI$_3$ by obtaining yellow crystals. This compound is characterized by 1D lead iodides chains surrounded from imidazolium cations, as shown in Figure 2.61. These cations create H-bonding between H of their C1 and iodine of inorganic chains (shown as turquoise dashed line in the unit cell image in Figure 2.62).[96]
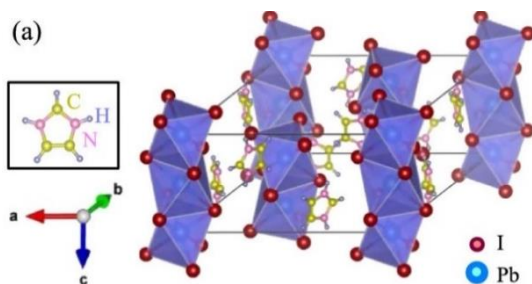
Figure 2.61. Imidazolium perovskite crystalline structure from Seth et al.[96]
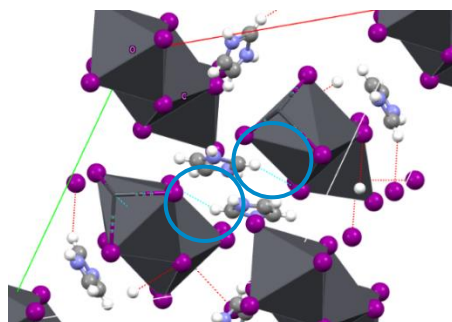
Figure 2.62. Computed hydrogen bond (circled in blue) imidazolium lead iodide unit cell, single crystal data from Weber et al. [71]

Inside this cell six imidazole ions are arranged hexagonally around the octahedral chain and the compound crystallizes in hexagonal space group $P6_3/m$. Imidazolium perovskite has distortion parameters in the order of other 1D compounds, as depicted in Table 2.1. These parameters, as described before can act on perovskite STE emissions, in this case distortion of inorganic sublattice is moderated. For example, this perovskite creates less distorted octahedra with respect to methylammonium lead iodide. [71]

Table 2.1. Distortion parameters for imidazolium lead iodides, computed from single crystal data of Weber et al. [71]

Distortion parameters	Imidazolium Lead iodide
Δd	$5.89*10^{-4}$ A
σ^2	21.29

Thermal stability was evaluated with TGA, DSC and XRD at various temperatures. Based on TGA data, imidazolium perovskite exhibits organic part-s peak of degradation at 425°C, while complete degradation of residual PbI_2 happens over 600°C. DSC shows phase transition at 94°C (Figure 2.63). From Powder XRD analysis

at temperature near transition, peaks related to crystallographic planes merges. This effect has been reported as proof of increase of lattice symmetry with a new phase.[114] Stability of this perovskite over time was proven by evaluation of stable intensity of selected peak of its lattice. This result, together with thermal properties, make this material interesting for its stable 1D structure.[114]
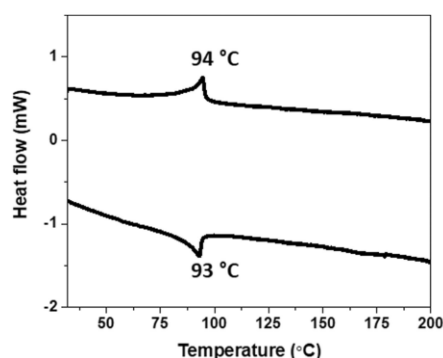
Figure 2.63. DSC measurements on Imidazolium lead iodide powders in the temperature range of 32°C to 200°C at the scan rate of 5°C/min[114]

Despite differences between imidazolium lead halides (lead bromide was reported as 2D perovskite), 1-alkyl-3-methyl-imidazolium perovskites has been reported as 1D structures with different halogen atoms (Cl and Br).[115,116] The most significant example is given from ethyl-methyl-imidazolium (C2ImMet) lead halides, with reported resolved single crystal structures for lead chloride and bromide and approximated one for lead iodide (the last one was resolved in this thesis). [115,116]

C2ImMet cations separates lead halide chains, creating hydrogen bond with them and among organic cations. In ethyl-methyl-imidazolium $PbCl_3$ and $PbBr_3$ hydrogen bonds between H atoms are related to C atoms. These bonds template distorted lead chloride structure as shown in Figure 2.64. These results allow to make comparison among different 1D lead halide's structure, considering halogen effect in terms of dimensionality and electronegativity.[115,116]
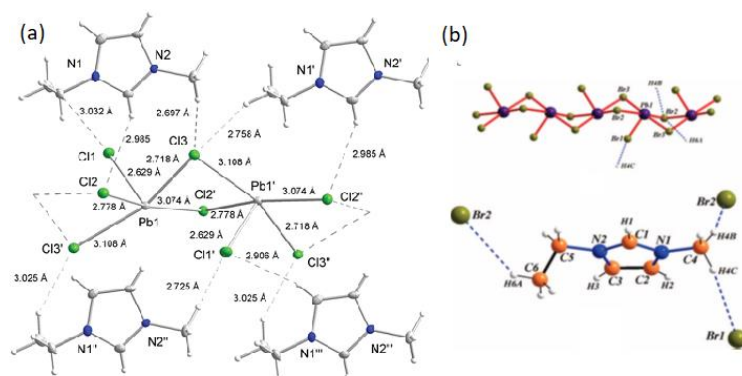
Figure 2.64. 1-ehtyl-3-methyl-imidazolium (a) lead chloride and (b) lead bromide.[115,116]

Lead was found in a pentacoordinate state with different length given by distortion, creating an orthorhombic unit cell with space group Pnma, for lead bromide. While $P_{2_12_12_1}$ space group was found for lead chloride. This difference is made by different strength and template of hydrogen bonds between inorganic sublattice and C_2ImMet cations.

Hydrogen bond templating effect was found effective also with longer chains as described from single crystal structure of lead bromide 1D perovskites with methyl substituted imidazolium salts with propyl, pentyl, and hexyl as substituent in position 3. These interactions are mediated by hydrogen bonding (circled and shown as turquoise dotted line in Figure 2.65a, and c) that can interest H related to primary carbon of alkyl substituent in position 3. These atoms are more prone to hydrogen bonding with halogen of inorganic chains thanks to electron delocalization induced by the nearest N atoms. Increasing alkyl chain length, hydrogen bond of CH_3 group in alkyl chain becomes less important, with interdigitation among alkyl chain more dominant. However, Butyl-methyl imidazolium lead bromide exhibits a 0D clustered structure (Figure 2.65b) thanks to hydrogen bonds among imidazolium cations.[115] So, even with alkyl-methyl imidazolium perovskites some unexpected changes in dimensionality can occur, 1D structures were reported. This effect results in different optoelectronic properties.[60-62]
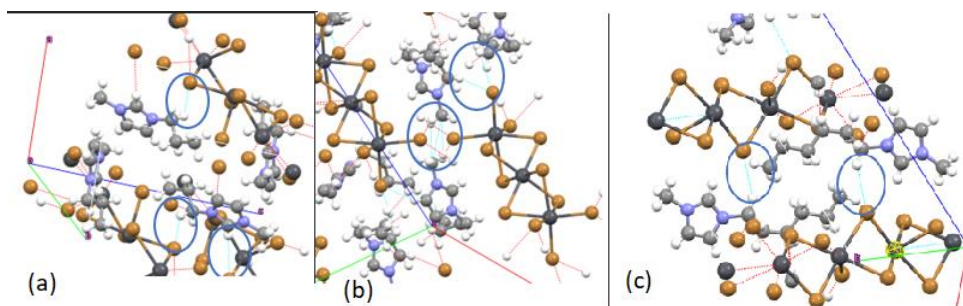
Figure 2.65. Single crystal structure of (a) Propyl-Methyl-Imidazolium, (b) Butyl-Methyl-Imidazolium and (c) Hexyl-Methyl-Imidazolium lead Bromide, single crystal data from [60-62]

Temperature affects crystalline structure with phase transitions that occur at low temperature because of arrangement of alkyl chains of imidazolium. These phase transitions affect dielectric permittivity at different frequencies evaluated at different temperatures. In fact, over a certain temperature, dielectric relaxation shifts dielectric peak to higher frequencies. This dielectric relaxation can be ascribed to phase transition over the previously mentioned temperature. Under this temperature dipole motion is suppressed leading to a dielectric permittivity with temperature. [60-62]

Distortion parameters of lead halides chains are affected by different packing and interaction of imidazolium cations as shown in Table 2.2. These parameters will affect Photoluminescence with similar STEs broadband wavelength.

Table 2.2. Lead bromide chains distortion parameters for imidazolium perovskite: absolute value and percentage variation with respect to undistorted lead bromide octahedra (*butMetIm is a 0D structure) [60-62]

	Bond lenght distortion(Δd) [A]$\rightarrow$%	**Angle distortion (σ^2)$\rightarrow$(σ/90°)**
EtMetIm-PbBr3	0.02[1] (0.015) $\rightarrow$0.0067 %	150.81[1] (28.97) $\rightarrow$13.6%
PropMetIm-PbBr3	1.56*10^{-7}$\rightarrow$0.52*10^{-7}%	21.16$\rightarrow$5.1%
ButMetIm-PbBr3*	1.56*10^{-7}$\rightarrow$0.52*10^{-7}%	21.10$\rightarrow$5.1%
HexMetIm-PbBr3	0.00705$\rightarrow$0.00235 %	74.46$\rightarrow$7.8%

2.3.3.1 *Optoelectronic properties*

Based on these observations in some cases electronic structure of imidazolium compounds have been calculated thanks to DFT theory, to explain absorption spectra these perovskites.

Imidazolium lead iodide exhibits 1D quantum confinement effect, this result was obtained by Seth et al. [96] using EMEW (effective mass envelope-wavefunction) theory. This theory comes from 2D perovskite and was fitted for 1D quantum confined structure problem, neglecting terms of interaction among inorganic chains via cations interaction. However, from experimental data, absorption edge was found at 2.92 eV ca. as shown in Figure 2.66, with a shoulder at lower energy given from absorption in π^* state of imidazolium cations.[96]
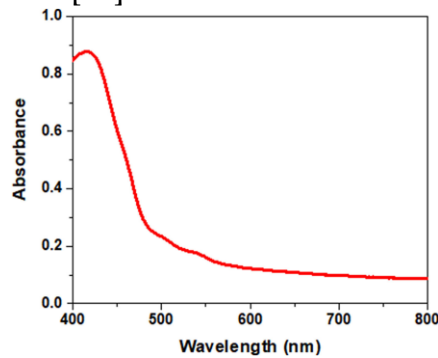
Figure 2.66. Absorption spectrum of ImPI crystal powder, recorded in the diffuse reflectance mode at room temperature[96]

So, this approximation is partially valid for imidazolium because it does not fully describe band structure and other phenomena, such as thermochromic effect, as we will see later. Starting from this calculation Band Gap was found as 3.3 eV, higher than PbI2 of 0.76 eV, with exciton energy around 200 meV. [96]
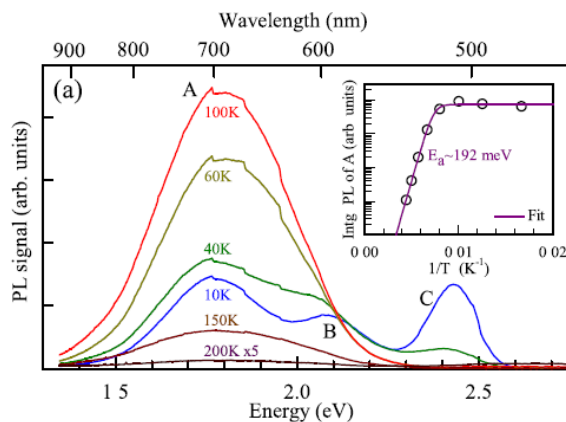
Figure 2.67. (a) Temperature dependence of the PL spectrum of ImPI (right) Arrhenius plot of the integrated PL throughput at high temperatures[96]

Self-trapped exciton was observed from PL measure at low temperature (100K and 10K), here effect of STEs, is highlighted with respect to free exciton. Photoluminescence spectrum (Figure 2.66 curve A) shows a broad peak at 1.8 eV (width 173 nm). This peak is strongly redshifted with respect to absorption edge because of STEs emission. Intensity of this broad peak increases from 200K to 100K (thanks to reduction of FE contribution) but decreases at temperatures lower than 100K (Figure 2.66 curve B). This effect is made from reduction of thermal energy that reduces probability to create a self-trapped state. Exciton decay equation with temperature was fitted with activation energy of 192 meV ((Figure 2.66 right). At 100K was reported a very small peak related to free exciton emission in thermal equilibrium with STE, this effect is enhanced with temperature. In addition, decreasing temperature results in an additional peak at energy higher than 2 eV, that can be ascribed to defect in this case, with a saturation of PL intensity increasing laser excitation. [96]

Time resolved photoluminescence of broad peak A shows two exponential decay functions. The main one is related to STEs and results in decay time $\tau = 13$ µs at 10 K, which decreases to 2.5 µs at 100 K. These values show PL efficiency from STE enhanced at low temperature. However, this 1D perovskite needs to be further investigate by modification of organic cations to enhance photoluminescence even at room temperature. [96]
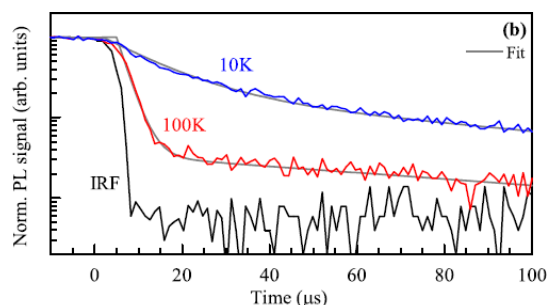
Figure 2.68. Temporal decay of PL (325 nm laser) throughput from ImPI at two different temperatures along with the instrument response function [96]

Imidazolium lead iodide perovskite solar cells performances were evaluated, with PCE of 1.1%, like methylammonium perovskite on same device (PCE=1.6%).[114]

Absorption spectra (Figure 2.69) of imidazolium salt lead bromide compounds shows a sharp band on absorption edge, made from transition from valence to conduction band (400-500nm). This band can present a shoulder made from transition involving directly π^* states of imidazolium cations. Then π-π^* transitions made from imidazolium cations give an intense and broad absorption band at lower wavelengths (200-300nm).[60,61]
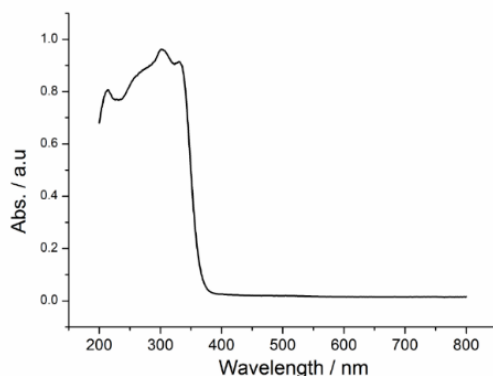
Figure 2.69. Solid state absorption spectra of propyl-methyl-imidazolium lead bromide at room T[60]

Absorption spectra for these perovskites give values of energy gap from 3.65 eV (propyl-methyl imidazolium) to 3.35 eV (hexyl-methyl imidazolium). So, thanks to different arrangement of chains, lead and bromide orbitals have a different superposition resulting in lower bandgap with longer chains.[60-62]

Photoluminescence spectra of these compounds is characterized at room T by a broad peak between 500 and 750 nm (Figure 2.70). This peak is caused by STE emission in thermal equilibrium with free exciton emission. Intensity of this peak are reduced with longer chains, resulting in a different emission.[61] Similar values for exciton emission wavelengths are given from similar distortion parameters of these perovskites. In addition, PLQY at room temperature of these perovskite remains at room T between 2-5% range. [60-62]
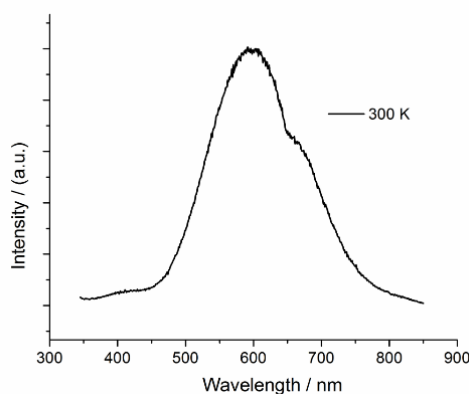
Figure 2.70. Solid state emission spectra of butyl-methyl-imidazolium lead bromide at room temperature[61]

These perovskite exhibit thermochromism induced by the onset of π^* states radiative transitions at low temperature. These transitions result in a secondary peak at

wavelengths lower than broadband peak (usually in 400-500 nm region, associated to imidazolium ring emission) (Figure 2.71b). This peak is present at low temperature (usually around 150-100 K) because it is a consequence of decoupling between vibrational modes of lead bromide sub-lattice and imidazolium excited states. Lowering temperature "freezes" non-radiative de-excitation path, enabling radiative recombination of pi* states to VB. At temperature lower than threshold values for second emission, as shown in Figure 2.71c, intensity of higher energy peak increases more than the broad peak. [60-62]
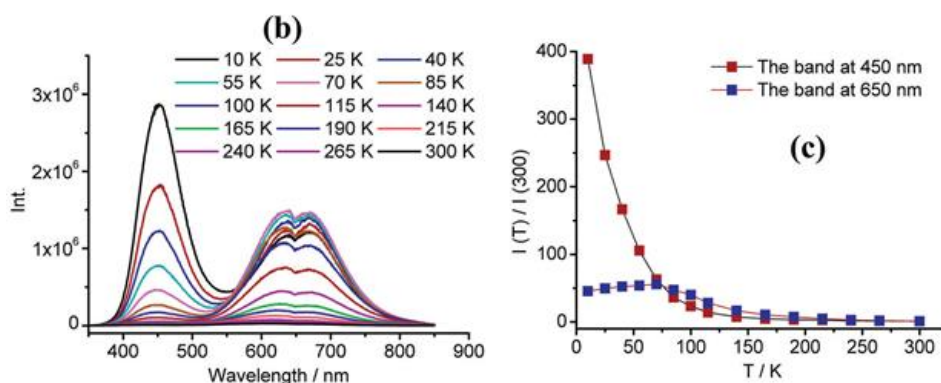
Figure 2.71. Hexyl-methyl imidazolium lead bromide (b) emission spectra, (c) temperature dependent relative emission intensity for two bands[62]

This effect is mediated from organic cations (functional group, electronic structure) and their interaction with inorganic sublattice. So, secondary emission wavelength and onset temperature are modified by alkyl chains and perovskite dimensionality. [60-62]

This thermochromic effect was evaluated by CIE diagram. CIE results show a non-monotonic change of color of these materials a different temperature, useful for temperature sensing application (Figure 2.72 c and d).[60,61]
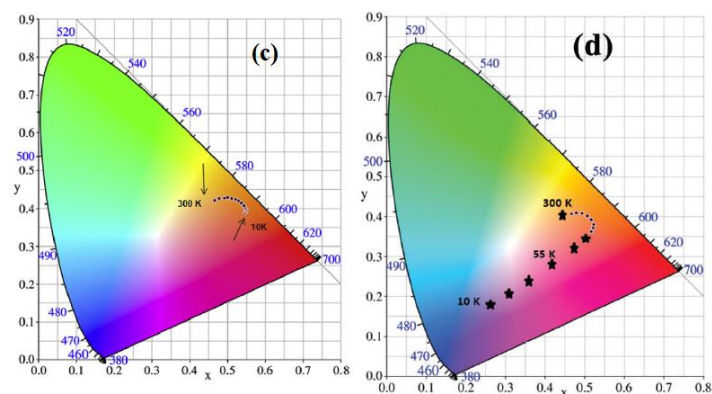
Figure 2.72. CIE chromaticity diagram showing the fluorescence color at selected temperatures of (c) propyl-methyl-imidazolium lead bromide and (d) hexyl-methyl imidazolium lead bromide.[60,61]

However, imidazolium perovskites literature lacks in a systematic study of correlation structure properties with different halogens or use of fluorinated cations. This thesis investigated these two aspects trying to understand better effect of functionalized imidazolium cations in lead iodide 1D structures.

3. Purpose of the experimental work

The purpose of this experimental work was the investigation of alkyl-methyl imidazolium cations inside perovskite structure and incorporation of perfluoroalkyl chains in low dimensional perovskite through these cations.

Perfluoroalkyl chains have been reported in literature as interesting functional groups thanks to their effect on electronic structure on conjugated cations. Lowered LUMO and HOMO of conjugated core made by from strong withdrawn of electrons by perfluoroalkyl chains.[88,107] This effect has not been investigated inside a perovskite structure. In addition, these functional groups take advantage of self-assembly effect induced by interaction of fluorinated phase, as described before.
Moreover, perfluoroalkyl chains are well known for their hydrophobic effect, described before, interesting for moisture protection of perovskite materials and so a possible enhancement of their stability.
Perfluoroalkyl-methyl imidazolium molecules were selected thanks to their previously analyzed properties of self-assembly, that causes liquid crystal behavior imidazolium iodide salts described before. In addition, these molecules can be compared to results in literature about alkyl-methyl imidazolium lead bromide and imidazolium lead iodide 1D perovskites.

Therefore, a study on alkyl-methyl imidazolium (with different alkyl chain lengths, as shown in Figure 3.1) in lead iodide perovskite was carried out to understand their structure and properties. These results were compared to (1,1,1,2,2,3,3-heptafluoro-pentil-methyl-imidazolium iodide (C_5F_7MetImI-) and 1,1,1,2,2,3,3,4,4,5,5,6,6-Tridecafluorononil-methyl-imidazolium iodide (C_9F_{13}MetImI-)(Figure 75(c)) to understand perfluoroalkyl chain effect. Investigation was made through synthesis of these compounds and thermal, optical and structural characterization. Moreover, hydrophobicity was evaluated through contact angle measures to assess this property for these perovskites.
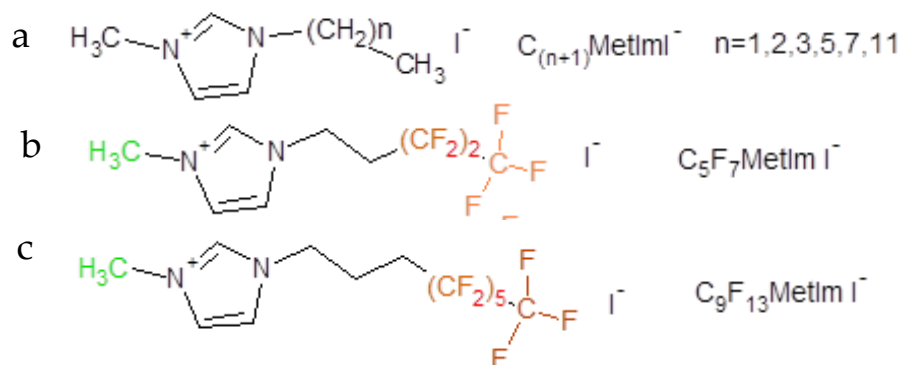
Figure 3.1. 1-Alkyl-3-methyl- imidazolium and perfluoroalkyl-methyl imidazolium iodide used in this work

Therefore, a systematic study about these cations can provide insight for low dimensional perovskites considering conjugated cations with perfluoroalkyl chains with respect to alkyl chains, aspect that have not been investigated yet.

4. Materials and methods
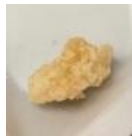
3.1 Synthesis and reagents

3.1.1 Imidazolium salts

All alkyl-methyl-Imidazolium salts were commercially available with exception of octyl-methylimidazolium iodide, as listed in Table 4.1

Table 4.1 Commercially available alkyl-methyl-imidazolium iodide salts used for this work

Name compound	Company	Chemical formula (MW[g/mol])	Characteristics	Phase at Troom	Photo
Imidazolium	Sigma Aldrich	$C_3H_4IN_2$ (68.08)	99% purity	Solid crystal	
1-Ethyl-3-methylimidazolium iodide (C₂MetImI-)	TCI	$C_6H_{11}IN_2$ (238.07)	98.0% purity	Solid crystal	
1-Methyl-3-propylimidazolium iodide (C₃MetImI-)	Sigma Aldrich	$C_7H_{13}IN_2$ (252.10)	98.0% purity	Ionic liquid	
1-Butyl-3-methylimidazolium iodide (C₄MetImI-)	Sigma Aldrich	$C_8H_{15}IN_2$ (266.12)	98.0% purity	Ionic liquid	
1-Hexyl-3-methylimidazolium iodide (C₆MetImI-)	Sigma Aldrich	$C_{10}H_{19}IN_2$ (294.18)	98.0% purity	Ionic liquid	

1-Dodecyl-3methylimidazolium iodide (C₁₂MetImI-)	Abcr	C₁₆H₃₁IN₂ (278.43)	98.0% purity	Solid crystal	

Octyl-methyl imidazolium iodide (C₈MetImI-) was obtained by nucleophilic addition of 1-iodooctane (from Sigma Aldrich with purity at 98%, MM=240.13 g/mol) to 1-methyl imidazolium (from Sigma Aldrich. MM=82.01 g/mol). 1-Iodo-octane (1.7 ml, 8.08 mmol, 1.29 eq.) in slight excess was dissolved in Toluene (13 mL) and then methyl-imidazolium (0.5 ml, 6.22 mmol, 1 eq.) was added. The solution was stirred for 24 hours at toluene reflux. Then, a brown viscous liquid was obtained at the bottom of the balloon. This phase was dried under vacuum, then the compound was characterized by ^{19}H in acetone-d. NMR analyses denote remained some residual methyl imidazole, with signals in 10-7 ppm region doubled as shown in Figure 4.1.
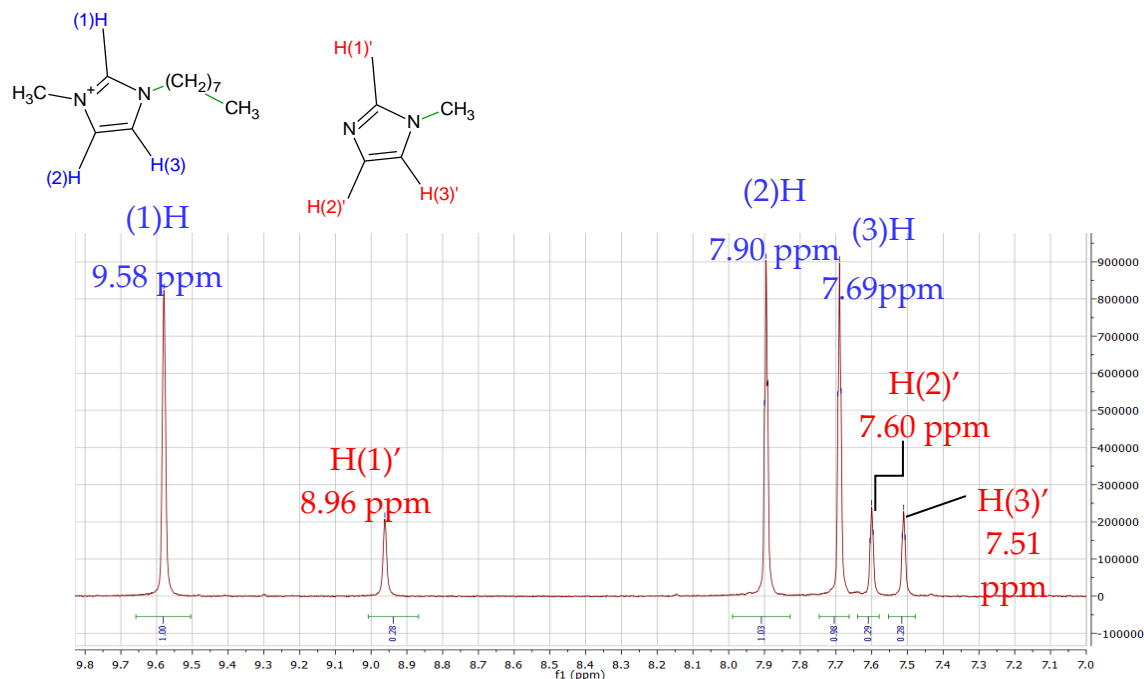
Figure 4.1. ^{1}H NMR signals in acetone-d6, with resolved peaks in 10-7 ppm region, blue for C₈ImMetI- and red for methyl imidazole

After this step, the obtained oil was washed with stirring at 50°C three times with hexane to remove traces of initial reagents. Then, this imidazolium salt was dissolved in chloroform and dried again to remove impurities inside the viscous liquid. Then, a viscous brown liquid (Figure 4.2, yield 65%) was obtained and characterized through FTIR and NMR.

Figure 4.2. 1-octyl-methyl-imdazolium iodide

As shown in Figure 4.3, imidazolium salts signals are expected in three regions:

1. Single H linked to carbon atoms of imidazolium ring: a first singlet is present at 9-10 ppm (signal of H(1)). Then two doublets are present in region between 8 and 7 ppm. All these signals are integrated equal to 1.
2. CH group linked directly with imidazolium ring: one peak (triplet, 2H) is located at 4.3 ppm due to CH_2 in position 1. Methyl group in position 3 creates singlet around 4 ppm (3H)
3. Other CH of alkyl group in position 1: these signals in alkylated chains contains a multiplet of CH_2 of secondary carbon (around 2, 2H) and multiplets related to alkyl chain at 1.9-1.8 ppm (10H). The last methyl group is present at 0.8 ppm, as multiplet with area=3. In case of fluorinated chains multiplets of alkyl part are still present as multiplets.
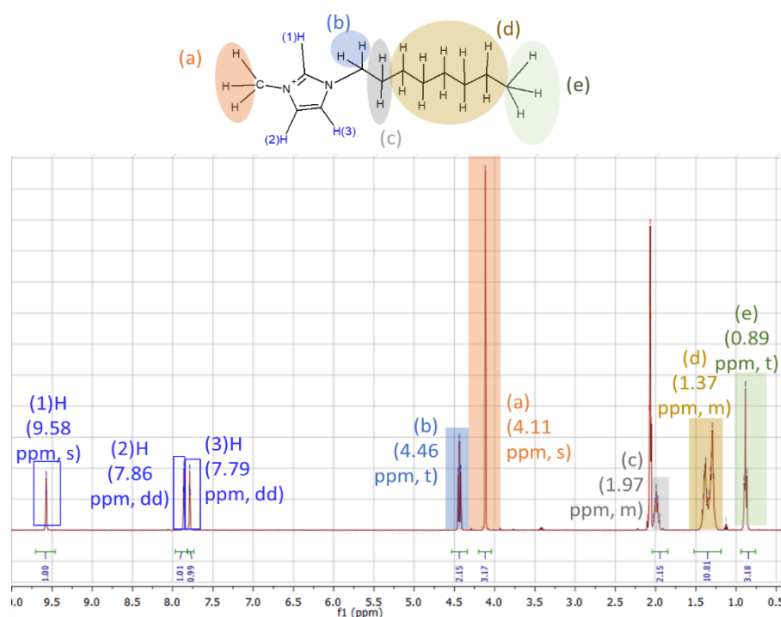
Figure 4.3. Resolved 1H NMR spectra for $C_8ImMetI-$

Perfluoro alkyl methyl imidazolium iodides were obtained with similar procedure (1-methyl imidazole in toluene at reflux for 24 hours), using 8-iodo-perfluoro-alkyl compound:

1. $C_5F_7MetImI-$: 1,1,1,2,2,3,3-heptafluoro-5-iodopentane from abcr(purity 96%, MM=323.98 g/mol)
2. $C_9F_{13}MetImI-$: 1,1,1,2,2,3,3,4,4,5,5,6,6-Tridecafluoro-9-iodo-nonane from Manchester Organic (purity 95%, MM=488.03 g/mol)

Reaction for $C_5F_7MetImI$-, $C_8F_{13}MetImI$-, $C_9F_{13}MetImI$- was carried out with the following step, with quantities listed in Table 4.2.

1. Step 1: slight excess of 2-iodo- was dissolved in toluene and then 1-methyl imidazole was added.

   Then reaction was left 24 hours under stirring and at 110°C.

2. Step 2: brown crystals or brown viscous liquid were obtained and dried at rotavapor. Then compounds were washed to remove excess of unreacted compounds

   $C_5F_7MetImI$- was washed at 80°C in toluene and then three times with hexane te remove excess of other compounds. After this step a brown viscous liquid was obtained (Figure 4.4).

   $C_9F_{13}MetImI$- was washed with ethyl-acetate and dried at rotavapor for three times. Then yellow-white crystals were obtained (Figure 4.5).

All compounds were characterized with NMR, mass spectrometry and FTIR with data reported in 4 section, coherent with previous work about these salts.[106,117]

Table 4.2. Reagents quantities for $C_5F_7MetImI$-, $C_8F_{13}MetImI$-abd $C_9F_{13}MetImI$-
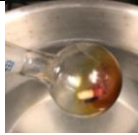
Name – molar mass	1-Methylimidazole - V (moles- eq.)	Toluene (volume)	1-iodo-perfluoro alkyl chain - mass (moles – eq.)	Photo
$C_5F_7MetImI$- (DR42) - 323.98 g/mol (yield=85%)	0.156 mL (1.93 mmol- 1 eq.)	5 mL	736 mg (2.137 mmol – 1.1 eq.)	Figure 4.4. $C_5F_7MetImI$-
$C_9F_{13}MetImI$- (GV3) - 488.03 g/mol (yield=90%)	.283 mL (3.51 mmol – 1 eq.)	3 mL	1.07 mL (3.861 mmol – 1.1 eq.)	Figure 4.5 $C_9F_{13}MetImI$-

Table 4.3. NMR peaks and mass spectroscopy of $C_5F_7MetImI-$ and $C_9F_{13}MetImI-$

Name – molar mass	¹H NMR peaks (CDCl₃)	¹⁹F NMR peaks (CDCl₃)
$C_5F_7MetImI-$ 323.98 g/mol	δ=10.2 (s, 1H), 7.48 (s, 1H), 7.3 (s, 1H), 4.83 (t, 2H), 4 (s, 3H), 2.93 (m, 2H) ppm	δ=-80.34 (t, 3F), -114.1 (m, 2F), -127. 37 (t, 2F) ppm
$C_9F_{13}MetImI-$ 488.03 g/mol	δ=10.18 (s, 1H), 7.37 (s, 1H), 7.36 (s, 1H), 4.53 (t, 2H), 4.04 (s, 3H), 2.3 (m, 2H) ppm (Data coherent with Cavallo et al.)[106]	δ=-80.81 (s, 3F), -113.56 (s, 2F), -121.82 (m, 2F), -122.81 (m, 2F), -123.12 (m, 2F), -126.1 (m, 2F) ppm (Data coherent with Cavallo et al.)[106]

19F NMR spectra show peaks of fluorinated chains, as demonstrated in Figure 4.6. This characterization was used to assess incorporation of perfluoroalkyl chains in position 3, visible from one signal for every group of fluorinated atoms, as shown in Figure 4.6.
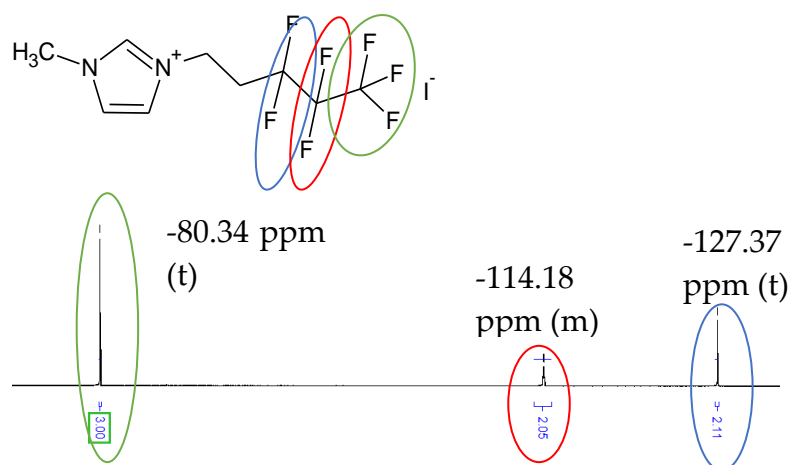
Figure 4.6. Resolved ¹⁹F NMR spectrum of $C_5F_7MetImI-$

3.1.2   Perovskites

Perovskite syntheses were carried out with the procedure described in Seth article, using imidazolium iodide and PbI_2 with molar ratio 2:1, this reaction happens in huge excess of HI.[114] Lead (II) iodide (PbI_2, 461.1 g/mol) was purchased from abcr, with purity 99.999% specific for perovskite synthesis. This material appears as yellow powder, as shown in Figure 4.7.

Figure 4.7. Lead (II) iodide
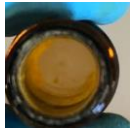
Hydroiodic acid (HI, 127,9 g/mol) was purchased from abcr, as 57% w/w solution stabilized with 1.5% Hypophosphorous acid.
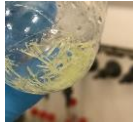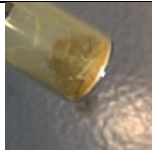
Imidazolium salt was added to PbI_2 previously dissolved with heating and agitation in a huge excess of HI (30 equivalents with respect to lead iodide).

Then reaction was kept at 110°C for 24 hours under stirring and nitrogen atmosphere. After this step some precipitate was obtained for short alkyl chain and it was filtered at Buckner, to obtain yellow needle-shaped crystals. These crystals were washed with ethanol and annealed at 90°C for 1 hour.

For longer chains (Cn, with n>3) an additional step with precipitation in fridge for 1 night were needed, after that precipitation was obtained with addition of ethanol. Then yellow powders are obtained, washing with ethanol. Samples were stored in fridge without direct exposure to light.

Table 4.4. Imidazolium perovskite reagents quantity and final product

Name(yield)	Imidazolium cation (mass/volume, moles)	Lead (II) iodide (mass, moles)	HI	Photo
DR31(81%)	Imidazole (200 mg, 2.94 mmol, 2 eq.)	677.2 mg, 1.46 mmol, 1 eq.	5.8 ml (30 eq.)	

DR23 (83%)	C$_2$MetImI- (361 mg, 0.950 mmol, 2 eq.)	218 mg, 0.475 mmol, 1 eq.	1.95 mL, 30 eq.	
DR38 (79%)	C$_3$MetImI- (0.38 mL, 3.38 mmol, 2 eq.)	525 mg, 1.19 mmol, 1 eq.	4.5 mL, 30 eq.	
DR40 (60%)	C$_4$MetImI- (0.43 mL, 3.37 mmol, 2 eq.)	549.4 mg, 1.685 mmol, 1 eq.	4.5 mL, 22 eq.	
DR26 (65%)	C$_6$MetImI- (361 mg, 0.950 mmol, 2 eq.)	218 mg, 0.475 mol, 1 eq.	1.95 mL, 30 eq.	
DR49 (61%)	C$_8$MetImI- (100 mg, 0.31 mmol, 2 eq.)	71.55 mg, 0.155 mmol, 1 eq.	1.4 mL, 30 eq.	
DR28 (63%)	C$_{12}$MetImI- (391.13 mg, 1.034 mmol, 2 eq.)	238.3 mg, 0.517 mmol, 1 eq.	4.1 mL, 30 eq.	
DR46 (65%)	C$_5$F$_7$MetImI- (118.8 mg, 0.214 mmol, 2 eq.)	49.25 mg, 0.107 mmol, 1 eq.	1 ml, 30 eq.	
DR34 (60%)	C$_9$F$_{13}$MetImI- (710 mg, 1.244 mmol, 2 eq.)	287 mg, 0.622 mmol, 1 eq.	1.23 ml, 30 eq.	

3.1.3 Deposition for contact angle measure

Perovskite films were obtained by dissolution of imidazolium perovskite in anhydrous N,N-dimethylformamide (Sigma Aldrich, purity 99.8%). Solution with different concentrations of 1M were made for different imidazolium perovskite. Concentration was tuned in function of deposition technique, because of higher solution dissipation with spin coating with respect to drop casting. Glass substrates were prepared to

deposition with washing with acetone and ozone treatment for 15 minutes to avoid presence of passivated groups over glass substrate.

Perovskite-DMF solutions were deposited onto glass substrate with two techniques:

1. Drop casting: solutions with concentration 1M were prepared and deposited onto glass samples (Figure 4.8). Then solvent was left to evaporate for 2 days. Contact angle values were measured after this step, as well as FTIR spectra to asses presence of DMF. Then samples were annealed in a furnace at 90°C for one hour. After this step contact angles and FTIR spectra were measured again.
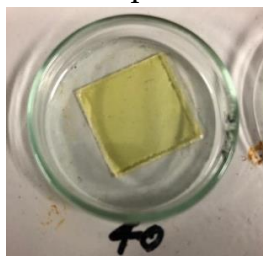
Figure 4.8. Deposited DMF-Perovskite solution onto glass sample for drop casting deposition

2. Spin coating was made with solution at 5M deposited onto glass samples. Deposition was made at 1500 rpm for 3 minutes. After this step contact angles were measured. Then samples were annealed in furnace at 90°C for one hour. After this step contact angles were measured again.

3.2 Materials characterization

3.2.1 Nuclear magnetic resonance (NMR)

1H and 13C NMR spectra in solution were recorded at ambient temperature on Nuclear Magnetic Resonance Spectrometer AVANCE III, Bruker-BioSpin (400 MHz). All the chemical shifts are given in ppm and the coupling constants in Hz. CDCl3 was used as both solvent and internal standard (as residual CHCl$_3$) in 1H NMR spectra and in ^{19}F

3.2.2 Fourier transformed Infrared spectroscopy (FTIR)

Varian 640-IR was used to perform FT-IR measurements. Transmittance scanning type selected with laser wavelength of 632.8 nm. PIKE Technologies MIRacle accessory allowed for attenuated total reflectance (ATR) mode analysis. The samples were placed onto ZnSe crystal plate and pressed hard against it by flat pressure tip. Dry nitrogen was used as purge gas. Varian Resolution Pro Software was used to elaborate data. Imidazolium salts and perovskite spectra were collected with 64 scans in 400-4000 cm-1 wavenumber range. Coating spectra were collected with 512 scans in 400-4000 cm-1 wavenumber range.

3.2.3 Thermogravimetric analysis (TGA)

TGA was employed to study degradation temperature of samples and to verify their stoichiometry. TA Instruments Q500 and TA Instruments Software were used to perform TGA and to elaborate data. Aluminum standard pans (75 ◎L) were used for samples insertion in the furnace. TA Universal analysis was used for data elaboration.

3.2.4 Differential scanning microscopy (DSC)

DSC analyses were performed by Mettler Toledo DSC823e instrument at a scan rate of 10K/min in sealed aluminum standard crucibles (40 ◎L) under air. An electrical resistance and nitrogen cooling system controlled the temperature. The furnace temperature was in the maximum range of -225K and 573K for these samples. STARe Software (Version 12.10) was used for data elaboration.

3.2.5   X-ray diffraction (XRD)

The single crystal data of the compounds were collected at 293 K using a Bruker SMART APEX II CCD area detector diffractometer. Data collection, unit cell refinement and data reduction were performed using Bruker SAINT.

Powder X-Ray diffraction data of compounds were collected on Bruker AXS D8 powder diffractometer with experimental parameters as follows: Cu-Kα radiation (λ = 1.54056 Å), scanning interval 4-40° at 2θ, step size 0.016°, exposure time 1.5 s per step.

3.2.6   Polarized optical microscope (POM)

The crystals textures during phase transitions were studied with an Olympus BX51 polarized optical microscope equipped with a Linkam Scientific LTS 350 heating stage and a Sony CCD-IRIS/RGB video camera. Samples were measured from room T to 250°C with heating and cooling rate of 5°C/min.

3.2.7   Contact angle measure

The contact angles of all of coated glass were determined using an OCA 15 PLUS instrument (Dataphysics) using droplet volumes of 4 µL for Milli-Q water. Advancing and receding contact angles were measured through the tilting plate method. The average contact angles (Elliptic method) were calculated from a series of five independent measurements by the SCA20 software.

3.2.8   Photophysical characterization

The absorption spectra were recorded using a Varian Cary 50 spectrophotometer.
The photoluminescence measurements were performed using a pulsed diode laser at 355 nm (Edinburg Inst. EPL 405, 40 ps pulse width) as excitation source and collecting the emitted light with a charged coupled device coupled to a spectrometer. Time-resolved photoluminescence experiments were conducted using the excitation source and collecting with a time-correlated single photon counting unit coupled to a monochromator and a photomultiplier tube. All PL measurements were performed with power density of 100 nJ/cm^2. Measurements were carried out at room temperature for all samples and in the temperature range 20K-300K for $C_3ImMet(PbI_3)$.

5. Results and discussion

5.1 Fourier transformed Infrared spectroscopy (FTIR)

Fourier transform infrared spectra was evaluated to analyze how vibrational modes of imidazolium are modified by the interaction inside perovskite lattice. So, interactions of these cations inside perovskite structure can be assessed.

First, it's needed to define which signals are typical of imidazolium salts used in this work. So, it can be understood which wavenumbers can provide a specific signal to recognize imidazolium cations and how they interact with lead halides octahedra.
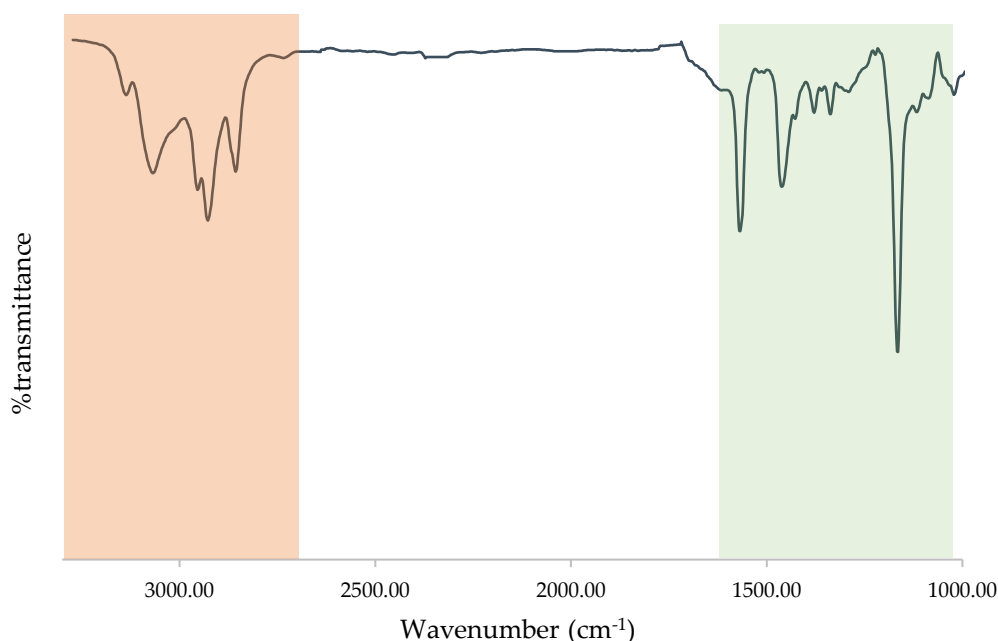
Figure 5.1. 1-Methyl-3-Hexyl imidazolium iodide FTIR spectra with CH stretching region (in orange) and other signals related to imidazole ring (in green)

As shown in Figure 5.1, alkyl-methyl-imidazolium iodide salts IR main signals can be analyzed in two regions:

1. **From 1000 cm^{-1} to 1800 cm^{-1}**, where significant peaks related to imidazolium ring are present, as shown in Figure 5.2.[62,118]

   Here, signals of C=C stretching and C-N stretching (between 1550 and 1600 cm^{-1} Figure 5.2 point c) are affected by ionic interaction among methyl-alkyl imidazolium cation and inorganic sublattice. Jerman et al.[119] reported single peak for imidazolium iodide salts, while changing ionic interaction with anions counterpart will result in a secondary peak in this region made from C-N ring stretchings de-coupled among them and so visible with respect to C=C one.[119] Other lower signals such as CH$_3$ scissoring (1400-1500 cm^{-1}), H-C(4)-C(5)-H scissoring (1000-1100 cm^{-1}) are present but are not useful to analyze imidazolium incorporation. FTIR spectrum shows peaks of alkyl chain rocking (1400-1300 cm^{-1}), twist (1100-1000 cm^{-1}), as enlightened in Figure 5.2 region (d). [118]

   In this region, a strong peak (Figure 5.2, peak (a)) between 1100-1200 cm^{-1} is present due to N(1)-C(2)-H rocking.[118] This peak's wavenumber remains a visible feature at lower wavenumbers to assess cations incorporation.
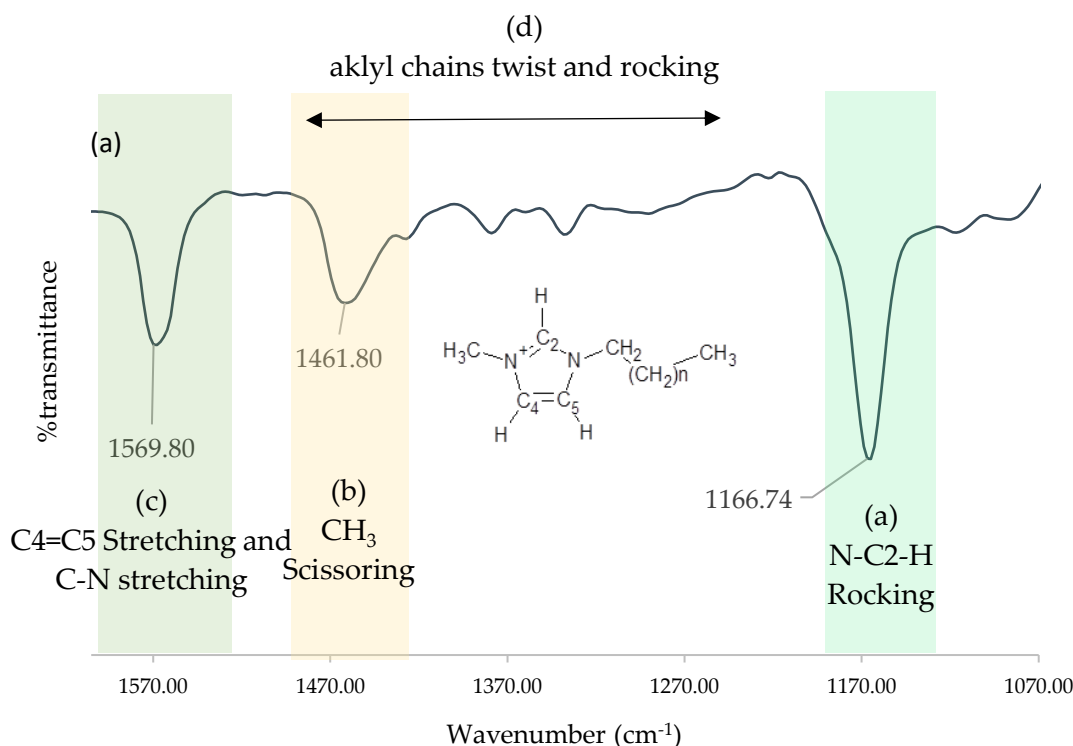
Figure 5.2. 1000-1800 cm-1 region FTIR spectra on 1-propyl-3-methyl-imidazolium iodide, with peak assigned to imidazolium signals

2. **At wavenumbers higher than 2800 cm^{-1}**, signals are caused from CH stretching modes of imidazolium ring and alkyl chains (Figure 5.3). [118,120]

CH vibration of aromatic ring creates peaks at 3200-3000 cm^{-1} (H-C(4)-C(4)-H stretching modes, peak (c) in Figure 5.3) and at 2900-2800 cm^{-1} (C(2)-H stretching peak (a) in Figure 5.3). These signals can be modified with change of anions with respect to I$^-$.[119]

Alkyl chain effect results from symmetric or asymmetric stretching between 2900-3200 cm^{-1}, as shown in Figure 5.3 by band (d). These signals, which change with different alkyl chains, can be used to asses cation incorporation. In addition CH$_3$ linked to C(3) creates a signal between 3100 and 2900 cm^{-1} (peak (b) in Figure 5.3) and prone to modification with perovskite incorporation. [119]
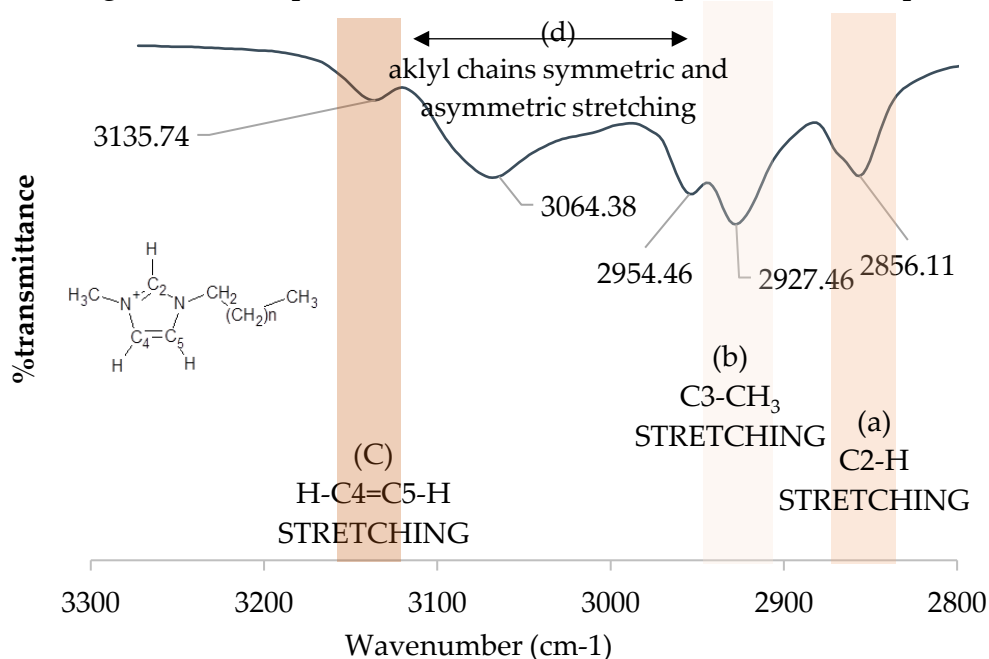
Figure 5.3. 2800-3300 cm-1 region FTIR spectra on 1-hexyl-3-methyl-imidazolium iodide, with peak assigned to imidazolium signals

Methyl-imidazolium iodide with fluorinated chains in position one shows same signals related to imidazolium ring (with different wavenumbers induced by different cations structure) with additional signals. In 2800-3300 cm^{-1} region (green band in Figure 5.4), signals are related to CH stretching in imidazolium ring and CH$_3$ in position 3. Moreover, alkyl spacers with fluorinated part linked to position 1 creates signals in this region. Then, at lower wavenumbers, imidazolium ring stretching is affected by lower interaction with anionic species, creating a shoulder in the signal of C=C stretching at 1500-1600 cm^{-1} (grey band in Figure 5.4). Moreover, CF stretching signals creates very strong bands dependent in terms of peaks and wavenumber on

fluorine atoms (orange band in Figure 5.4). Usually, CF_2 and CF_3 stretching signal creates strong bands in the region between 1400-1000 cm^{-1}. These signals are dependent on fluorinated carbon in imidazolium, and they overlap other signals.[121,122] They are made by CF_2 chains deformation and vibration and CF_3 rocking and wagging (in 600-800 cm-1 region in yellow band of Figure 5.4). [121,122] Obtained results are summarized in Table 5.1, with signal of $C_8F_{13}ImMetI^-$. They are coherent with previous literature reports of these crystals.[123]

1-Methyl-3-tridecafuorononylimidazolium iodide
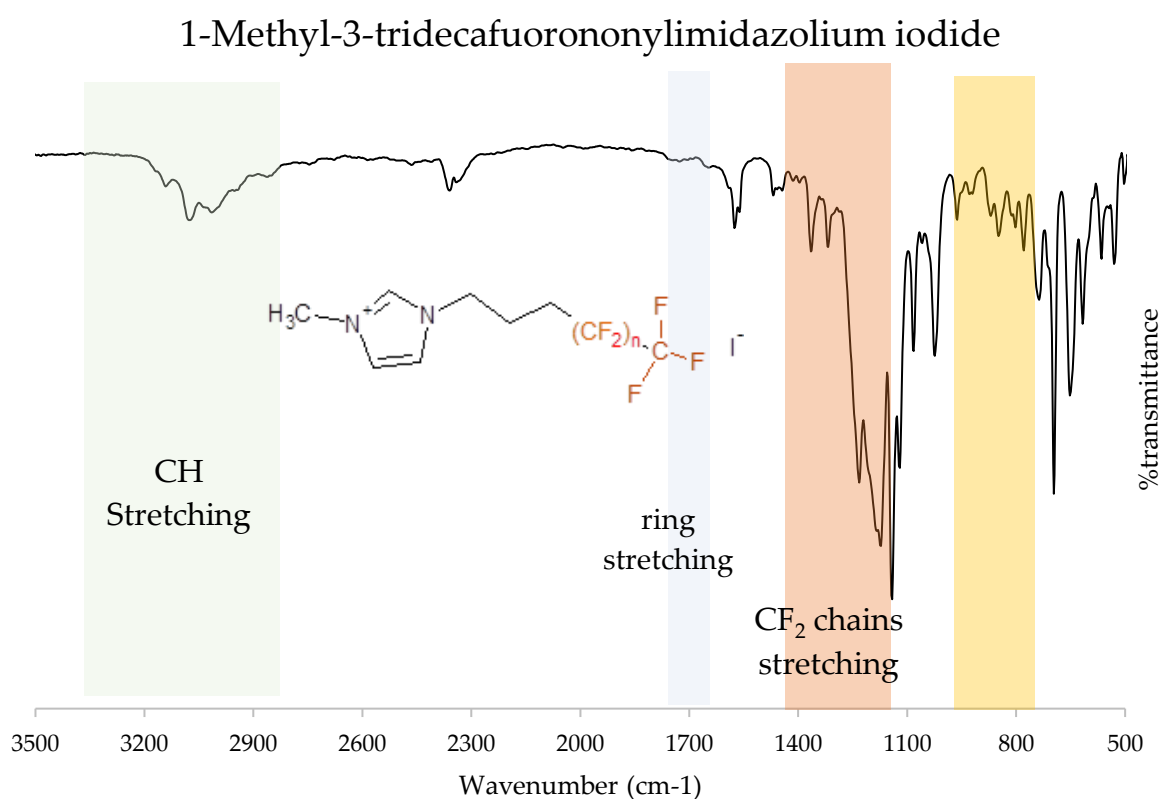
Figure 5.4. 1-Methyl-3-tridecafuorononylimidazolium iodide (GV3) FTIR spectrum with main bands

Table 5.1. Fluorinated imidazolium signals related to functional groups
(str=stretching, def=deformation, rock=rocking)

	HCCH str	CH3 str	C2H str	CH Chains str
$C_5F_7ImMetI^-$	3145	2962	2855	3066-3025
$C_9F_{13}ImMetI-$	3137	2931	2870	2957-3072

	C=C str	NCH rock	CF2 str	CF2 def
$C_5F_7ImMetI^-$	1576	1115	1219, 1172	750, 700
$C_9F_{13}ImMetI-$	1569 - 1581	1118	1236,1184	695, 749

FTIR spectra of imidazolium lead iodide 1D perovskite exhibited the same differences with respect to initial salts, with signals modified in different regions. Assessment of imidazolium inside perovskite can be carried out thanks to:

1. **Change of imidazolium C=C stretching** in 1500-1600 cm^{-1} region, where a double peak is created from interaction with lead iodide chains with imidazolium cations. These two peaks are related to a decoupling of C-N stretching from C=C peaks as effect of different charge distribution induced by lead halide chains (Figure 5.5 (a)).[119] In addition, the lower peak is at lower wavenumbers with respect to initial imidazolium peak, as an effect of different anion systems. So, imidazolium ring stretching was reported for all alkyl imidazolium species, as shown in Table 5.2. In perovskites' spectrum is still visible NCH rocking signal, shifted to lower wavenumbers (Figure 5.5 (b) and
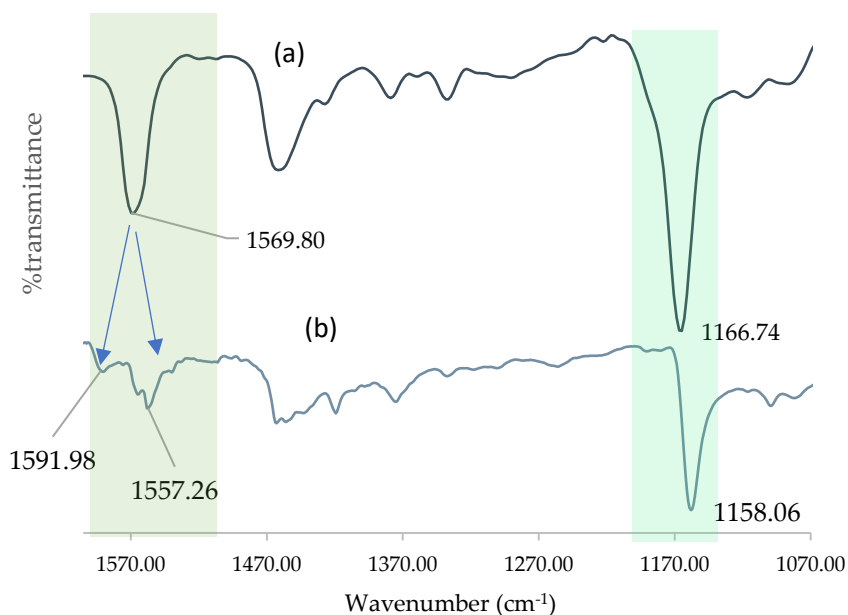
Figure 5.5. FTIR spectra of (a)C$_3$ImMetI- and (b)C$_3$ImMet (PbI$_3$)$^-$ in typical imidazolium ring signals region

Table 5.2. Imidazolium C4=C5 stretching and NC2-H rocking signals for different alkyl-methyl imidazolium iodide salts and their lead iodide perovskites

	Imidazolium iodide salt		Lead iodide perovskite	
	C=C str	NCH rock	C=C str	NCH rock
C₂ImMet	1570	1168	1560, 1583	1161
C₃ImMet	1569	1168	1558, 1591	1161
C₄ImMet	1567	1166	1560, 1582	1161
C₆ImMet	1568	1166	1562, 1573	1158
C₈Met m	1567	1164	1559, 1580	1160
C₁₂ImMet	1564	1164	1558, 1576	1161

These effects are also present in the case of fluorinated imidazolium, with additional peaks in imidazolium stretching region, as described in Table 5.3. However, NCH rocking is not clearly visible due to CF stretching signals, as shown in Figure 5.6.

CF stretching signals are similar for liquid crystal fluorinated chains, induced by similar perfluoro alkyl interactions.

Table 5.3. Imidazolium C4=C5 stretching and NC2-H rocking signals for different alkyl-methyl imidazolium iodide salts and their lead iodide perovskites

	Imidazolium salt				Perovskite			
	C=C str	NCH rock	CF2 str	CF2 def	C=C str	NCH rock	CF2 str	CF2 def
C₅F₇ImMetI⁻	1576	1115	1219, 1172	750, 700	1559, 1570	1111	1162,1220	707,756
C₉F₁₃ImMetI-	1581	1118	1236,1184	695, 749	1558, 1571	1122	1232,1189	697, 736
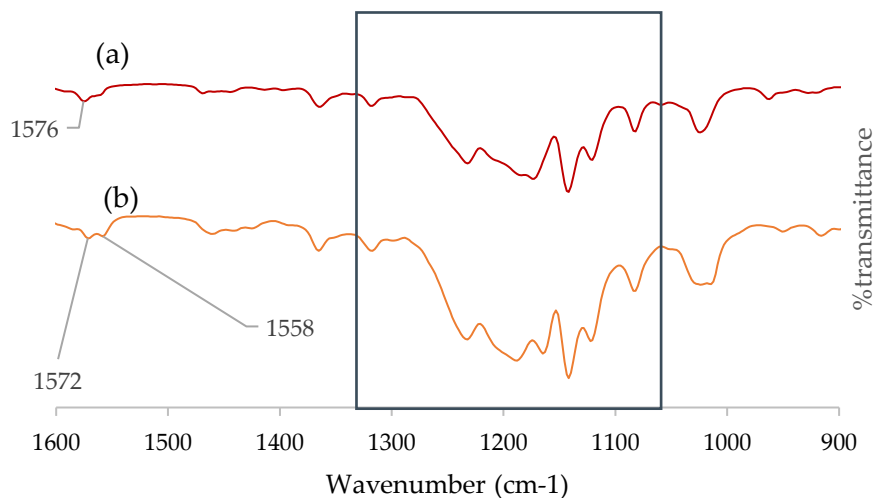
Figure 5.6. (a) $C_9F_{13}ImMetI^-$ and (b) $C_9F_{13}ImMet(PbI_3)^-$ FTIR spectra with comparison among imidazolium ring stretching signals and CF stretching (in square)

FTIR spectra of imidazolium lead iodide 1D perovskite exhibited same differences with respect to initial salts, with signals modified in different regions. Assessment of imidazolium inside perovskite can be assessed thanks to:

1. **Change of signals in 2800-3200 cm^{-1} region related to CH stretching band**: These changes are induced by ionic interaction. In perovskite, CH vibrations can be modified by surrounding interaction with halogen atoms.[124,125] These changes made by different interactions are reflected in the modification of stretching region, with shift of CH$_3$ and C2(H) stretching at lower wavenumbers,as shown in Figure 5.7.
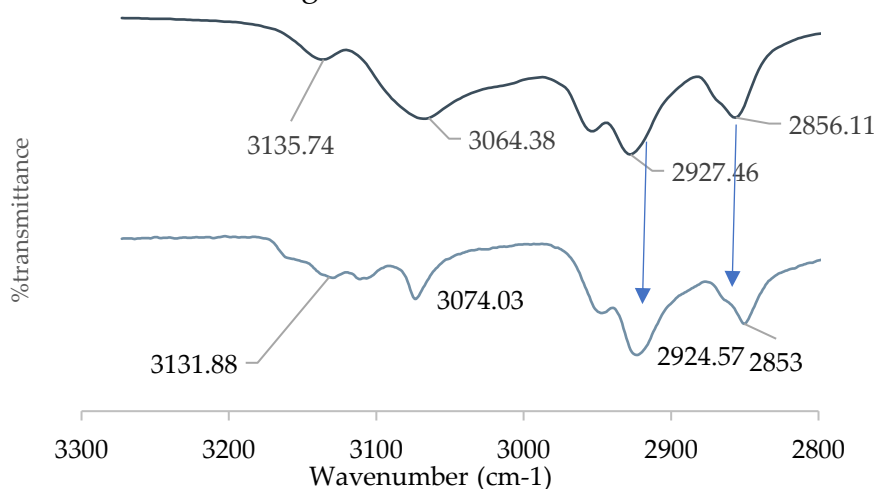
Figure 5.7. FTIR spectra of C$_3$ImMetI- and C$_3$ImMet (PbI$_3$)- in CH stretching region

This effect, together with modification of other CH stretching signals, gives a clue for incorporation of different alkyl-imidazolium, as shown in Table 5.4.

So, thanks to FTIR analysis, a first assessment of imidazolium presence inside the material was made. Further characterization has been used to confirm this hypothesis and further investigate material composition, structure, and properties

Table 5.4. Imidazolium ring stretching in CH stretching region for alkyl and fluoroalkyl imidazolium and their perovskite counterparts

	Imidazolium salts				Perovskites			
	HCCH str	CH_3	C2H	Alkyl Chains	HC CH str	CH_3	C2H	Alkyl Chains
C2Met	3134	2960	2871	3051-3080	3137	2928	2870	2960-3079
C3Met	3140	2945	2875	3077-2964	3134	2929	2871	2960-3079
C4Met	3137	2931	2870	2957-3072	3131	2930	2865	2953-3081
C6Met	3136	2927	2856	2972-3065	3131	2924	2853	2955-3043
C8Met	3141	2925	2854	2952-3074	3136	2921	2852	3084-3135
C12Met	3131	2919	2850	3026-3027	3139	2917	2848	3063-2974
C_5F_7Im Met	3145	2962	2855	3066-3025	3131	2953	2846	3107-3072
$C_9F_{13}Im$ Met	3137	2931	2870	2957-3072	3137	2948	2825	3083-3107

5.2   X-ray diffraction (XRD)

Crystalline structure of perovskite has been investigated with powder X-ray diffraction (PXRD) and single crystals XRD analysis, through the crystallographic software Mercury.[126]

PXRD have been used to assess perovskite formation in terms of a new crystalline structure. Peaks must be different for perovskite with respect to initial lead halide and imidazolium salts, otherwise the analyzed compounds can contain impurities or unreacted reagents. In Perovskite materials, signals are mainly related to lead and halogen atoms, thanks higher electronic density than organic molecules.[127]

In this experimental work, PXRD spectrum of alkyl-methyl imidazolium lead iodide was compared to the diffractograms of initial regents: Lead (II) Iodide and imidazolium iodide salts (possible only with salts solid at room T: C_2ImMetI- and C_{12}ImMetI-). As shown in Figure 5.8 for C_2ImMet lead iodide, different peaks with respect to reagents described an effective synthesis without remained imidazolium or lead iodide impurities. Comparison among peaks in alkyl-methyl perovskites were carried out for all perovskites, showing an effective synthesis.
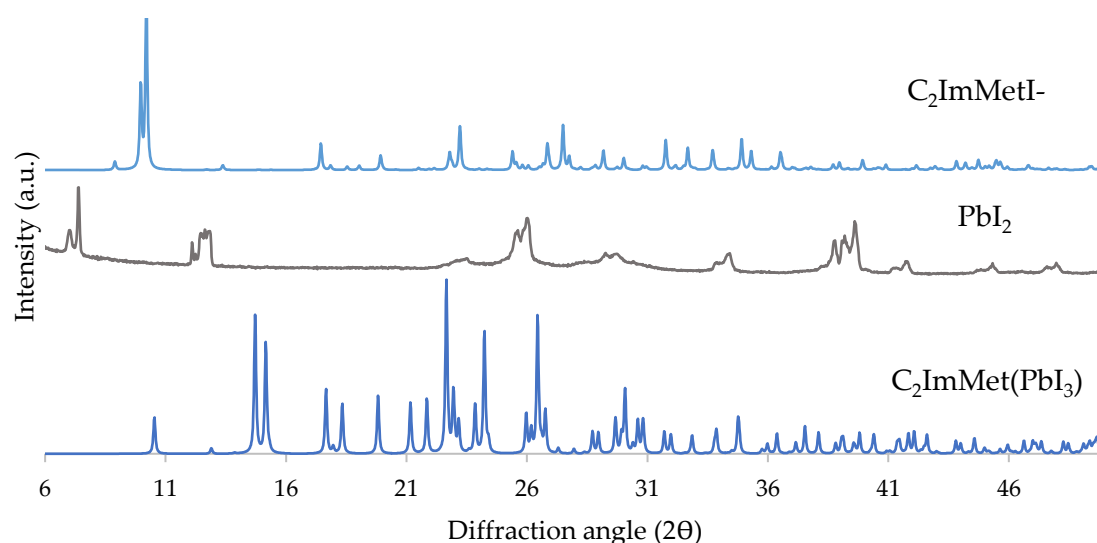
Figure 5.8. Powder XRD comparison among C2ImMetI-, Lead (II) Iodide and (C$_2$ImMet)PbI$_3$

First, C_2ImMet and C_3ImMet lead iodide perovskite needle-shaped crystals were analyzed through XRD of single crystal. Lattice structure was resolved for both this compounds, with a 1D perovskite structure made by lead iodide chains surrounded by organic cations. This structure was coherent with Imidazolium lead iodide,

C2ImMet(PbBr3) and C3ImMet(PbBr3).[60-62,115] C2ImMet lead iodide structure was resolved for the first time in this study. This material has a 1D perovskite structure, with lead iodide chains (parallel to b axis) surrounded by C2ImMet cations, as shown in Figure 5.9. Crystalline structure is arranged in Pbca space group, with a orthorhombic unit cell with the following parameters: **a** 17.734 **b** 8.188 **c** 19.862. Further details about crystallographic structure are present in Table A.1.
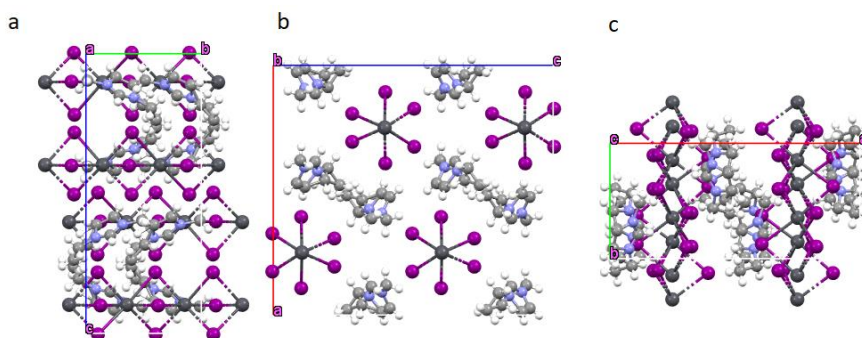
Figure 5.9. C2ImMet lead iodide crystal structure, with view along a, b, c axes

C3ImMet lead iodide shows a 1D perovskite structure like C2ImMet, as described in Figure 5.10. Its structure was resolved in P2(1)/n space group within a monoclinic cell, with a=8.138, b=17.9057 and c=21.422, with increase of cell dimensions in respect to C2ImMet. Further details about crystallographic structure are present in Table A.2
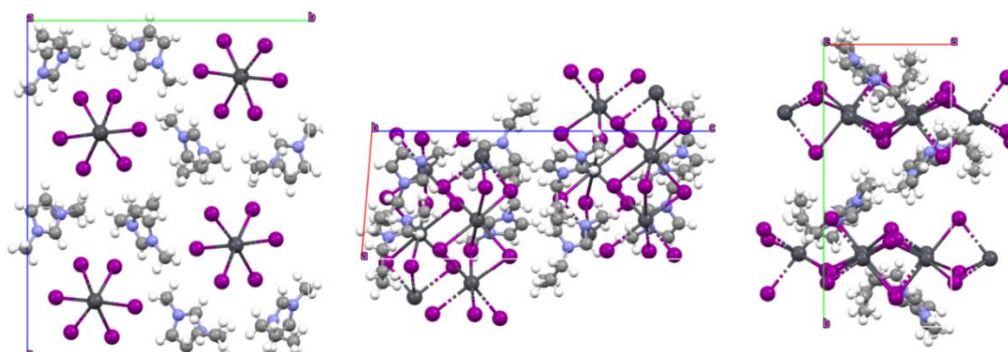
Figure 5.10. C3ImMet lead iodide crystal structure, with view along a, b, c axes

These structures have different packing induced by supramolecular interaction and steric hindrance, even though they maintain 1D structure like reported imidazolium lead iodide by Seth et al.[114] (C3ImMet)PbI3 exhibits hydrogen bonds among lead iodide chains and imidazolium cations that shapes lead halide distortion (Figure 5.11b). While (C2ImMet)PbI3 shows hydrogen bond among imidazolium cations (Figure 5.11c). (C3ImMet)PbI3 shows similar single crystal structure with respect to C3ImMet lead bromide reported by Shi et al.[60]. The main difference is made from

different hydrogen bonds with inorganic chains with respect to lead bromide counterpart (Figure 5.11c). As expected, H-bond are weaker for C3ImMet, due to lower electronegativity of iodine. [60]

d=3.180 A

d1=3.161 A
d2=3.131A

d1=2.988 A
d2=2.871 A
d3=3.023 A
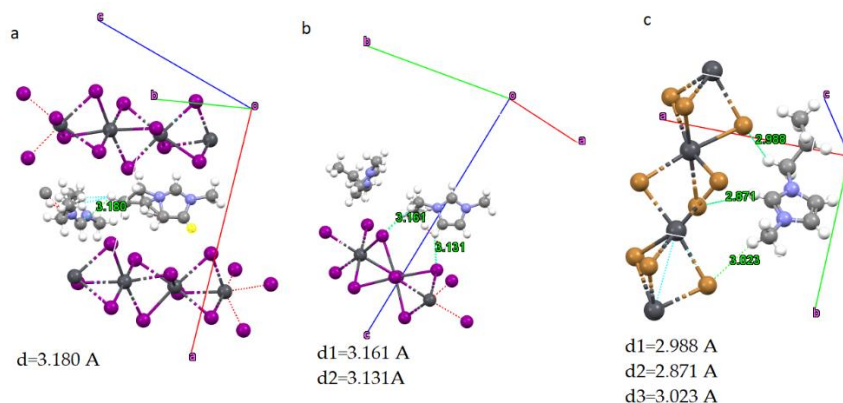
Figure 5.11. Hydrogen bonds (d) in (a) C2ImMet lead iodide, (b) C3ImMet lead iodide and (c) C3ImMet lead bromide[60]

Before discussion of PXRD and single crystals, literature data have been investigated to understand relation among PXRD and single crystal data in imidazolium 1D perovskite. XRD single crystal of 1-ethyl-3-methyl-imidazolium chloride and 1-alkyl-3-methyl-imidazolium bromide show that these perovskites possess a 1D face-sharing structure (Figure 5.12a and b).[115,116] In C2ImMet lead iodide (Figure 5.15c) compared to other lead halide, C2ImMet produces lower distortion with respect to other metal halides, as described in Table 5.5. This effect is made from stronger H-bond for chloride and bromide (computed from single crystal file with crystallographic software Mercury)[126] thanks to electronegativity which shapes lead halide sublattice, increasing bonds and angle distortion.[115,116]
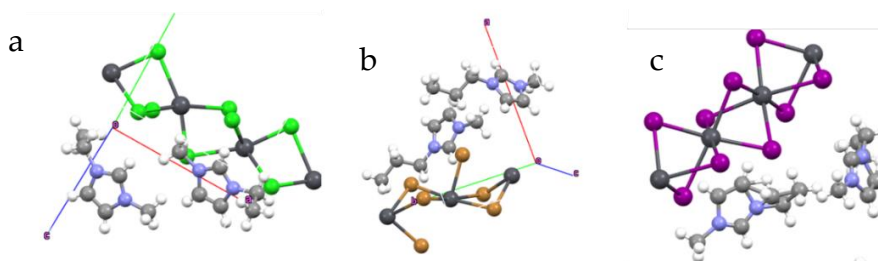
Figure 5.12. Ethyl-methyl imidazolium (a) lead chloride, (b) lead bromide and (c) lead iodide[115,116]

Table 5.5.Lattice distortion parameters (Δd and σ^2) and lead halide chain distance in C$_2$ImMet lead iodide, chloride and bromide from.[115,116] (1) value in brackets are computed using pentacoordinate Pb

	Bond length dist. $(\Delta d) \rightarrow \%$	Angle distortion $(\sigma^2) \rightarrow (\sigma/90°)$
C$_2$ImMet -PbI$_3$ (from this work)	$1.1*10^{-4}\%$	$48.41 \rightarrow 0.006\%$
C$_2$ImMet -PbBr$_3$[115]	0.007%	$150.81^{(1)}$ (28.97) $\rightarrow 13.6\%$
C$_2$ImMet -PbCl$_3$[116]	0.012%	$217.87^{(1)}$ (87.62) $\rightarrow 16.4\%$

Based on this observation, PXRD spectra simulated from lead bromide and lead chloride single crystals were compared to C$_2$ImMet. These spectra show strong peaks in 5-15° region (Figure 5.13).
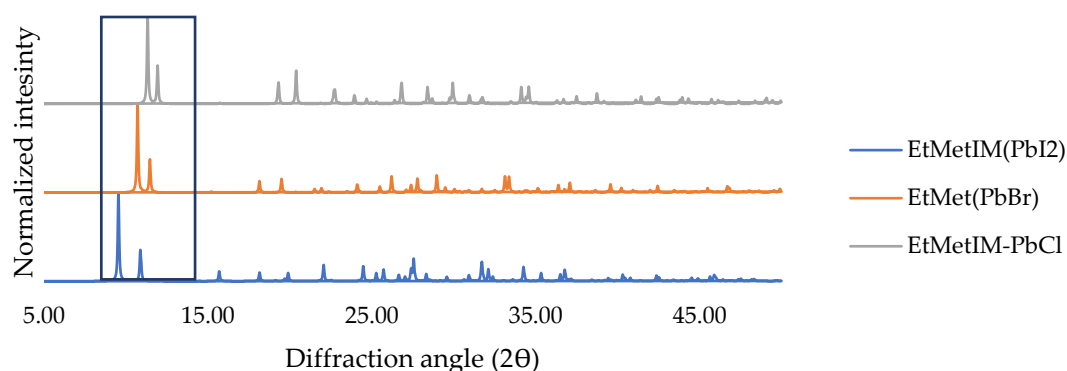
Figure 5.13. C$_2$ImMet lead halides simulated XRD spectra: lead chloride (grey), lead bromide (orange), lead iodide (blue). Initial peak squared in blue, data from [115,116]

Initial peaks (region between 5° and 15° values of diffraction angles) of simulated XRD powder spectra are related to distances among planes containing lead halide chains, as described by simulated powder XRD (in Figure 5.14 example for 1-ethyl-3-methylimidazolium lead bromide).These peaks are stronger because of their anisotropic structure in this direction of 1D perovskite inorganic sublattice. So, inside perovskite lattice, lower distance among planes results in lower lead halide interchain distance inside unit cell.
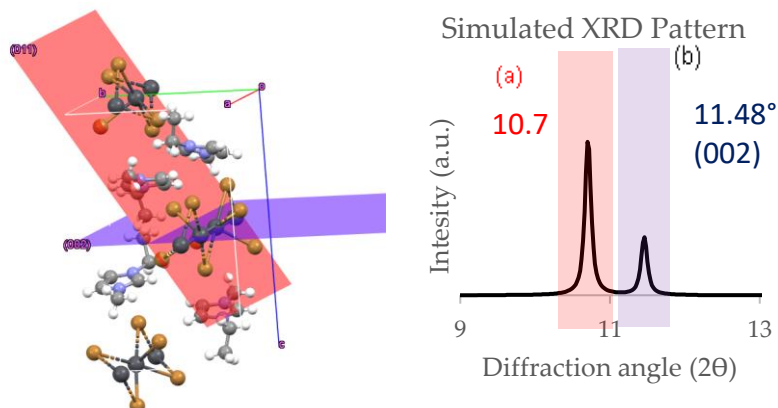
Figure 5.14. Ethyl-methyl imidazolium lead bromide crystal structure with crystallographic planes related to inorganic chains direction in purple and red (bottom). Computed XRDP related to (hkl) planes (right), data from.[115]

Given the fact that higher distances among planes need lower angles for scattering, signals in XRD are shifted to lower values thus increasing distance among previously described planes.[128] So, peak shift observed in PXRD is the result of lower distance among planes parallel to alkyl chains. These planes can be used to describe molecules inside perovskite unit cell. Therefore, inorganic chains and cations distances inside unit cell are affected by spacing among the planes described in low angle peaks.

In this work, distances between lead halide chains inside unit cells have been compared for different perovskites (Appendix B). Firstly, it was evaluated in relation to literature data and then to obtained compounds. These values were then compared to peaks values in PXRD spectra of C_nImMet(PbBr$_3$) (n from 2 to 6), as shown in Figure 5.15 and Table 5.6. Crystallographic plane (002) is parallel to lead halide chains and can be found in all spectra. Moreover, it was set as the reference to evaluate the change in crystal structure with alkyl chains length. Other planes are related to different symmetry of unit cell. Peaks of these planes (Figure 5.15) show a trend: longer alkyl chain shifts initial peaks to lower angles, suggesting higher distance among diffraction planes. This trend is also present in data about distance among lead bromide chains shown in Table 5.6. So, apart from butyl-methyl which is a 0D structure[61], increasing alkyl chain length results in an interesting effect on crystal structures and their related XRD signals.
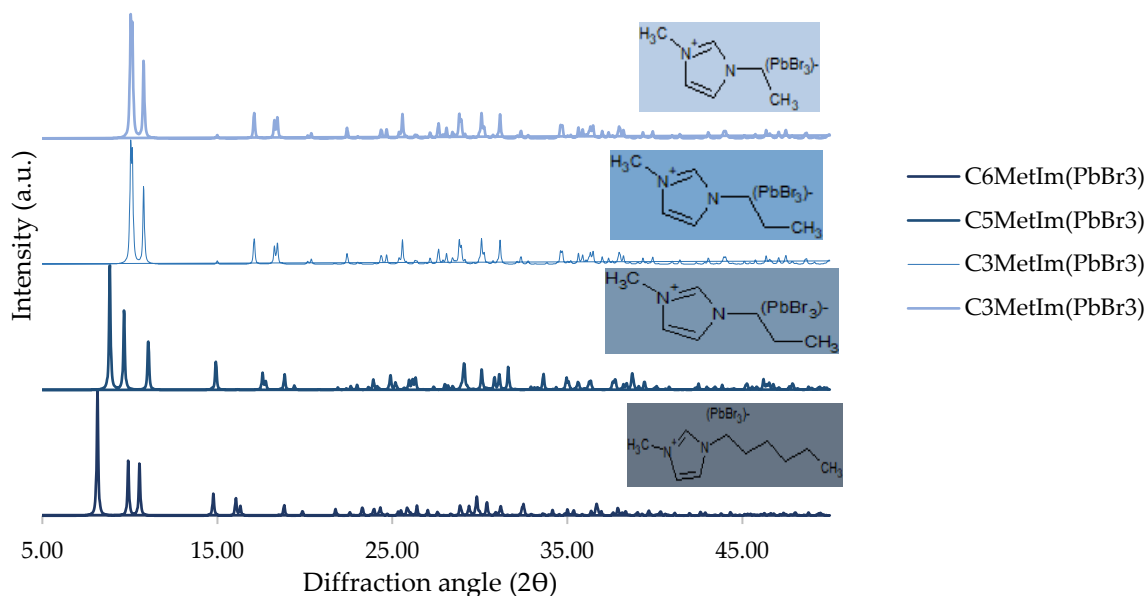
Figure 5.15. Alkyl-methylimidazolium lead bromide 1D perovskite powder XRD
spectra simulated from single crystal, data retrieved from [60,62,115]

Table 5.6. Alkyl-methylimidazolium lead bromide 1D perovskite PXRD initial peaks
values (with planes) with PbBr chains distances (D(PbX)), data from [60-62,115]

	First peaks values (crystallographic planes)	D(PbX) (A)	Bond lenght dist. (Δd) [A]→%	Angle distortion (σ^2)→(σ/90°)
C₂ImMetPbBr₃[115]	10.71 (011), 11.48 (002)	9.77	0.0067 %	150.81[(1)] →13.6%
C₃ImMetPbBr₃[60]	10.04(002), 10.14(100), 10.94(10-2)	9.86	$0.52*10^{-4}$ %	21.16→5.1%
C₅ImMetPbBr₃[61]	8.86(002), 9.64(10-1), 11.01(101)	10.44	0.251%	96.43
C₆ImMetPbBr₃[61]	8.13 (002), 9.901(10-1), 10.5 (101)	11.51	0.234%	74.46→7.8%

Then data obtained in this work were compared to the lead bromide, due to same 1D
face sharing structure of obtained C₂ImMetPbI₃ and C₂ImMetPbI₃. The previous trend

was confirmed by C$_2$ImMet and C$_3$ImMet lead iodides results of this study combined with imidazolium lead iodide data (1D perovskite single crystal structure reported by Seth et al.[114]). As described in Table 5.7 and Figure 5.16, a different lattice arrangement affects lead iodide distortion parameters and distance among lead iodide chains, which is related to initial peaks in XRD powder. In addition, (002) plane peaks for alkyl-methyl imidazolium perovskites follow the same trend of lead bromide counterparts, as shown in Figure 5.17. Distance among these planes increase from 9.899 A to 10.375 A adding 1 carbon atom to alkyl chain, as shown in Figure 5.16.
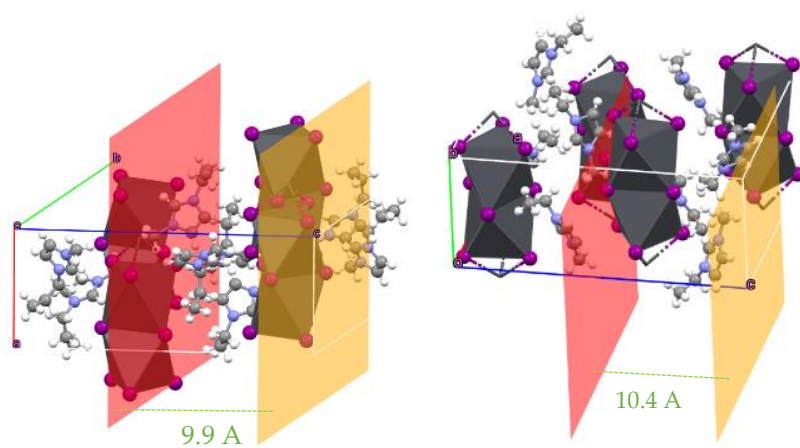
Figure 5.16. C$_2$ImMet and C$_3$ImMet lead iodides single crystal structure with (002) crystallographic planes parallel to lead iodide chains

Table 5.7. Imidazolium lead iodide, C$_2$ImMet and C$_3$ImMet distortion parameters and distance among lead iodide chains (D(PbX)= distance among lead iodide chains)

	Bond length distortion(Δd) %	Angle distortion (σ^2)$\rightarrow$($\sigma/90°$)	D(PbX) (A)	Peaks at low angles (planes)
Imidazolium-PbI$_3$[114]	$1.84*10^{-6}$ %	$21.29 \rightarrow 5.1$%	9.42	11.31(2-10), 12.8(201), 13.19(200)
C$_2$ImMet-PbI$_3$	$1.1*10^{-4}$ %	$48.41 \rightarrow 7.7$%	9.75	8.93(002), 9.96(200),10.2 (102)
C$_3$ImMet-PbI$_3$	0.297%	$38.78 \rightarrow 6.92$%	10.375	8.28(002), 9.65(012), 9.87(020)

Before moving on to overall powder XRD data analysis, a comparison among simulated data obtained from single crystal is needed. To ensure that analyzed single crystal is significant in respect to sample, simulated and experimental data must fit for the main peaks. As described in Figure 5.17, peaks of XRD powder of C_2ImMet and C_3ImMet lead iodides correspond to simulated pattern obtained from single crystal data.
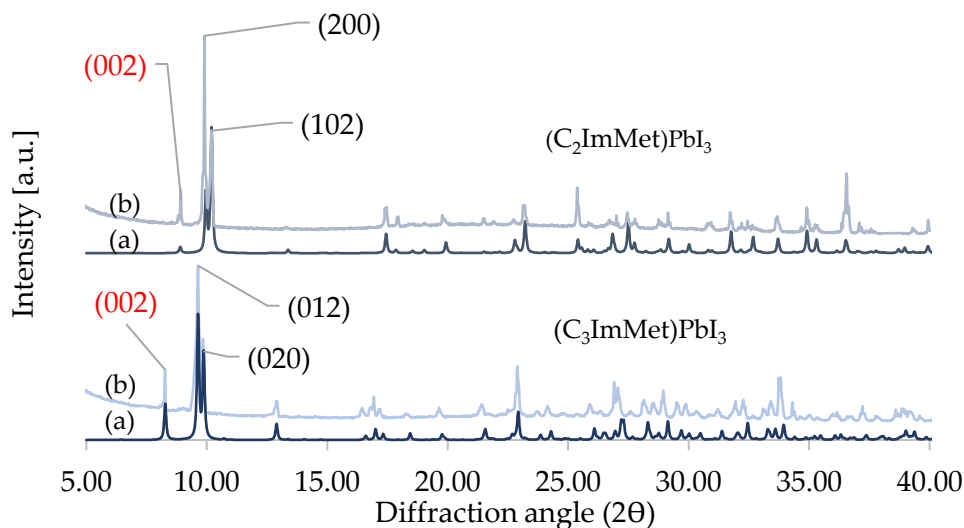
Figure 5.17. (left) Comparison among PXRD simulated single crystal data and experimental data for C_2ImMet and C_6ImMet lead iodides ((a) single crystal, (b) experimental), signal analyzed in Table 3 are reported with planes

Unluckily, for C_nImMet lead iodides with n>3, crystal quality was not enough to resolve single crystal structure, due to the disorder induced in perovskite structure by long alkyl chains. Only C_8ImMet lead iodide allowed a partial resolution of single crystal structure only for lead iodide sublattice, as shown in Figure 5.18. This structure was characterized by lead iodide chains composed by two lead atoms. However, 1D structure crystallographic planes were found in PXRD spectra, as shown in Figure 5.18, even with different order among peaks of planes. The "additional" lead atoms change peaks order in simulated PXRD diffractogram, however, peak with minimum angles still follow trends observed for $(C_2ImMet)PbI_3$ and $(C_2ImMet)PbI_3$.These data were used as comparison among PXRD values, due to unavailable experimental diffractogram for this compound. For plane (002) trend is not respected due to different type of lead iodide chains.
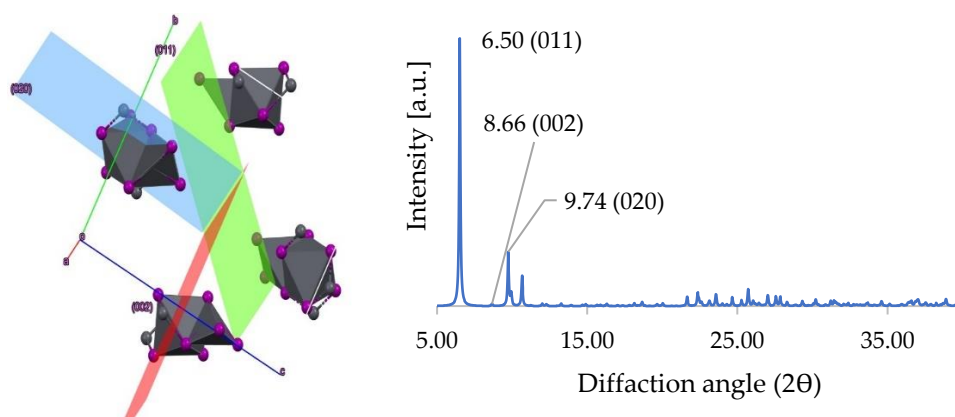
Figure 5.18. (Left) C₈ImMet lead iodide partially resolved single crystal structure with main crystallographic planes parallel to lead iodide chains, (right) simulated PXRD with peaks related to planes

Based on these observations and data collected from single crystal structure of C_2ImMet and C_3ImMet lead iodides, comparison among different alkyl chains was carried out through PXRD diffractogram. These results show the same trend of lead bromides perovskites[60,62,115], so it could be assumed that obtained compounds have a similar 1D structures, despite (002) plane position is modified. As shown in Figure 5.19 peaks parallel to alkyl chain is shifted to lower wavelengths, moreover computed distance among lead iodide chains is coherent with these data.

Based on this assumption, all analyzed perovskite could be ascribed in the trend previously described with alkyl-methyl imidazolium lead bromide [60,62,115], as shown in Figure 5.19. However, it was noticed that for longer chains, signals are stronger in a particular direction. This effect can be made by different crystallization techniques that creates crystallographic planes orientation.

An interesting effect was obtained with dodecyl-methyl imidazolium perovskite, where the peak at low angles is slightly higher than hexyl-methyl imidazolium. This effect could be explained by the use of long chain of crystalline liquids which create different arrangement of lead iodide sublattice. This creates lower distance among lead iodide chains.
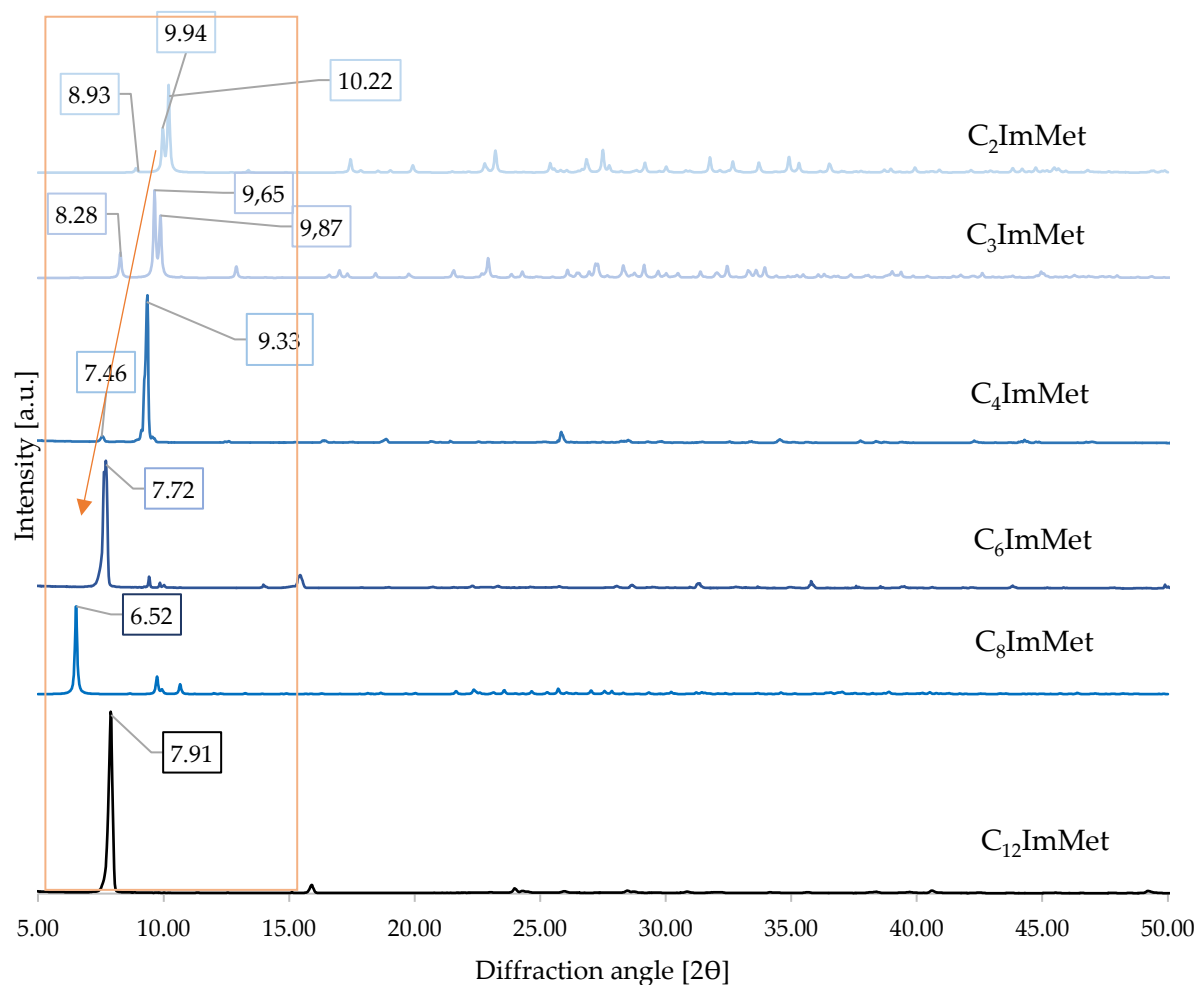
Figure 5.19. Alkyl-methyl imidazolium lead iodide XRD spectra. Comparison among experimental values with observed trend on low-angle peaks, inside orange box low angle region peaks, with decreasing trend

So, XRD powder spectra can give information about spacing effect of imidazolium cations alkyl chains. This insight could be useful for further studies on this parameter which can affect optoelectronic properties of lead halide perovskites. Distortion parameters are affected by this effect, as observed for propyl and ethyl chains.

The same analyses were performed for C_5F_7ImMet and $C_9F_{13}ImMet$ lead iodide perovskites. It must be noticed that this compound does not show superimposable peaks with reagents signal, for example for $C_9F_{13}ImMetI$- based perovskite shown in Figure 5.20.
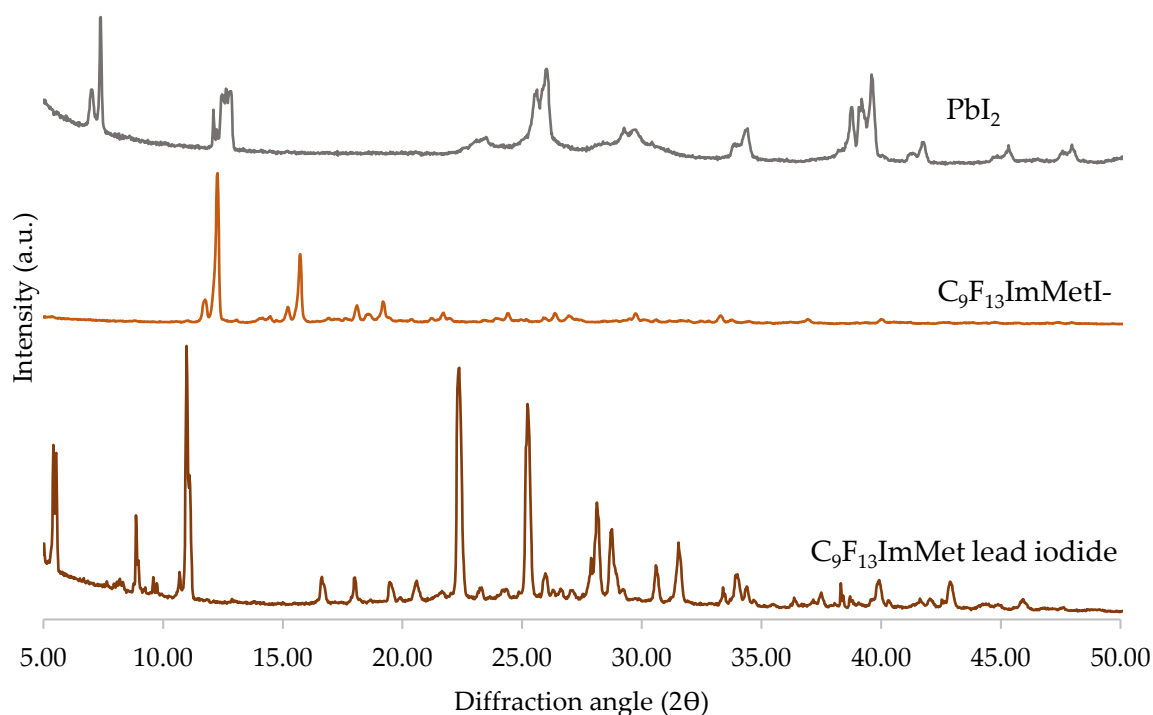
Figure 5.20. PXRD comparison among $C_9F_{13}ImMetI-$, PbI_2 and $C_9F_{13}ImMet$ lead iodide

As visible in Figure 5.21, these compounds exhibit a strong peak at 5.4°, which is different from lowest angles small peaks present in alkyl-methyl imidazolium perovskites. These data suggest the creation of a different lead iodide lattice for alkyl-methyl-imidazolium iodide perovskite. Based on previous work on lead iodide perovskite these peaks could be ascribed to different shape of 1D chains.

Other important peaks at angles between 8° and 10° are present. Unluckily, single crystal structure was not fully resolved, due to strong disorder and low quality of crystals. Therefore, these peaks cannot be ascribed to a particular lead halide sublattice trend, given their difference with respect to alkyl-methyl imidazolium perovskite organization. One hypothesis about similar values of angles could be related to different packing of perfluoroalkyl chain in $C_9F_{13}ImMet$ perovskite induced from self-assembly effect of long perfluoroalkyl chain.
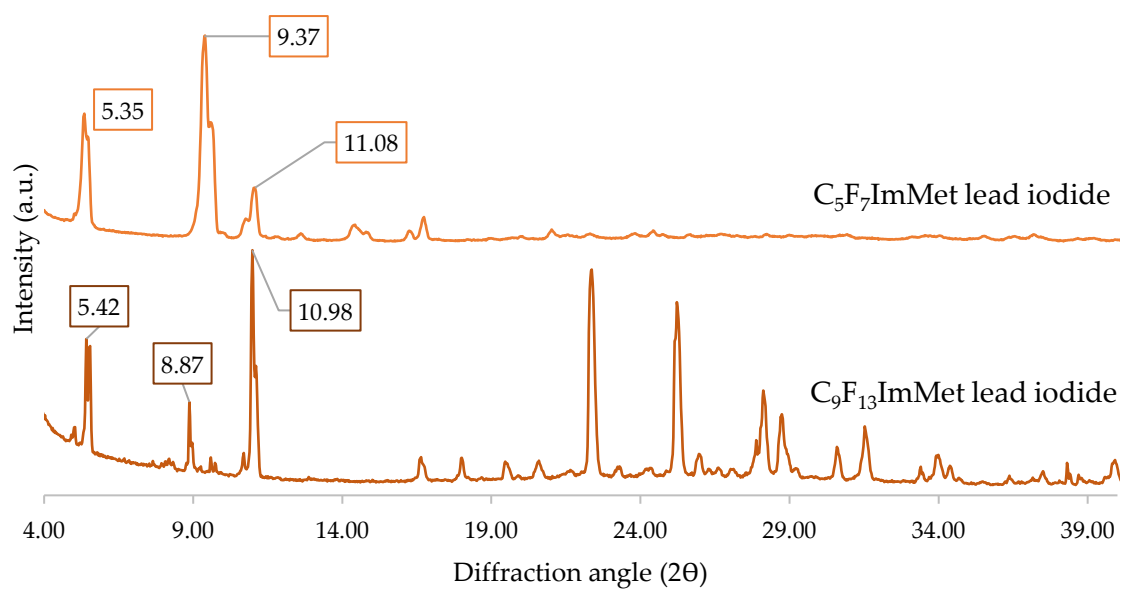
Figure 5.21. Comparison among C₅F₇ImMet and C₉F₁₃ImMet lead iodide powder XRD spectra, with peaks in initial region

So, starting from these results, thermogravimetric analysis and optical characterization were used to investigate effects of crystal structures analyzed in this chapter.

5.3   Thermogravimetric analysis (TGA)

Thermal stability of imidazolium perovskite has been investigated through TGA to understand their degradation temperature. Before examining results of experiments in this work, a brief overview about imidazolium perovskite TGA results was discussed. However, they are related to alkyl-methyl- imidazolium lead bromide perovskites and imidazolium lead iodide.[60-62] The above-mentioned results have been studied to understand general processes and degradation temperatures for these materials.

Previous TGA of imidazolium lead bromide perovskites shows two degradation steps:

1. Organic cations degradation with evaporation of HX (where X is halogen anoin in imidazolium salts) decompose perovskite structure in PbX_2. This degradation usually happens with a peak around 200-300°C, as shown in Table 5.8. This step is responsible for perovskite degradation induced by cations. This step was analyzed in this work to understand temperature of dergadation of perovksites and so thier limit of stabilty for possible applications. Analysis of these step was carried out also with first derivative of TGA with repsect to temperature[61]

2. PbX_2 sublimation at temperatures higher than 400°C with total loss of mass

Table 5.8. Imidazolium lead bromides perovskites degradation onset (*=0D perovskite) data from [61]

	$C_2ImMet(PbBr_3)$	$C_3ImMet(PbBr_3)$[60]	$C_4ImMet (PbBr_3)$ [61]	$C_5ImMet (PbBr_3)$ [61]	$C_6ImMet (PbBr_3)$ [61]
Tdeg	210°C	230°C	260°C	320°C	210°C

Imidazolium lead iodide data confirmed this degradation trend with a double peak in graphs of TGA derivative (computed as derivative of percentage of loss mass with respect to temperature), shown Figure 5.22, as red line. Here is reported also from lead iodide perovskite an onset of degradation induced by cations degradation.[114]
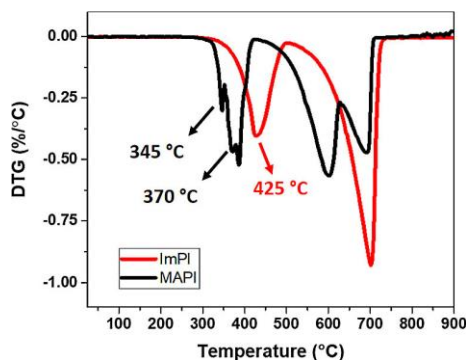
Figure 5.22. First derivative thermo-gravimetric plots of ImPI and MAPI.[114]

Before perovskite analysis, TGA of lead (II) iodide (Figure 5.23) was carried out to understand how residual PbI_2 decomposition affects wight loss in thermogravimetric analysis. From TGA analysis performed in this work, the onset of degradation (T_{deg}) was found around 390°C, which is coherent with literature data. [129] Based on this result perovskite degradation temperature was compared to this value to verify effective presence of imidazolium cations with their degradation at lower temperatures.

$$PbI_2$$
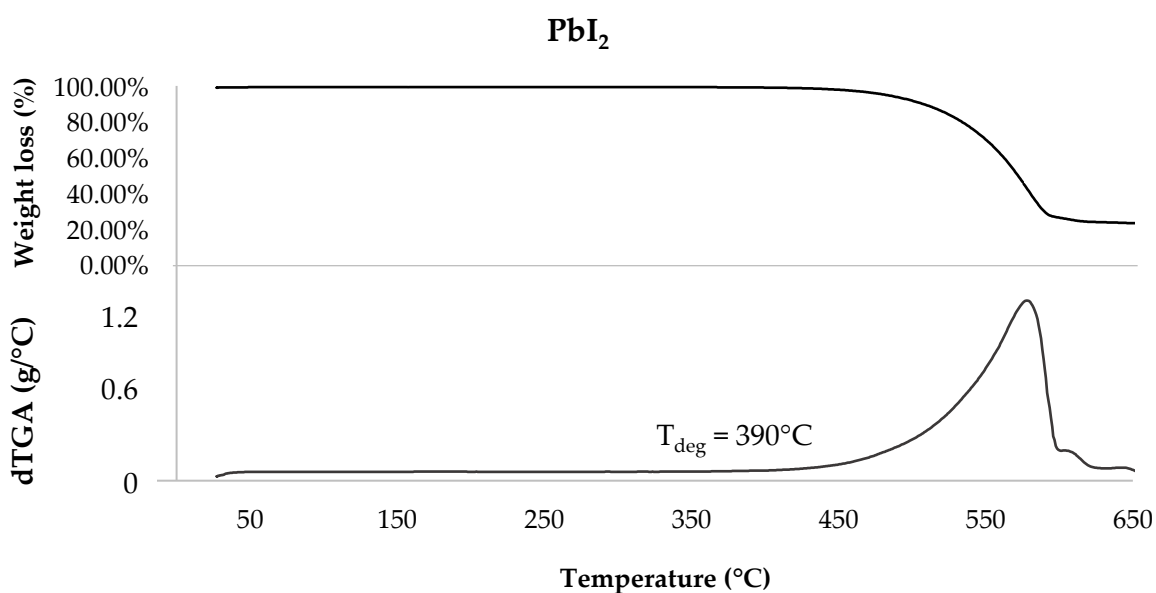
Figure 5.23. Lead (II) iodide thermogravimetric analysis Weight loss and derivative of mass with respect to temperature (dTGA) in function of temperature

Regarding compounds synthesized in this work, TGA plots show a typical degradation onset around 250-270°C that can be ascribed to imidazolium degradation, as described from C$_4$ImMet example in Figure 5.24. Unluckily, as shown in Figure 5.24,

degradation peak of imidazolium cations overlaps with degradation of lead iodide, making difficult to compute degradation path of these materials.
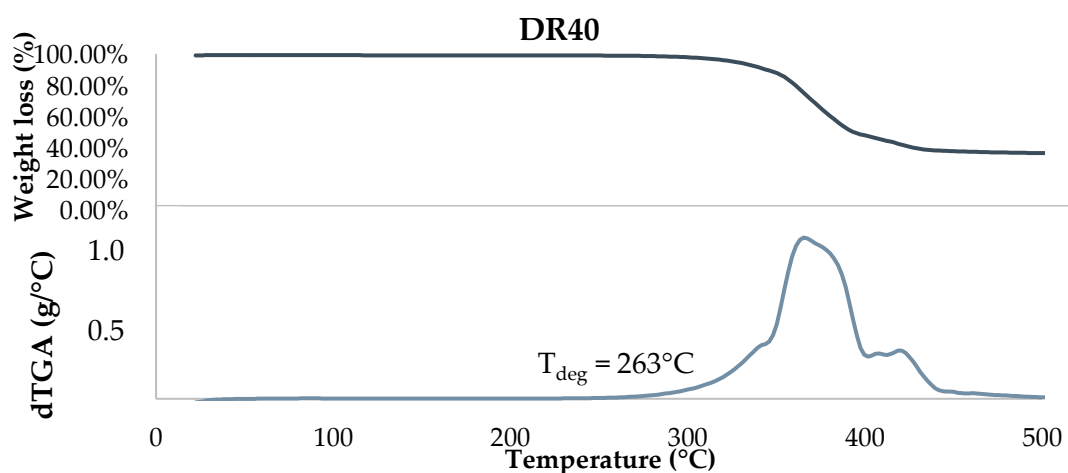
Figure 5.24. C4ImMet lead iodide Weight loss and dTGA in function of T

TGA measurements of alkyl-methyl-imidazolium perovskites show similar characteristics: degradation onset between 250 and 270°C made from imidazolium cations degradation, and main degradation peaks around 300-400°C (Table 5.9). These peaks appear at lower temperatures with respect to imidazolium lead iodide[114]. This effect could be ascribed to absence of strong H-bonds induced by two free nitrogen atoms.

Table 5.9. Onset and peak degradation T for C_nImMet lead iodide perovskites

Cation	Onset of degradation	Degradation peak
C_2ImMet	253°C	364°C
C_3ImMet	268°C	369°C
C_4ImMet	263°C	367°C
C6ImMet	254°C	363°C
C_{12}ImMet	259°C	422°C

Perovskites with fluorinated cations show similar behavior, as described by Figure 5.25. But with these perovskite, double degradation peaks in dTGA occur at two different temperatures. In this case, as described by Table 5.10, values for degradation are from 200°C (C_5F_7ImMet perovskite, with a lower degradation temperature induced

by lower stability of short, fluorinated alkyl chains) and higher values for $C_9F_{13}ImMet$ perovskite (259°C).
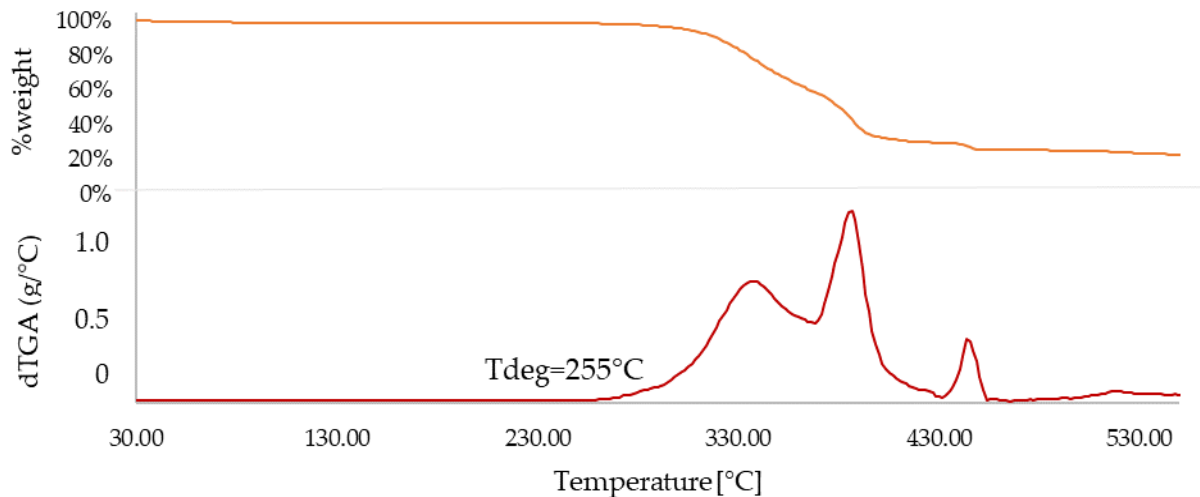
Figure 5.25. ($C_9F_{13}ImMet$) lead iodide wight loss (green) and dTGA (blue) in function of T

Table 5.10. Onset and peak degradation T for Perfluoroalkyl-ImMet lead iodide perovskites

Cation	Onset of degradation	Degradation peak
C_5F_7ImMet	207.6°C	328°C,502°C
$C_9F_{13}ImMet$	255°C	320°C, 408°C

So, TGA results show degradation onset higher than limits for good stability during operational temperature (reported for critical lead halide LEDs perovskite around 110°C), making these materials interesting for these applications.[30,130]

Given similar values for degradation temperatures, alkyl-methyl perovskites were analyzed with differential scanning calorimetry until 250°C, to avoid sample degradation.

5.4   Differential scanning calorimetry (DSC)

Differential scanning calorimetry has been studied to evaluate phase transitions in perovskites. Their phase transitions were reported as discontinuity in DSC thermogram made from different space reorganization of lead halide lattice. Shi et al.[60] reported phase transitions for propyl-methyl imidazolium lead bromide, based on endothermic peaks in DSC analysis at 256 and 359 K. These phases were observed thanks to XRD peaks changes inside these regions, as shown in Figure 5.26.[60]
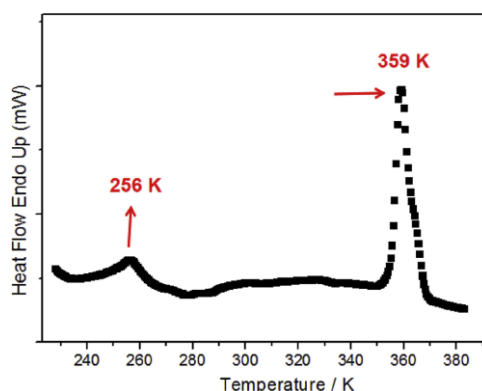
Figure 5.26. DSC curves for C_3ImMet lead bromide in the heating process showing heat anomaly at 256 and 359 K[60]

The melting point has been reported at 102 and 113°C respectively for pentyl and hexyl methylimidazolium lead bromide. However, cooling process does not produce exothermic peak but shows a supercooling behavior.[61] In addition, a phase transition for C_6ImMet lead bromide happens at 250 K, because of cations' more vigorous dynamic motion in the lattice. This effect was explained with discontinuity in lead bromide distance from single crystal data. So, in lead bromide perovskites mediated from H bonds, cations motion affects perovskite transitions.[62] This effect was reported also for imidazolium lead iodide perovskite, with phase transition at 94°C, as described in 2.3.3 section. Here a transition to more symmetric structure was proven by merge of XRD peaks.[114]

Based on these observation C_nImMet lead iodide perovskite has been analyzed in a range between -100°C (to investigate low temperature transitions) and 250°C (to study effect at high temperature).

First, C_2ImMet lead iodide exhibits a phase transition at 212°C (with a small endothermic peak) before melting at 239°C (described by a higher endothermic peak). Melting and solidification steps are proven in cooling and heating cycles, as shown in peaks in Figure 5.27. However, given short chains, supercooling behavior is not observed for this perovskite.
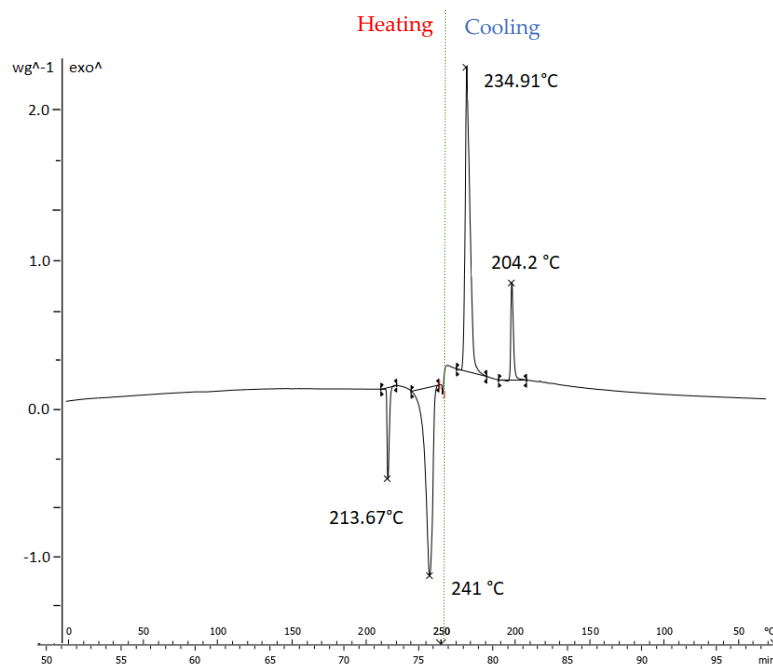
Figure 5.27. DSC of C₂ImMet lead iodide from room T to 250°C with integrated peaks

In this work, different behaviors were observed with different alkyl chains, as shown from comparison among C₃ImMet and C₄ImMet perovskites (Figure 5.28). In the first one a transition occurs at 181°C and it is replicated also in cooling cycles at 154°C (Figure 5.28a). This transition turns out to be perovskite melting. C₄ImMet exhibited the same behavior with respect to propyl counterpart, but with transitions at lower temperature: 118°C during heating process and 108°C for cooling process (Figure 5.28b).

While for longer chains an initial melting of the material was observed but without followed peak of recrystallization, probably made from supercooling behavior of these materials, as reported for their lead bromide counterparts [61]. This transition happens at 106°C for C₆ImMet lead iodides and at 167°C for C₈ImMet lead iodide, as shown in Figure 5.29. However, for all analyzed perovskites, phase transitions at temperature lower than room T were not detected.
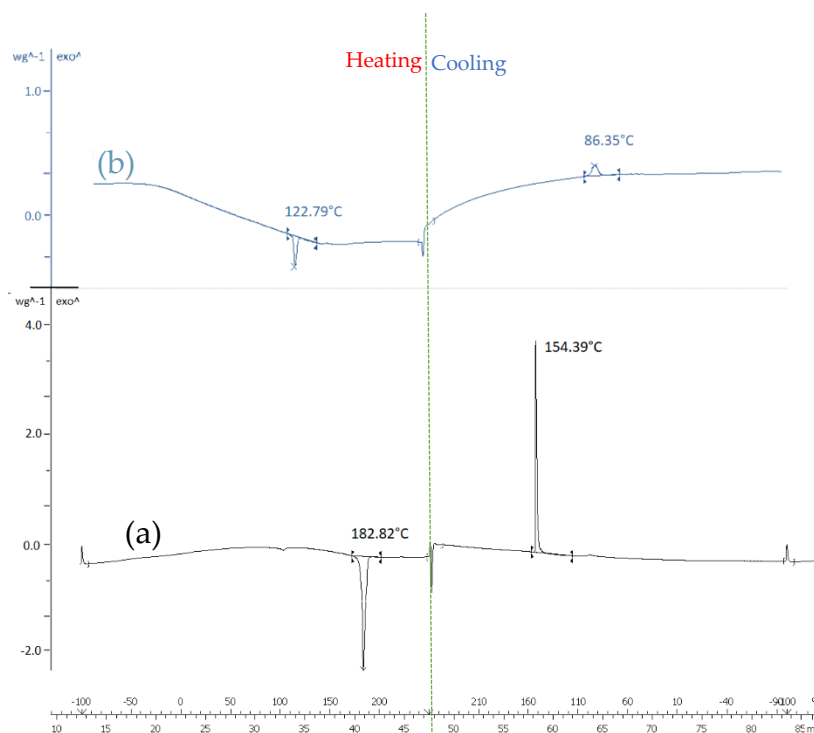
Figure 5.28. DSC thermogram between -100 and 250°C for (a)C₃ImMet and (b)C₄ImMet with peaks
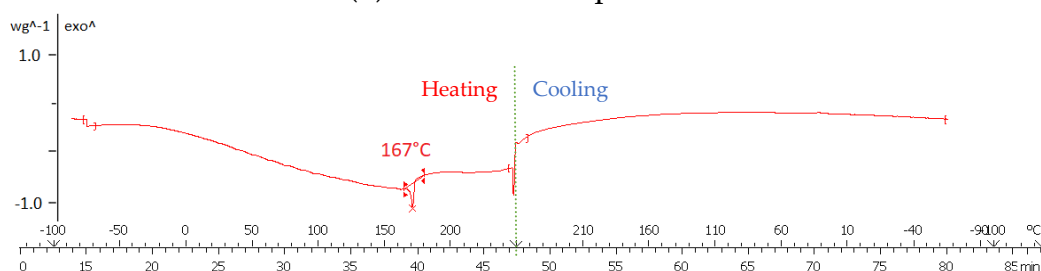
Figure 5.29. DSC thermogram between -100 and 250°C for (a)C₈ImMet with peaks

DSC was used to investigate thermal behavior of perovskite obtained from liquid crystal imidazolium salts. These analyses were made to understand if perfluoroalkyl chain *fluorous-fluorous* interactions is also present in related perovskite. [106] These interactions in initial imidazolium salts results in packing of perfluoroalkyl chains that creates ordered also in liquid phase with a smectic phase A as described in Table 5.11. C₁₂ImMetI- liquid crystal behavior (shown in Table 5.11) allows to compare effect of long alkyl chains in terms of induced order in perovskite at high temperatures. [103] As it will be explained in next pages, liquid crystal behavior was evaluated at transition temperature observed with DSC.

Reported phase transitions temperatures are inside perovskite stability range, as described in section 3.2.3, so DSC have been carried out for these perovskites to assess the effect of liquid crystals as organic cations.

Table 5.11. Liquid crystal imidazolium phase transitions for $C_9F_{13}ImMetI$- and $C_{12}ImMetI$-

Crystal	Type of transition	Temperature	ΔT
$C_{12}ImMetI$- [103]	Crystal→smectic A	27*C	53°C
	Smectic A→isotropic liquid	80°C	
$C_9F_{13}ImMetI$-[106]	Crystal→smectic A	86°C	112°C
	Smectic A→isotropic liquid	198°C	

First, $C_{12}ImMet$ perovskite was analyzed within temperature range from -100 to 250°C. As we can see from Figure 5.30, $C_{12}ImMet$ lead iodide shows two endothermic peaks at 125°C and 194°C during first heating run. Phase transitions were present as exothermic peaks (172°C and 89°C) during cooling run. However, liquid crystalline behavior was not observed with polarized optical microscope. Therefore, long alkyl chains effect present in initial imidazolium salt is not replicated in perovskite. This effect is coherent with higher disorder induced by alkyl chains in perovskite lattice.
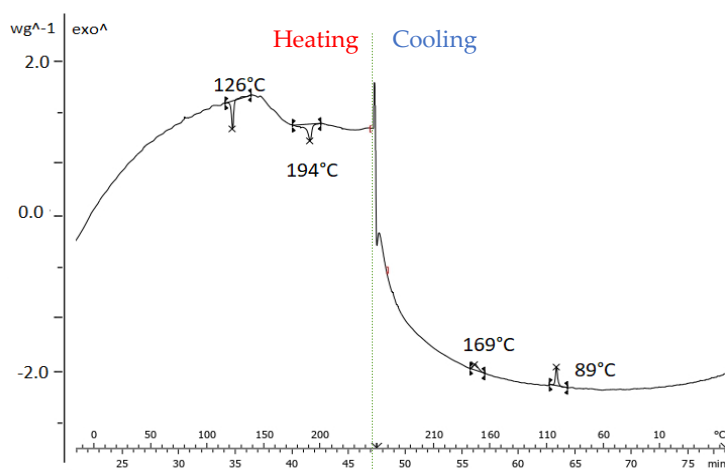
Figure 5.30. $C_{12}ImMet$ lead iodide thermogram from 0°C to 250°C, with cooling and heating rate of 10°C/min

Perfluoroalkyl chain effect was evaluated through comparison among DSC thermogram of initial imidazolium salt and related perovskite, as shown in Figure 5.31. Here three phase transitions are present for both compounds during heating, while for cooling only a single peak was detected. This single peak was reported as supercooling behavior of imidazolium salts. [106] While transitions during heating process are related to creation of smectic phase A and then isotropic liquid. [106] Values for these transitions for perovskite are translated to higher temperature, made from lead iodide effect.
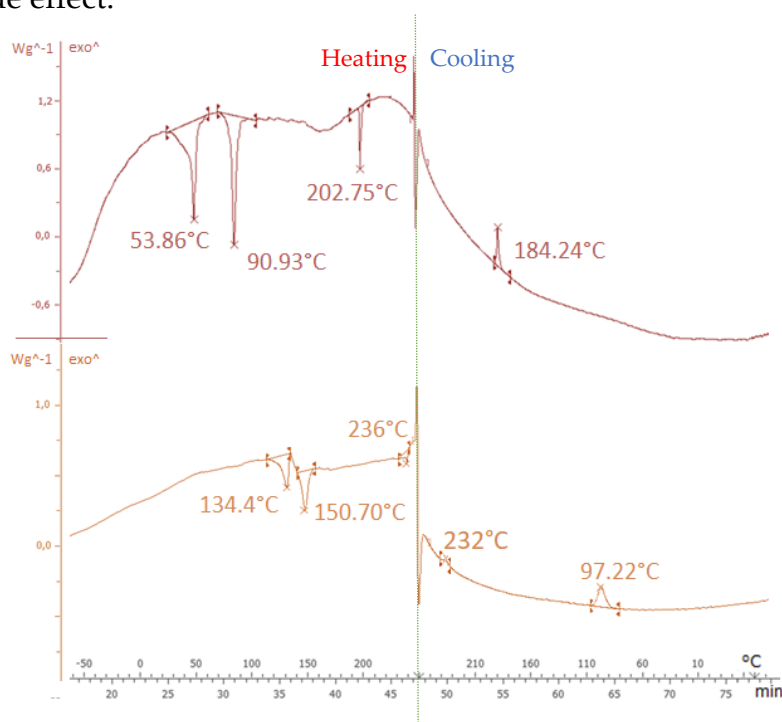
Figure 5.31. Comparison among DSC results of $C_9F_{13}ImMetI$- and $C_9F_{13}ImMetI$- lead iodide

So, behavior of these materials was investigated at these temperature range with polarized optical microscope (POM) to understand nature of these peaks. For imidazolium salts, increasing temperature a smectic phase A appears made from packing of perfluoroalkyl chains that result in an ordered structure also in liquid phase. This effect resulted in birefringence typical of liquid crystal that rotate polarized light. Therefore, with two polarized inclined by 90° light can be detected passing through liquid crystal.

As visible from POM images in Figure 5.32, this perovskite undergoes to an initial melting transition (peak at 134.4°C in Figure 5.31) to pass to a liquid crystalline smectic phase A at 144°C (as shown from peak at 150.70°C in Figure 5.31 and image b in Figure 5.32). This phase remains stable (Figure 5.32c) until it melts as isotropic liquid at 236°C (peak at 236°C in Figure 5.31 and Figure 5.32d). Then liquid crystalline behavior has

been proven also during cooling phase. First isotropic liquid pass to smA at 232°C, visible in (Figure 5.32e and f). Finally at 97°C liquid phase crystallizes in random direction (Figure 5.32g).
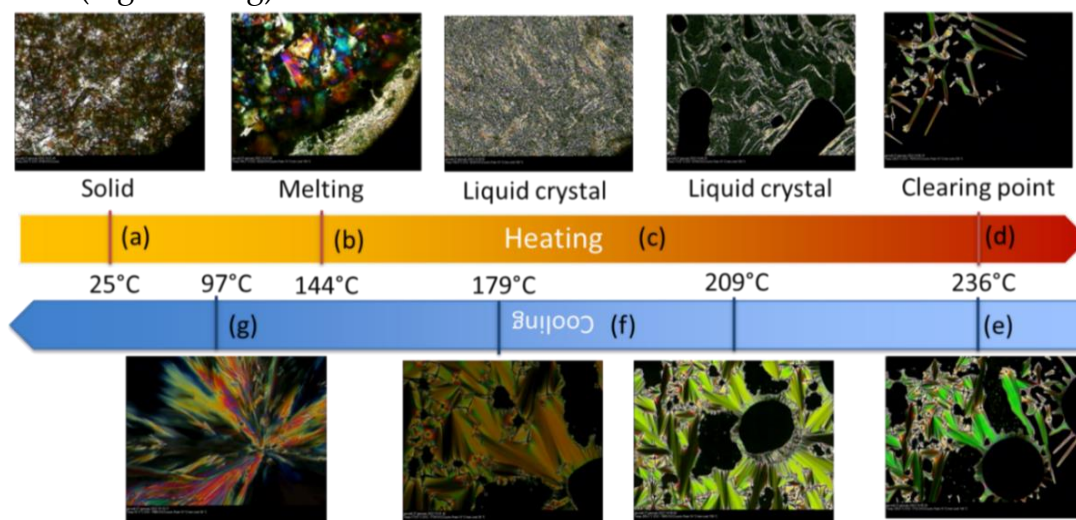
Figure 5.32. POM images with T from 25°C to 250°C, heating (a, b, c, d) and cooling (e, f, g)

Differently from D_{12}ImMet lead iodide, this perovskite could exploit fluorophobic effect typical of these crystals, which it can be assumed that organize themselves to create a liquid crystalline phase also inside perovskite. This effect is not present in C_{12}ImMet.

So, for the first time, thermotropic liquid crystalline behavior in bulk low dimensional perovskite was observed. Other cases about low structural dimensionality perovskite have been reported using nanostructures of 2D perovskites using ligands to separate nanoplatelets. Here lyotropic liquid crystals were obtained with proven 60 days of stability.[129] In this work bulk thermotropic liquid crystals were proven after 90 days. But this behavior has not been observed for bulk materials and this result provides a new insight about low dimensional perovskites properties and possibilities. As ionic liquid counterpart for this perovskite, C_7F_5ImMet lead iodide has also been investigated. No phase transitions are present, as expected from different nature of imidazolium present inside perovskite. Therefore, we can hypothesize that this behavior is induced by higher level of order made by fluorinated long alkyl chains segregation.

5.5   Contact angle measures

Contact angle (CA) measures was made to evaluate effect of perfluoroalkyl chains with respect to alkyl ones on imidazolium lead iodide perovskite. So, thanks to this analysis, this effect for perfluoroalkyl chains was investigated in their related perovskites. Based on previous literature, imidazolium with alkyl and fluorinated chains have been used to passivate perovskite surface, with hydrophobic behavior (contact angles up to 110°). This effect caused an increase in device performance stability over time induced by higher moisture resistance of perovskite part.[71]

As described in section 3.1.3, contact angle measures were carried out on glasses covered by spin coating and drop casting techniques. These techniques were selected as main one for perovskite fabrication: drop casting allows to have a slow evaporation, while spin coating is used as more fast and effective deposition method for perovskite optoelectronic devices. Contact angle measures were compared to control sample (uncoated glass) and imidazolium lead iodide (ImPbI$_3$).

Samples obtained with drop casting were characterized by this technique, before and after annealing step. Contact angle values before annealing shows a trend in increase of contact angle with longer alkyl chains (Figure 5.33 and Table 5.12). Hydrophobic behavior (contact angle higher than 90°) was reported for alkyl chain length higher than 6, with values higher than 90° for C$_{12}$ImMet. This effect was reported also for C$_5$F$_7$ImMet and C$_9$F$_{13}$ImMet perovskite samples, as shown in Figure 5.33 and Table 5.12.
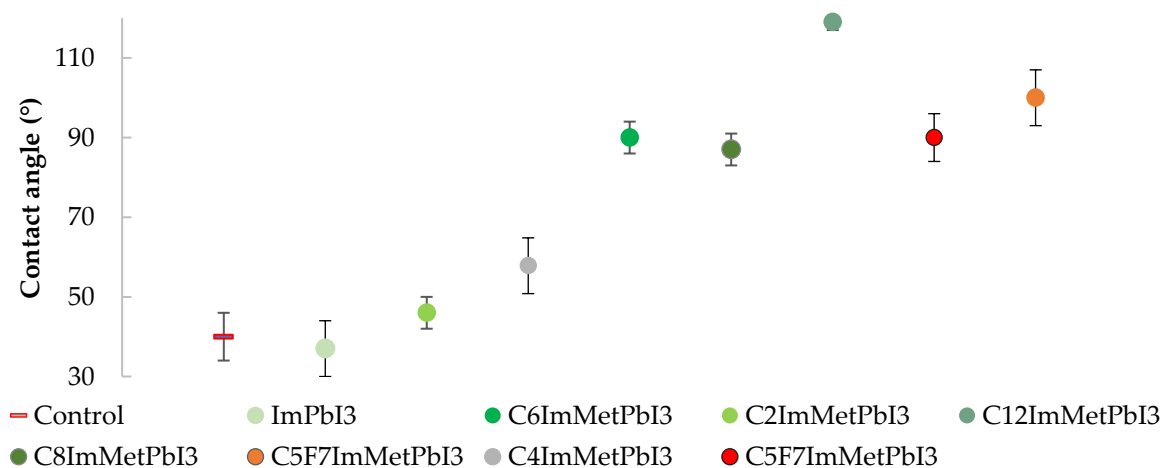
Figure 5.33. Contact angle values for samples coated with perovskite with drop casting

Table 5.12. Contact angle values for samples coated with perovskite with drop casting

Sample	CA
Control	40±6°
Im	37±7°
C$_2$ImMet	46±4°
C$_4$ImMet	58±7°
C$_6$ImMet	98±4°
C$_8$ImMet	87±4°
C$_{12}$ImMet	119±2°
C$_5$F$_7$ImMet	91±6°
C$_9$F$_{13}$ImMet	100±7°

To assess presence of residual DMF inside coatings FTIR analysis were performed on these samples. DMF incorporation can be described by an additional peak in 1600-1730 cm^{-1} region, made from C=O of DMF.

As shown in FTIR spectra of these samples (Figure 5.34), DMF was still present in a small amount, so samples undergone to annealing to remove residual DMF. After this treatment, FTIR measures were performed again and C=O stretching signal was no more detected, as described in Figure 5.34. So, this additional step is needed in coating procedure to evaluate contact angle and avoid possible residue of DMF that can be present in coatings.

However, some inhomogeneity issues were reported for some samples with longer chains, as depicted in Figure 5.35.
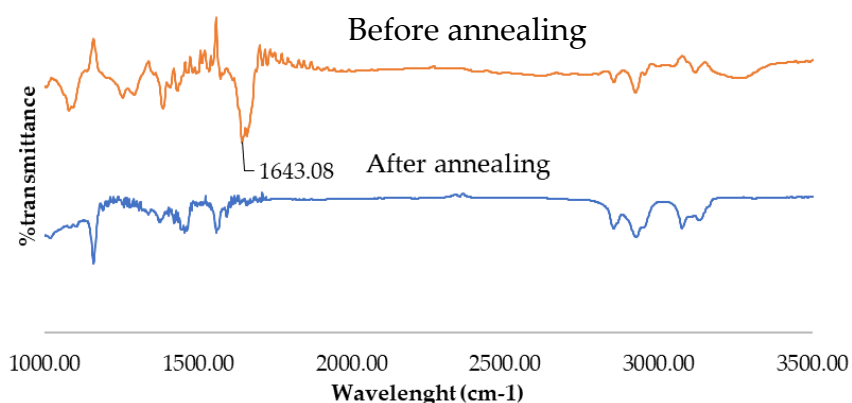
Figure 5.34. FTIR spectra of C$_6$ImMetPbI$_3$ coated sample, with highlighted strong signal associated to DMF before and after annealing
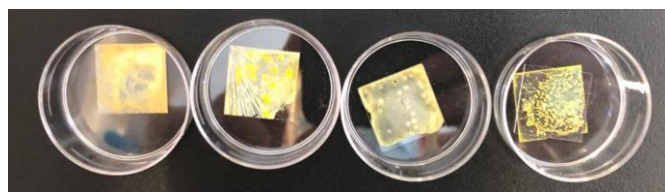
Figure 5.35. From left to right: coating samples for C_5F_7ImMet, C_2ImMet, $ImPbI_3$ and $C_9F_{13}ImMet$ after annealing

After this treatment contact angle measures were performed again, to assess effect of annealing step. Contact angle values shows the same trend with different alkyl chain length and fluorinated chains, as described from Figure 5.37. Contact angle values remain in the same range, with an increase for shorter alkyl chains after annealing step, as shown in Table 5.13.

Hydrophobic behavior was verified for long alkyl chains and C_5F_7ImMet and $C_9F_{13}ImMet$ lead iodides, as visible in comparison with $ImPbI_3$ from Figure 5.36.
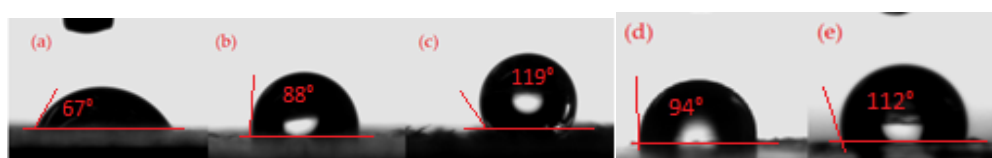
Figure 5.36. (a) Imidazole, (b) C_6ImMet, (c) $C_{12}ImMet$, (d) C_5F_7ImMet and (e) $C_9F_{13}ImMet$ lead iodide perovskite contact angle
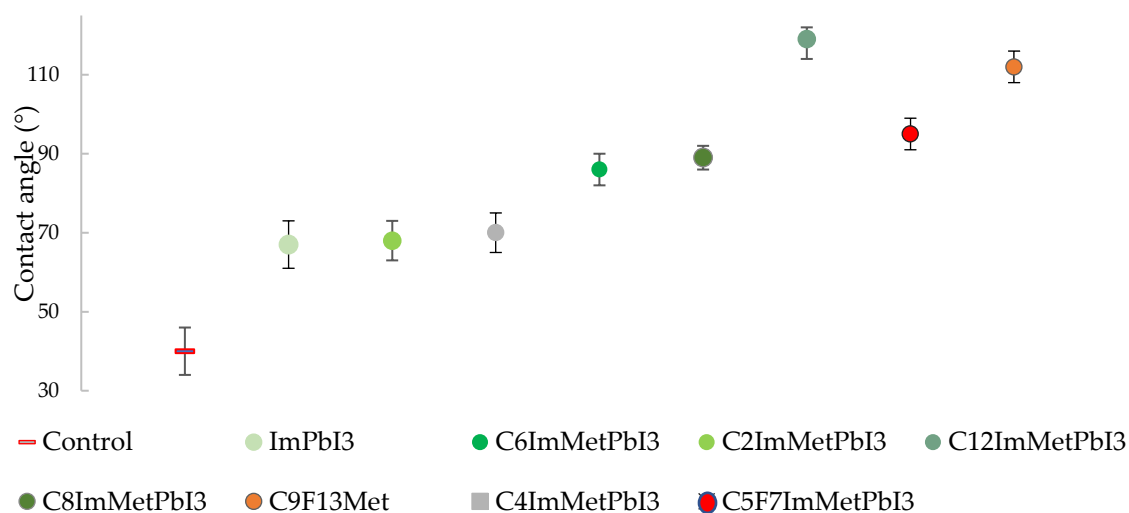
Figure 5.37. Contact angle values after annealing for samples coated with perovskite with drop casting

Table 5.13. Contact angle before and post annealing step

	CA Before annealing	CA post annealing
Control	40±6°	40±6°
Im	37±7°	67±6°
C$_2$ImMet	46±4°	68±5°
C$_4$ImMet	58±7°	70±4°
C$_6$ImMet	98±4°	88±2°
C$_8$ImMet	87±4°	89±3°
C$_{12}$ImMet	119±2°	119±9°
C$_5$F$_7$ImMet	91±6°	94±3°
C$_9$F$_{13}$ImMet	100±7°	112±4°

Then, spin coating as deposition technique has been studied for perovskite/DMF solution. However, poor coatings were obtained during this deposition technique due to insufficient amount of material available. Contact angle values were collected, with similar trend and lower values for alkylated imidazolium perovskites (Figure 5.38). We assumed that this effect is induced by problem of recrystallization and chain packing induced by fast evaporation in spin coating or coating inhomogeneity.
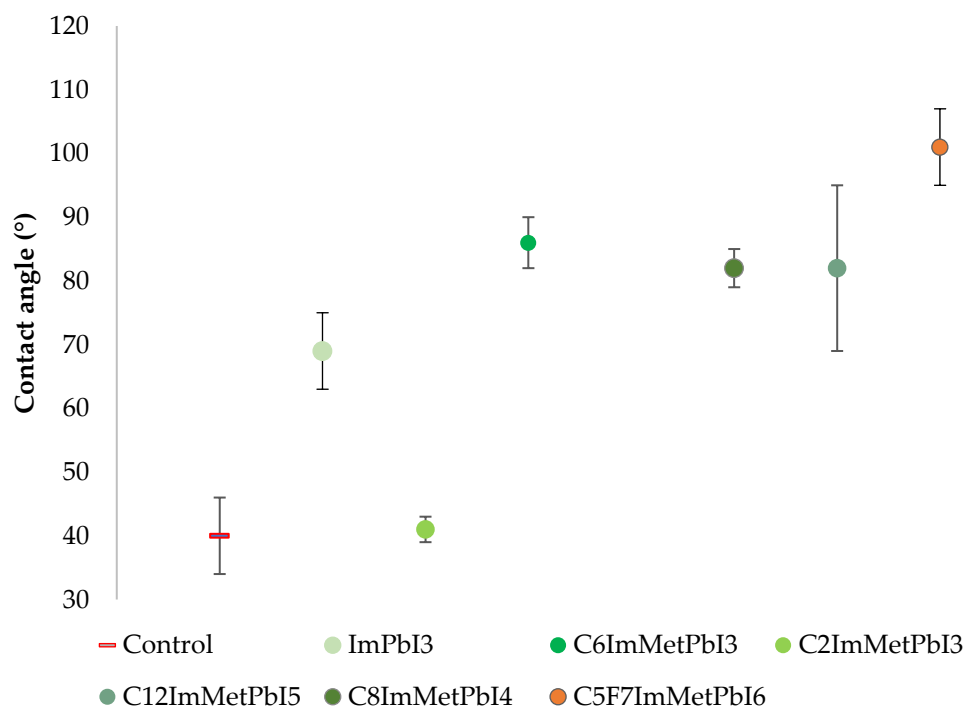
Figure 5.38. Contact angle values for spin coated samples

Table 5.14. Contact angle values for sample deposited with spin coating and drop casting

	Control	Im	C$_2$ImMet	C$_6$ImMet	C$_{12}$ImMet	C$_9$F$_{13}$ImMet
CA Drop casting	40±6°	37±7°	46±4°	98±4°	119±2°	100±7°
CA Drop casting post annealing	40±6°	67±6°	68±5°	86±2°	119±9°	112±4°
CA Spin coating	40±6°	69±6°	41±5°	79±6°	87.1±8°	101±6°
CA Spin coating post annealing	40±6°	59±8°	45±6°	63±9°	82±3°	103±6°

After spin coating samples undergoes to annealing, with similar values for contact angles for C$_9$F$_{13}$ImMet and lower values for alkylated imidazolium chains. This effect could be ascribed at arrangement of the chain and lower hydrophobic barrier with lower quantity of perovskites. While C$_9$F$_{13}$ImMet maintains its hydrophobic effect related to fluorinated chains. Based on this results perfluoroalkyl chains hydrophobic effect was assessed with both techniques. However, spin coating techniques for fabrication of thin film perovskite must be further optimized for these materials.

5.6   Photophysical characterization

UV-Vis absorption spectroscopy was used to determine onset of absorption of these materials. Based on previous results on alkyl-methyl imidazolium lead bromide [61], absorption onset is mainly related to exciton in lead bromide chains in 500-650 nm region.[61] In some cases, shoulders induced by transitions from valence band to π^* orbitals of organic cations were reported. However, this effect is not always present, because a strong interaction among the two parts is needed. For example, pyridinium gives this effect with lead bromide but not with lead iodide. [53]

So, solid state absorption spectra were collected and analyzed for different alkyl-methyl imidazolium perovskite obtained in this work. Through this analysis interaction inorganic-organic sublattices was studied and it was tried to assess effect of alkyl chain on absorption onset. [114] In these lead iodide perovskites (Figure 5.39), exciton peak in lead iodide chains was detected in 350-450 nm region. This effect is coherent with values reported for imidazolium lead iodide (maximum of absorption at 425 nm), considering change of cations. [114]
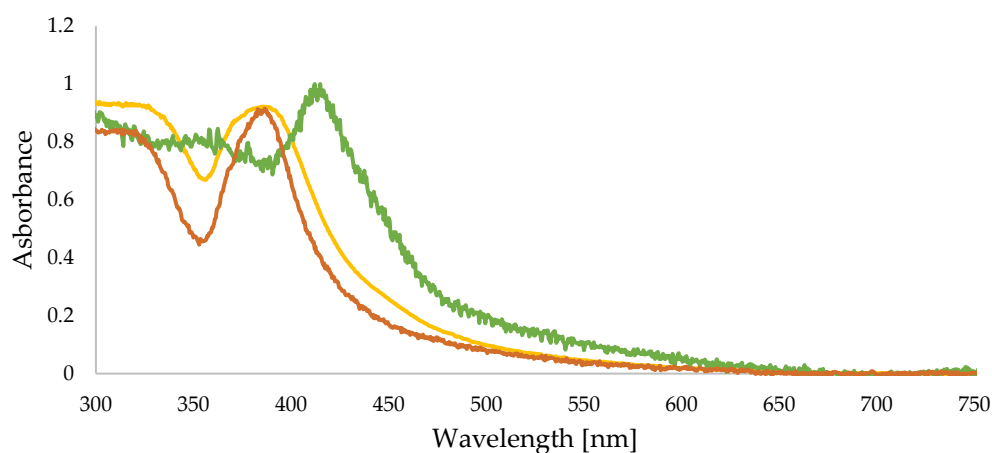
Figure 5.39. Absorption spectra for C_3ImMet (orange), C_4ImMet (yellow), C_{12}ImMet (green) lead iodides

Comparing data of different perovskites, a trend in lower wavelength of absorption onset was found for C_nImMet perovskites, with data for Eg shown in Table 5.15. This effect could be ascribed at different distortion of lead halide chains with longer chains.

Table 5.15. Energy gap calculated with Tauc plot, assuming alkyl-methyl imidazolium perovskite as direct semiconductor

Cation	C$_3$ImMet	C$_4$ImMet	C$_{12}$ImMet
Bandgap	2.6 eV	2.48 eV	2.28 eV

For perfluoroalkyl-methyl imidazolium perovskite similar behavior was obtained in terms of absorption spectra as shown in Figure 5.40. Their absorption spectrum is characterized from a maximum in absorption in the same region of alkyl compounds. So, this peak could be related to exciton in lead iodide chains. Bandgaps were obtained in the same range of alkyl-methyl imidazolium lead iodides, as shown in Table 5.16.
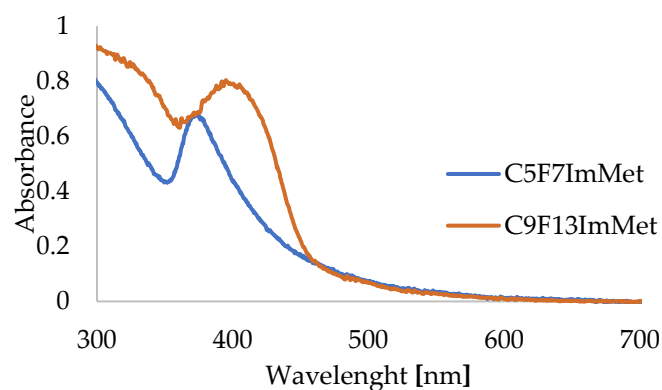
Figure 5.40. C$_5$F$_7$MetIm (blue) and C$_9$F$_{13}$MetIm (orange) lead iodide absorption spectra

Table 5.16. Energy gap calculated with Tauc plot, assuming C$_a$F$_b$ImMet perovskite as direct semiconductor

Cation	C$_5$F$_7$ImMet	C$_9$F$_{13}$ImMet
Bandgap	2.53 eV	2.4 eV

Photoluminescence (PL) spectroscopy has been used to investigate optical behavior of this materials, in terms of emission and lifetime of excited states.

Based on previous results about alkyl-methyl imidazolium lead bromide perovskites, PL has been evaluated at lower temperature to assess thermochromic effect of these perovskites. As described in 2.3.3 section, these perovskites emit with a broad band around 500-750 nm, made from STE. [114] This band is affected by lead halides distortion parameters, induced by different alkyl chain length. Thermochromic effect was obtained through secondary peak at lower temperature 400-500 nm made from imidazolium cations emission.[62] However, secondary peak was not reported for lead

iodide 1D perovskite, probably made from interactions between organic and inorganic electronic subsystems or forbidden transitions.[53,96]

Imidazolium lead iodide data at low temperatures present in literature was integrated are coherent with data at room T of this work. PL spectra reported from [114] PL at variable temperature show a strong enhancement of PL signal related to STE at 688 nm, passing from room T to 10 K.

PL emission of C_mImMet perovskite obtained in this work was made to understand effective photoluminescence emission as 1D materials. For these compounds, as shown in Figure 5.41, broad band emission was found between 400 and 800 nm, with peaks at different wavelength shown in Table 5.17. This peak is blue shifted with respect to imidazolium cations, made by stronger distortion in lead iodide lattice.
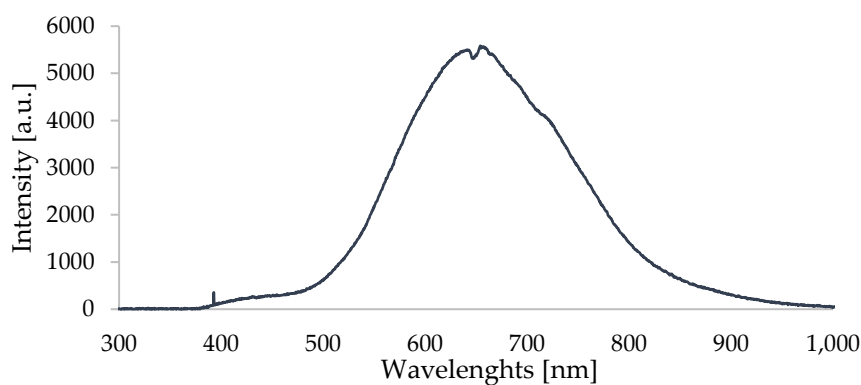
Figure 5.41. C_2ImMetPbI$_3$ photoluminescence spectra at room T

This emission is strongly Stoke shifted with respect to absorption onset. As described before, this effect is made by Self-trapped exciton states created in one dimensional perovskite, giving another indication about analyzed structures. This effect was found for all analyzed samples with some examples shown in Figure 5.42. Moreover, longer alkyl chains shift PL peaks at shorter wavelengths, as reported in Table 5.17. This effect has been reported also for some lead bromide perovskite, and in this work, it was confirmed for lead iodide. [61] Moreover, with long alkyl chains intensity of photoluminescence is reduced, as shown from Figure 5.42. As described by XRD data (Section 5.2), with longer chains, disorder in lattice increases, reducing PL signal. Unfortunately, these materials are characterized by a very strong quenching of PL, therefore their PLQY at room T lower than 1%. So, these materials are not very useful for lighting application. However, they allow to compare effect of alkyl chain length with reduction and blueshift of PL signals.
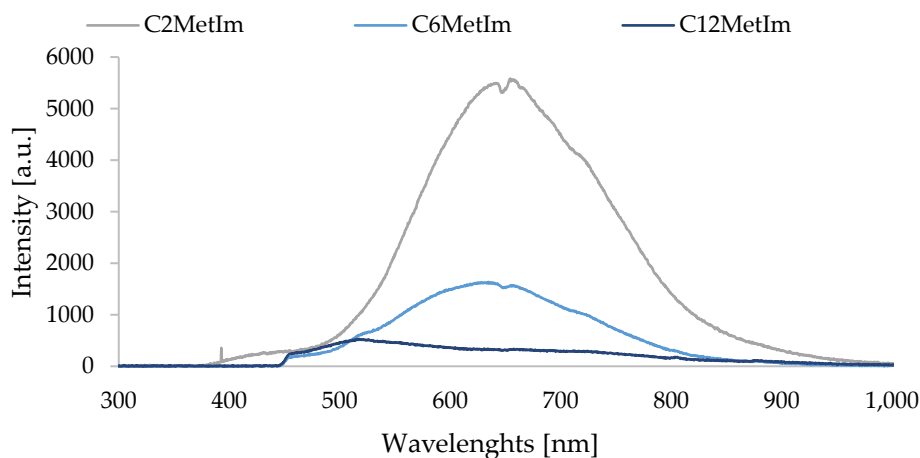
Figure 5.42. PL signals for C_2MetIm(PbI$_3$), C_6MetIm(PbI$_3$) and C_{12}MetIm(PbI$_3$) with excitation at 355nm

Table 5.17. Photoluminescence peak for alkyl-methyl imidazolium lead iodides

Im(PbI3)	C$_2$ImMet(PbI$_3$)	C$_3$ImMet(PbI$_3$)	C$_6$ImMet(PbI$_3$)	C$_{12}$ImMet(PbI$_3$)
688 nm	654 nm	654 nm	635 nm	620 nm

From analysis of C_3ImMet at lower temperature a strong enhancement of PL emission was found as shown in Figure 5.43, made from suppression of non-radiative recombination. For 1D perovskites this behavior is made by lower non-radiative relaxation path induced by coupling with lattice vibration. [114]
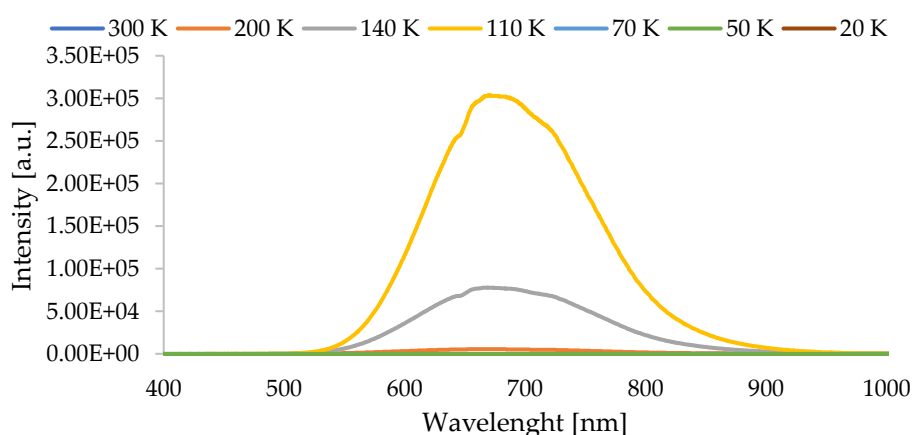
Figure 5.43. PL at variable temperature for (C_3ImMet) PbI$_3$

Time resolved photoluminescence was used to understand recombination dynamics of carriers in excited state. Imidazolium lead iodide shows relaxation time at room T in the order of 0.1 µs (Figure 5.44), coherent with trend observed in literature at higher temperatures (τ = 13 µs at 10 K), which decreases to 2.5 µs at 100K.
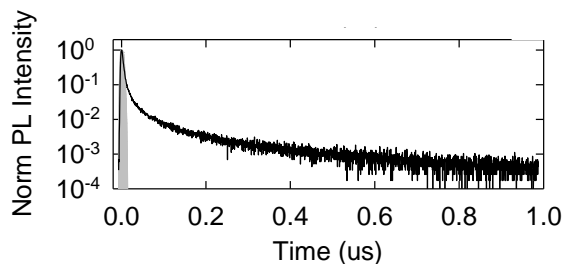
Figure 5.44. PL spectra for imidazolium lead iodide experimental results at 293 K obtained in this work

Obtained spectra show a very fast decay in the order of tenth of ns, as shown from Figure 5.45, related to high number of non-radiative paths for these materials.
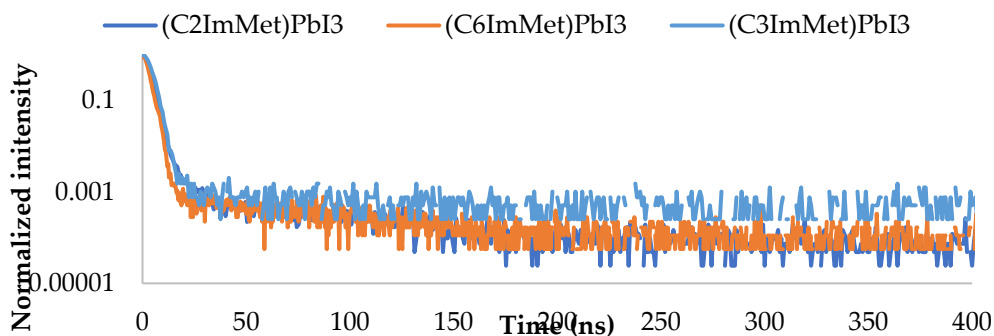
Figure 5.45. Relaxation time for $(C_2ImMet)PbI_3$, $(C_3ImMet)PbI_3$, $(C_6ImMet)PbI_3$ and $(C_{12}ImMet)PbI_3$ at room T excited with 355nm laser

However, perfluoroalkyl compounds show different emission, with narrower peaks that could be ascribed to a different lead iodide sublattice structure, coherent with new peaks in PXRD diffraction. Moreover, photoluminescence peaks are present to lower wavelength with respect to alkyl-methyl imidazolium perovskites, around 520 nm. This effect could be made by different distortion that reduces stoke-shift induced by STE. The shoulder can be made by another phase present in this perovskite. Differently from alkyl-methyl imidazolium perovskites, longer chains results in enhancement of PL emission, as described in Figure 5.46. This effect could be made by lattice arrangement induced by longer perfluoroalkyl chain that results in an increase of the order.
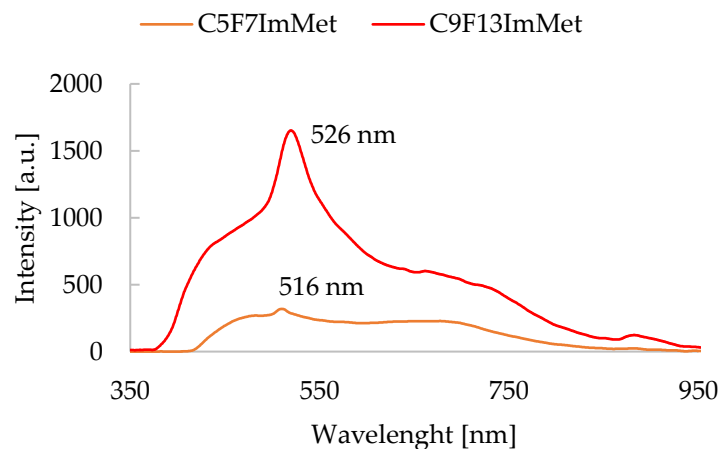
Figure 5.46. C_5F_7ImMet and C_9F_{13}ImMet lead iodide PL at room T excited with 355 nm laser

Thanks to this effect, perfluoroalkyl chain show a photoluminescence higher with respect to C_{12}ImMet and slightly higher than C_6ImMet lead iodides, as shown in Figure 5.47.
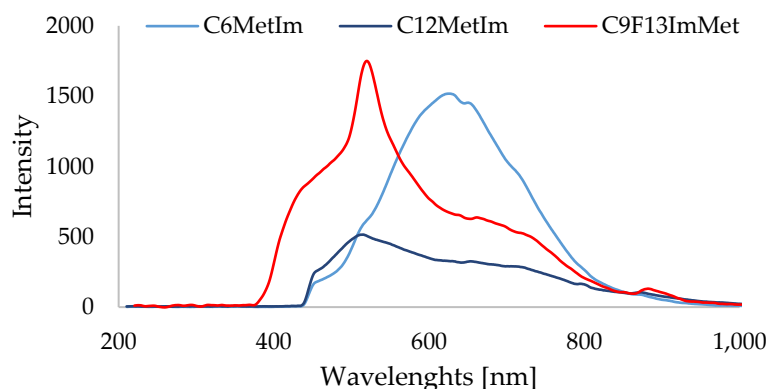
Figure 5.47. C_9F_{13}ImMet, C_6ImMet and C_{12}lead iodides PL at room T excited with 355 nm laser

Moreover, C_9F_{13}ImMet lead iodide show longer relaxation time as shown in (Figure 5.48 yellow line) , passing from 10 ns to hundreds of ns. This effect could be hypothesize as probably induced by increasing in order with this cation. While relaxation time for C_5F_7ImMet around 10ns (Figure 5.48 green line) was similar to perfluoroalkyl compounds.
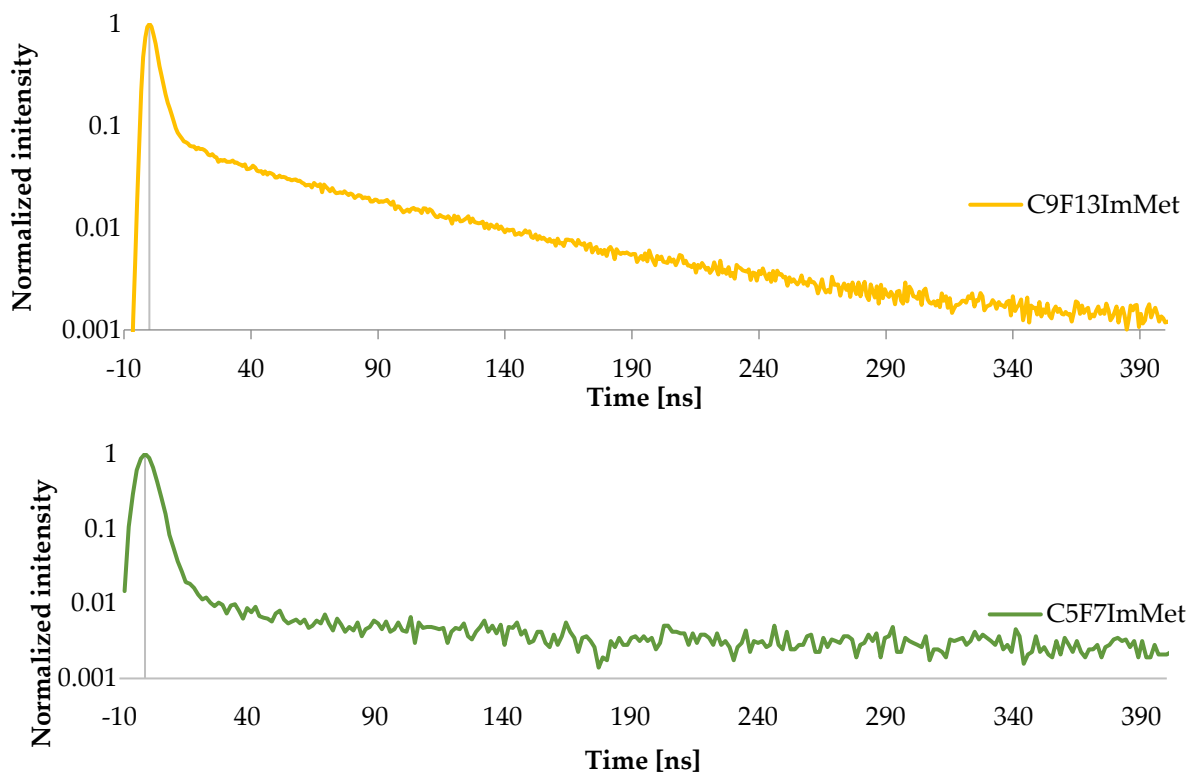
Figure 5.48. Relaxation time for C_2ImMet, C_9F_{13}ImMet and C_5F_7ImMet lead iodides

So, characterization of perfluoroalkyl-methyl imidazolium perovskite gives some differences in PL spectra in terms of signal (shape and wavelength). These effects could be probably related to different organization and distortion of lead iodide sublattice induced by these cations. For perfluoroalkyl imidazolium perovskites these results must have to be integrated with further study of crystalline structure to better understand exciton behavior.

6.   Conclusion of the work

In this work new lead iodide perovskites containing imidazolium cations decorated with alkyl or perfluoroalkyl chains of different length were synthetized and characterized. Single crystal structure of $(C_2ImMet)PbI_3$ and $(C_3ImMet)PbI_3$ shows 1D face sharing lead iodide perovskite, confirming the same structure of their lead bromides counterparts. Analysis of available PXRD data of imidazolium lead halide with results of this work allows to correlate the effect of alkyl chain length on crystal structure. In the case of perovskites prepared with other CmImMet cations (with m>3), single crystal structures were not resolved, due to the increasing disorder induced by longer chains. However, FTIR analyses confirm perovskite formation. Moreover, PXRD patterns similar to their lead bromide counterpart, suggest a 1D structure also for HPs containing imidazolium with longer alkyl chains This is in good agreement with optical characterization, showing   broad emission typical of 1D structure.

Perovskites containing perfluoroalkyl imidazolium cations show considerable differences both in XRD diffraction patterns (with peaks at lower angles) and photoluminescence spectra, with a sharper peak and PL signal shifted at lower wavelengths. Moreover, using $C_9F_{13}ImMet$, as cation allows to obtain a perovskite with liquid crystalline behavior. Interestingly the starting $C_9F_{13}ImMet$ iodide is a thermotropic liquid crystal with smectic phase and the same behavior is preserved also upon incorporation into perovskite lattice, as proven from DSC and polarized optical microscopy. Formation of a Smectic A phase was observed at 144°C with transition to isotropic liquid at 236°C. Moreover, Perovskite with $C_9F_{13}ImMet$ PL intensity is higher than $C_9F_{13}ImMet$ and long alkyl chains imidazolium perovksites. These two effects suggests that *fluorous-fluorous* interactions and the tendency to segregation of perfluoroalkyl chains could promote the formation of ordered structures in low-dimensional perovskites. Moreover, contact angle measures show a hydrophobic behavior induced by these materials, providing interesting properties in terms of moisture resistance of these perovskite.

6.1   Future steps

Perfluoroalkyl imidazolium perovskite must be better characterized in terms of solid-state NMR and single crystal XRD to understand better its crystalline structure.

Future research on low dimensional perovskites must consider these results, in particular the effect of fluorinated chains with different cations inside perovskite

lattice in terms of crystal structure and properties. These perovskites can be further investigated in terms of dielectric constant and conductivity to understand how these properties are influenced by these structures. Given the limits of using these perovskite as emitting materials new studies about perfluoroalkyl functionalized aromatic cations can be carried out to improve their photoluminescence for future applications. Perfluoroalkyl chain effect can be exploited to tune order and distortion inside perovskites. Moreover, these results open a new research strand about the use of perovskite as thermotropic liquid crystals, with study about optimization of these materials and their application in optoelectronic or electronic field, for example as polarized light detectors. In addition, use of fluorinated chains should be taken into account for their improvement in hydrophobic behavior of perovskites. Finally, stability tests must be performed also on future optoelectronic devices to evaluate this effect.

Bibliography

References

[1] G. Wu *et al*, *ACS Energy Lett.*, vol. 3, pp. 1443, 2018.

[2] P. Gao, M. Grätzel and M. K. Nazeeruddin, "Organohalide lead perovskites for photovoltaic applications," *Energy Environ. Sci.*, vol. 7, *(8)*, pp. 2448-2463, 2014.

[3] E. Mosconi *et al*, "First-Principles Modeling of Mixed Halide Organometal Perovskites for Photovoltaic Applications," *J. Phys. Chem. C*, vol. 117, *(27)*, pp. 13902-13913, 07/11, 2013.

[4] W. Ke and M. G. Kanatzidis, "Prospects for low-toxicity lead-free perovskite solar cells," *Nature Communications*, vol. 10, *(1)*, pp. 965, 02/27, 2019.

[5] M. S. Ozório *et al*, "The role of the A-cations in the polymorphic stability and optoelectronic properties of lead-free ASnI3 perovskites," *Phys. Chem. Chem. Phys.*, vol. 23, *(3)*, pp. 2286-2297, 2021.

[6] V. M. Goldschmidt, "Die Gesetze der Krystallochemie," *Naturwissenschaften*, vol. 14, *(21)*, pp. 477-485, 05/01, 1926.

[7] Y. Liu, Z. Yang and S. (. Liu, "Recent Progress in Single-Crystalline Perovskite Research Including Crystal Preparation, Property Evaluation, and Applications," *Adv. Sci.*, vol. 5, *(1)*, pp. 1700471, 01/01; 2021/11, 2018.

[8] A. K. Jena, A. Kulkarni and T. Miyasaka, "Halide Perovskite Photovoltaics: Background, Status, and Future Prospects," *Chem. Rev.*, vol. 119, *(5)*, pp. 3036-3103, 03/13, 2019.

[9] D. B. Mitzi, "Templating and structural engineering in organic–inorganic perovskites," *J. Chem. Soc. , Dalton Trans.*, *(1)*, pp. 1-12, 2001.

128   Errore. Per applicare Heading 1 al testo
                                              da visualizzare in questo punto,
                                              utilizzare la scheda Home.

[10] H. Kim, S. H. Im and N. Park, "Organolead Halide Perovskite: New Horizons in Solar Cell Research," *J. Phys. Chem. C,* vol. 118, *(11),* pp. 5615-5625, 03/20, 2014.

[11] Y. H. Chang, C. H. Park and K. Matsuishi, "First-principles study of the structural and the electronic properties of the lead-halide-based inorganic-organic perovskites (CH 3NH 3)PbX 3 and CsPbX 3 (X = Cl, Br, I)," *Journal of the Korean Physical Society,* vol. 44, pp. 889-893, 04/01, 2004.

[12] R. Prasanna *et al,* "Band Gap Tuning via Lattice Contraction and Octahedral Tilting in Perovskite Materials for Photovoltaics," *J. Am. Chem. Soc.,* vol. 139, *(32),* pp. 11117-11124, 08/16, 2017.

[13] J. Lee *et al,* "Resolving the Physical Origin of Octahedral Tilting in Halide Perovskites," *Chem. Mater.,* vol. 28, *(12),* pp. 4259-4266, 06/28, 2016.

[14] E. L. Unger *et al,* "Roadmap and roadblocks for the band gap tunability of metal halide perovskites," *J. Mater. Chem. A,* vol. 5, *(23),* pp. 11401-11409, 2017.

[15] G. Kim and A. Petrozza, "Defect Tolerance and Intolerance in Metal-Halide Perovskites," *Adv. Energy Mater.,* vol. 10, *(37),* pp. 2001959, 10/01; 2021/12, 2020.

[16] R. E. Brandt *et al,* "Searching for "Defect-Tolerant" Photovoltaic Materials: Combined Theoretical and Experimental Screening," *Chem. Mater.,* vol. 29, *(11),* pp. 4667-4674, 06/13, 2017.

[17] K. Ji *et al,* "Halide Perovskite Light-Emitting Diode Technologies," *Adv. Optical Mater.,* vol. 9, *(18),* pp. 2002128, 09/01; 2021/12, 2021.

[18] K. Zhang *et al,* "Opportunities and challenges in perovskite LED commercialization," *J. Mater. Chem. C,* vol. 9, *(11),* pp. 3795-3799, 2021.

[19] X. Liu *et al,* "Metal halide perovskites for light-emitting diodes," *Nature Materials,* vol. 20, *(1),* pp. 10-21, 01/01, 2021.

[20] J. Lu *et al,* "Lead-free metal halide perovskites for light-emitting diodes," *EcoMat,* vol. 3, *(2),* pp. e12082, 04/01; 2021/12, 2021.

[21] M. Worku *et al,* "Optically pumped white light-emitting diodes based on metal halide perovskites and perovskite-related materials," *APL Materials,* vol. 8, *(1),* pp. 010902, 01/01; 2021/12, 2020.

Errore. Per applicare Heading 1 al testo da   129
visualizzare in questo punto, utilizzare la
scheda Home.

[22] Y. Wei, Z. Cheng and J. Lin, "An overview on enhancing the stability of lead halide perovskite quantum dots and their applications in phosphor-converted LEDs," *Chem. Soc. Rev.,* vol. 48, *(1),* pp. 310-350, 2019.

[23] L. Protesescu *et al*, "Nanocrystals of Cesium Lead Halide Perovskites (CsPbX3, X = Cl, Br, and I): Novel Optoelectronic Materials Showing Bright Emission with Wide Color Gamut," *Nano Lett.,* vol. 15, *(6),* pp. 3692-3696, 06/10, 2015.

[24] R. L. Z. Hoye *et al*, "Light emission from perovskite materials," *APL Materials,* vol. 8, *(7),* pp. 070401, 07/01; 2021/12, 2020.

[25] P. Roy *et al*, "A review on perovskite solar cells: Evolution of architecture, fabrication techniques, commercialization issues and status," *Solar Energy,* vol. 198, pp. 665-688, 2020.

[26] H. Shen *et al*, "Mechanically-stacked perovskite/CIGS tandem solar cells with efficiency of 23.9% and reduced oxygen sensitivity," *Energy Environ. Sci.,* vol. 11, *(2),* pp. 394-406, 2018.

[27] F. Fu *et al*, "High-efficiency inverted semi-transparent planar perovskite solar cells in substrate configuration," *Nature Energy,* vol. 2, *(1),* pp. 16190, 12/19, 2016.

[28] J. H. Noh *et al*, "Chemical Management for Colorful, Efficient, and Stable Inorganic–Organic Hybrid Nanostructured Solar Cells," *Nano Lett.,* vol. 13, *(4),* pp. 1764-1769, 04/10, 2013.

[29] H. Wang *et al*, "Low-Dimensional Metal Halide Perovskite Photodetectors," *Adv Mater,* vol. 33, *(7),* pp. 2003309, 02/01; 2021/12, 2021.

[30] P. Zhu and J. Zhu, "Low-dimensional metal halide perovskites and related optoelectronic applications," *InfoMat,* vol. 2, *(2),* pp. 341-378, 03/01; 2021/11, 2020.

[31] D. Jeong, J. Yang and N. Park, "Roadmap on halide perovskite and related devices," *Nanotechnology,* vol. 31, 11/21, 2019.

[32] L. Lanzetta *et al*, "Degradation mechanism of hybrid tin-based perovskite solar cells and the critical role of tin (IV) iodide," *Nature Communications,* vol. 12, *(1),* pp. 2853, 05/14, 2021.

130   Errore. Per applicare Heading 1 al testo
                                                      da visualizzare in questo punto,
                                                      utilizzare la scheda Home.

[33] A. F. Akbulatov *et al*, "Light or Heat: What Is Killing Lead Halide Perovskites under Solar Cell Operation Conditions?" *J. Phys. Chem. Lett.,* vol. 11, *(1),* pp. 333-339, 01/02, 2020.

[34] A. M. A. Leguy *et al*, "Reversible Hydration of CH3NH3PbI3 in Films, Single Crystals, and Solar Cells," *Chem. Mater.,* vol. 27, *(9),* pp. 3397-3407, 05/12, 2015.

[35] J. M. Frost *et al*, "Atomistic Origins of High-Performance in Hybrid Halide Perovskite Solar Cells," *Nano Lett.,* vol. 14, *(5),* pp. 2584-2590, 05/14, 2014.

[36] N. Aristidou *et al*, "Fast oxygen diffusion and iodide defects mediate oxygen-induced degradation of perovskite solar cells," *Nature Communications,* vol. 8, *(1),* pp. 15218, 05/11, 2017.

[37] B. Chen *et al*, "Imperfections and their passivation in halide perovskite solar cells," *Chem. Soc. Rev.,* vol. 48, *(14),* pp. 3842-3867, 2019.

[38] M. Zhu *et al*, "Interaction engineering in organic–inorganic hybrid perovskite solar cells," *Mater. Horiz.,* vol. 7, *(9),* pp. 2208-2236, 2020.

[39] Y. Guo *et al*, "Phenylalkylammonium passivation enables perovskite light emitting diodes with record high-radiance operational lifetime: the chain length matters," *Nature Communications,* vol. 12, *(1),* pp. 644, 01/28, 2021.

[40] N. K. Noel *et al*, "Enhanced Photoluminescence and Solar Cell Performance via Lewis Base Passivation of Organic–Inorganic Lead Halide Perovskites," *ACS Nano,* vol. 8, *(10),* pp. 9815-9821, 10/28, 2014.

[41] X. Zheng *et al*, "Dual Functions of Crystallization Control and Defect Passivation Enabled by Sulfonic Zwitterions for Stable and Efficient Perovskite Solar Cells," *Adv Mater,* vol. 30, *(52),* pp. 1803428, 12/01; 2022/01, 2018.

[42] G. Cavallo *et al*, "The Halogen Bond," *Chem. Rev.,* vol. 116, *(4),* pp. 2478-2601, 02/24, 2016.

[43] A. Abate *et al*, "Supramolecular Halogen Bond Passivation of Organic–Inorganic Halide Perovskite Solar Cells," *Nano Lett.,* vol. 14, *(6),* pp. 3247-3254, 06/11, 2014.

[44] C. M. Wolff *et al*, "Perfluorinated Self-Assembled Monolayers Enhance the Stability and Efficiency of Inverted Perovskite Solar Cells," *ACS Nano,* vol. 14, *(2),* pp. 1445-1456, 02/25, 2020.

Errore. Per applicare Heading 1 al testo da   131
visualizzare in questo punto, utilizzare la
scheda Home.

[45] L. Zhang and Y. Chen, "Atomistic Understanding on Molecular Halide Perovskite/Organic/TiO2 Interface with Bifunctional Interfacial Modifier: A Case Study on Halogen Bond and Carboxylic Acid Group," *Appl. Surf. Sci.,* vol. 502, pp. 144274, 10/01, 2019.

[46] J. Kundu and D. K. Das, "Low Dimensional, Broadband, Luminescent Organic-Inorganic Hybrid Materials for Lighting Applications," *Eur. J. Inorg. Chem.,* vol. n/a, 08/30; 2021/10, 2021.

[47] O. Weber *et al*, "Structural diversity in hybrid organic–inorganic lead iodide materials," *Acta Crystallographica Section B Structural Science, Crystal Engineering and Materials,* vol. 71, pp. 668-678, 12/01, 2015.

[48] H. Lin *et al*, "Low-Dimensional Organometal Halide Perovskites," *ACS Energy Letters,* vol. 3, pp. 54-62, 01/12, 2018.

[49] X. Li, J. M. Hoffman and M. G. Kanatzidis, "The 2D Halide Perovskite Rulebook: How the Spacer Influences Everything from the Structure to Optoelectronic Device Efficiency," *Chem. Rev.,* vol. 121, *(4),* pp. 2230-2291, 02/24, 2021.

[50] F. Zhang *et al*, "Advances in two-dimensional organic–inorganic hybrid perovskites," *Energy Environ. Sci.,* vol. 13, *(4),* pp. 1154-1186, 2020.

[51] B. Febriansyah *et al*, "Targeted Synthesis of Trimeric Organic–Bromoplumbate Hybrids That Display Intrinsic, Highly Stokes-Shifted, Broadband Emission," *Chem. Mater.,* vol. 32, *(11),* pp. 4431-4441, 06/09, 2020.

[52] J. Jin *et al*, "Photoluminescent ionic metal halides based on s2 typed ions and aprotic ionic liquid cations," *Coord. Chem. Rev.,* vol. 448, pp. 214185, 2021.

[53] N. I. Selivanov *et al*, "Pyridinium lead tribromide and pyridinium lead triiodide: quasi-one-dimensional perovskites with an optically active aromatic π-system," *Dalton Trans.,* vol. 47, *(45),* pp. 16313-16319, 2018.

[54] J. Zhao *et al*, "Systematic Approach of One-Dimensional Lead Perovskites with Face-Sharing Connectivity to Realize Efficient and Tunable Broadband Light Emission," *J. Phys. Chem. C,* vol. 125, *(20),* pp. 10850-10859, 05/27, 2021.

[55] Y. Guo and P. Lightfoot, "Structural Diversity of Lead Halide Chain Compounds, APbX3, Templated by Isomeric Molecular Cations," *Dalton Transactions,* vol. 49, 08/27, 2020.

132   Errore. Per applicare Heading 1 al testo
                                         da visualizzare in questo punto,
                                         utilizzare la scheda Home.

[56] M. Li and Z. Xia, "Recent progress of zero-dimensional luminescent metal halides," *Chem. Soc. Rev.*, vol. 50, *(4)*, pp. 2626-2662, 2021.

[57] L. Zhang *et al*, "Ultra-long photoluminescence lifetime in an inorganic halide perovskite thin film," *J. Mater. Chem. A*, vol. 7, *(39)*, pp. 22229-22234, 2019.

[58] N. I. Selivanov *et al*, "The effect of organic cations on the electronic, optical and luminescence properties of 1D piperidinium, pyridinium, and 3-hydroxypyridinium lead trihalides," *Dalton Trans.*, vol. 49, *(14)*, pp. 4390-4403, 2020.

[59] M. D. Smith *et al*, "Structural origins of broadband emission from layered Pb–Br hybrid perovskites," *Chem. Sci.*, vol. 8, *(6)*, pp. 4497-4504, 2017.

[60] M. Shi *et al*, "A hybrid molecular rotor crystal with dielectric relaxation and thermochromic luminescence," *J. Mol. Struct.*, vol. 1206, pp. 127650, 2020.

[61] S. Yu *et al*, "Crystal structural and thermochromic luminescence properties modulation by ion liquid cations in bromoplumbate perovskites," *Inorganic Chemistry Communications*, vol. 112, pp. 107690, 2020.

[62] K. Wan *et al*, "Investigation of thermochromic photoluminescent, dielectric and crystal structural properties for an inorganic–organic hybrid solid of [1-hexyl-3-methylimidazolium][PbBr3]," *New J. Chem.*, vol. 40, *(10)*, pp. 8664-8672, 2016.

[63] T. H. Duong, S. Nobusue and H. Tada, "Preparation of perovskite-derived one dimensional single crystals based on edge-shared octahedrons with pyridine derivatives," *J. Cryst. Growth*, vol. 537, pp. 125577, 2020

[64] R. Kevorkyants, N. I. Selivanov and A. V. Emeline, "Modulating electronic properties of pyridinium lead halide perovskites via fluorinated methyl substituents," *Mater. Chem. Phys.*, vol. 273, pp. 125139, 2021.

[65] C. Lermer *et al*, "Benzimidazolium Lead Halide Perovskites: Effects of Anion Substitution and Dimensionality on the Bandgap," *Z. Anorg. Allg. Chem.*, vol. 642, *(23)*, pp. 1369-1376, 12/01; 2021/08, 2016.

[66] M. Tremblay *et al*, "Structures of (4-Y-C6H4CH2NH3)2PbI4 {Y = H, F, Cl, Br, I}: Tuning of Hybrid Organic Inorganic Perovskite Structures from Ruddlesden–Popper to Dion–Jacobson Limits," *Chem. Mater.*, vol. 31, *(16)*, pp. 6145-6153, 08/27, 2019.

Errore. Per applicare Heading 1 al testo da
visualizzare in questo punto, utilizzare la
scheda Home.

133

[67] J. Hu *et al*, "Aryl-Perfluoroaryl Interaction in Two-Dimensional Organic–Inorganic Hybrid Perovskites Boosts Stability and Photovoltaic Efficiency," *ACS Materials Lett.*, vol. 1, *(1)*, pp. 171-176, 07/01, 2019.

[68] I. García-Benito *et al*, "Fluorination of Organic Spacer Impacts on the Structural and Optical Response of 2D Perovskites," *Frontiers in Chemistry*, vol. 7, 2020.

[69] L. Wang *et al*, "A guide to use fluorinated aromatic bulky cations for stable and high-performance 2D/3D perovskite solar cells: The more fluorination the better?" *Journal of Energy Chemistry*, vol. 64, pp. 179-189, 2022.

[70] C. C. Stoumpos and M. G. Kanatzidis, "The Renaissance of Halide Perovskites and Their Evolution as Emerging Semiconductors," *Acc. Chem. Res.*, vol. 48, *(10)*, pp. 2791-2802, 10/20, 2015.

[71] X. Li *et al*, "Enhancing the Photovoltaic Performance and Moisture Stability of Perovskite Solar Cells Via Polyfluoroalkylated Imidazolium Additives," *ACS Appl. Mater. Interfaces*, vol. 13, *(3)*, pp. 4553-4559, 01/27, 2021.

[72] A. Trigui *et al*, "**The one-dimensional organic–inorganic hybrid: *catena*-poly[bis-[1-(3-ammoniopropyl)-1*H*-imidazolium] [[iodidoplumbate(II)]-tri-μ-iodido-plumbate(II)-tri-μ-iodido-[iodidoplumbate(II)]-di-μ-iodido]]**," *Acta Crystallographica Section E*, vol. 67, *(4)*, pp. 458-459, 2011.

[73] L. N. Quan *et al*, "Ligand-Stabilized Reduced-Dimensionality Perovskites," *J. Am. Chem. Soc.*, vol. 138, *(8)*, pp. 2649-2655, 03/02, 2016.

[74] C. Zhou *et al*, "Low dimensional metal halide perovskites and hybrids," *Materials Science and Engineering: R: Reports*, vol. 137, pp. 38-65, 2019.

[75] J. S. Manser, J. A. Christians and P. V. Kamat, "Intriguing Optoelectronic Properties of Metal Halide Perovskites," *Chem. Rev.*, vol. 116, *(21)*, pp. 12956-13008, 11/09, 2016.

[76] C. Katan *et al*, "Interplay of spin–orbit coupling and lattice distortion in metal substituted 3D tri-chloride hybrid perovskites," *J. Mater. Chem. A*, vol. 3, *(17)*, pp. 9232-9240, 2015.

[77] L. Mao *et al*, "Tunable White-Light Emission in Single-Cation-Templated Three-Layered 2D Perovskites (CH3CH2NH3)4Pb3Br10–xClx," *J. Am. Chem. Soc.*, vol. 139, *(34)*, pp. 11956-11963, 08/30, 2017.

134   Errore. Per applicare Heading 1 al testo
da visualizzare in questo punto,
utilizzare la scheda Home.

[78] C. Ortiz-Cervantes, P. Carmona-Monroy and D. Solis-Ibarra, "Two-Dimensional Halide Perovskites in Solar Cells: 2D or not 2D?" *ChemSusChem,* vol. 12, *(8),* pp. 1560-1575, 04/23; 2022/01, 2019.

[79] M. D. Smith and H. I. Karunadasa, "White-Light Emission from Layered Halide Perovskites," *Acc. Chem. Res.,* vol. 51, *(3),* pp. 619-627, 03/20, 2018.

[80] R. Gautier, M. Paris and F. Massuyeau, "Exciton Self-Trapping in Hybrid Lead Halides: Role of Halogen," *J. Am. Chem. Soc.,* vol. 141, *(32),* pp. 12619-12623, 08/14, 2019.

[81] A. Biswas *et al*, "Efficient Broad-Band Emission from Contorted Purely Corner-Shared One Dimensional (1D) Organic Lead Halide Perovskite," *Chem. Mater.,* vol. 31, *(7),* pp. 2253-2257, 04/09, 2019.

[82] Z. Qi *et al*, "Highly efficient self-trapped exciton emission in a one-dimensional face-shared hybrid lead bromide," *Chem. Commun.,* vol. 57, *(20),* pp. 2495-2498, 2021.

[83] G. Zhou *et al*, "Broad-band emission in metal halide perovskites: Mechanism, materials, and applications," *Materials Science and Engineering: R: Reports,* vol. 141, pp. 100548, 2020.

[84] M. Z. Rahaman *et al*, "One-Dimensional Molecular Metal Halide Materials: Structures, Properties, and Applications," *Small Struct.,* vol. 2, *(4),* pp. 2000062, 04/01; 2021/09, 2021.

[85] Y. Guo, L. Yang and P. Lightfoot, "Three New Lead Iodide Chain Compounds, APbI3, Templated by Molecular Cations," *Crystals,* vol. 9, *(12),* 2019. lead halideshybrid perovskitescrystal structure.

[86] L. Mao *et al*, "Structural Diversity in White-Light-Emitting Hybrid Lead Bromide Perovskites," *J. Am. Chem. Soc.,* vol. 140, *(40),* pp. 13078-13088, 10/10, 2018.

[87] Y. Wang *et al*, "Reaching 90% Photoluminescence Quantum Yield in One-Dimensional Metal Halide C4N2H14PbBr4 by Pressure-Suppressed Nonradiative Loss," *J. Am. Chem. Soc.,* vol. 142, *(37),* pp. 16001-16006, 09/16, 2020.

[88] F. Zhang *et al*, "Enhanced Charge Transport in 2D Perovskites via Fluorination of Organic Cation," *J. Am. Chem. Soc.,* vol. 141, *(14),* pp. 5972-5979, 04/10, 2019.

[89] H. Zhang *et al*, "Two-Dimensional Hybrid Perovskite Ferroelectric Induced by Perfluorinated Substitution," *J. Am. Chem. Soc.,* vol. 142, *(47),* pp. 20208-20215, 11/25, 2020.

[90] P. Shi *et al*, "Two-Dimensional Organic–Inorganic Perovskite Ferroelectric Semiconductors with Fluorinated Aromatic Spacers," *J. Am. Chem. Soc.,* vol. 141, *(45),* pp. 18334-18340, 11/13, 2019.

[91] M. Ruiz-Preciado *et al*, "Supramolecular Modulation of Hybrid Perovskite Solar Cells via Bifunctional Halogen Bonding Revealed by Two-Dimensional 19F Solid-State NMR Spectroscopy," *J. Am. Chem. Soc.,* vol. 142, *(3),* pp. 1645-1654, 01/22, 2020.

[92] I. García-Benito *et al*, "Fashioning Fluorous Organic Spacers for Tunable and Stable Layered Hybrid Perovskites," *Chem. Mater.,* vol. 30, *(22),* pp. 8211-8220, 11/27, 2018.

[93] M. E. Kamminga *et al*, "The Role of Connectivity on Electronic Properties of Lead Iodide Perovskite-Derived Compounds," *Inorg. Chem.,* vol. 56, *(14),* pp. 8408-8414, 07/17, 2017.

[94] Q. Wang *et al*, "Enhancing efficiency of perovskite solar cells by reducing defects through imidazolium cation incorporation," *Materials Today Energy,* vol. 7, pp. 161-168, 2018.

[95] X. Wang *et al*, "Atomistic Mechanism of Broadband Emission in Metal Halide Perovskites," *J. Phys. Chem. Lett.,* vol. 10, *(3),* pp. 501-506, 02/07, 2019.

[96] C. Seth *et al*, "One-Dimensional Behavior of Imidazolium Lead Iodide," *J. Phys. Chem. C,* vol. 123, *(26),* pp. 16449-16455, 07/05, 2019.

[97] X. Sun *et al*, "Combining Dual-Light Emissions to Achieve Efficient Broadband Yellowish-Green Luminescence in One-Dimensional Hybrid Lead Halides," *Inorg. Chem.,* vol. 60, *(3),* pp. 1491-1498, 02/01, 2021.

[98] Y. Han, S. Yue and B. Cui, "Low-Dimensional Metal Halide Perovskite Crystal Materials: Structure Strategies and Luminescence Applications," *Adv. Sci.,* vol. 8, *(15),* pp. 2004805, 08/01; 2021/10, 2021.

[99] F. Xu *et al*, "1D Perovskitoid as Absorbing Material for Stable Solar Cells," *Crystals,* vol. 11, *(3),* 2021. perovskite solar cell1D perovskitoidstabilityphotovoltaic materialhydrogen bonds.

136   Errore. Per applicare Heading 1 al testo
da visualizzare in questo punto,
utilizzare la scheda Home.

[100] C. Ma *et al*, "High performance low-dimensional perovskite solar cells based on a one dimensional lead iodide perovskite," *J. Mater. Chem. A,* vol. 7, *(15),* pp. 8811-8817, 2019.

[101] J. Liu *et al*, "Synthesis and optical applications of low dimensional metal-halide perovskites," *Nanotechnology,* vol. 31, 11/21, 2019.

[102] R. Atasiei *et al*, "Investigation of the conduction properties of ionic liquid crystal electrolyte used in dye sensitized solar cells," *Journal of Molecular Liquids,* vol. 267, pp. 81-88, 2018.

[103] N. Yamanaka *et al*, "Ionic liquid crystal as a hole transport layer of dye-sensitized solar cells," *Chem. Commun., (6),* pp. 740-742, 2005.

[104] M. H. Khanmirzaei, S. Ramesh and K. Ramesh, "**Effect of 1-Hexyl-3-Methylimidazolium Iodide Ionic Liquid on Ionic Conductivity and Energy Conversion Efficiency of Solid Polymer Electrolyte-Based Nano-Crystalline Dye-Sensitized Solar Cells**," *Journal of Nanoscience and Nanotechnology,* vol. 20, *(4),* pp. 2423-2429, 2020.

[105] R. Taniki *et al*, "Effects of the polyfluoroalkyl side-chain on the properties of 1-methyl-3-polyfluoroalkylimidazolium fluorohydrogenate ionic liquids," *J. Fluorine Chem.,* vol. 149, pp. 112-118, 2013.

[106] G. Cavallo *et al*, "Tuning of Ionic Liquid Crystal Properties by Combining Halogen Bonding and Fluorous Effect," *ChemPlusChem,* vol. 86, *(3),* pp. 469-474, 03/01; 2022/03, 2021.

[107] S. Yamada *et al*, "Synthesis of perfluoroalkylated pentacenes and evaluation of their fundamental physical properties," *Org. Biomol. Chem.,* vol. 15, *(12),* pp. 2522-2535, 2017.

[108] A. Gabriel Tomulescu *et al*, "Enhancing stability of hybrid perovskite solar cells by imidazolium incorporation," *Solar Energy Mater. Solar Cells,* vol. 227, pp. 111096, 2021.

[109] M. Salado *et al*, "Extending the Lifetime of Perovskite Solar Cells using a Perfluorinated Dopant," *ChemSusChem,* vol. 9, *(18),* pp. 2708-2714, 09/22; 2022/03, 2016.

Errore. Per applicare Heading 1 al testo da
visualizzare in questo punto, utilizzare la
scheda Home.

137

[110] X. Zhu *et al*, "High-Efficiency Perovskite Solar Cells with Imidazolium-Based Ionic Liquid for Surface Passivation and Charge Transport," *Angew. Chem. Int. Ed.,* vol. 60, *(8)*, pp. 4238-4244, 02/19; 2021/11, 2021.

[111] C. Luo *et al*, "Passivation of defects in inverted perovskite solar cells using an imidazolium-based ionic liquid," *Sustainable Energy Fuels,* vol. 4, *(8)*, pp. 3971-3978, 2020.

[112] S. Bai *et al*, "Planar perovskite solar cells with long-term stability using ionic liquid additives," *Nature,* vol. 571, *(7764)*, pp. 245-250, 07/01, 2019.

[113] B. Saparov and D. B. Mitzi, "Organic–Inorganic Perovskites: Structural Versatility for Functional Materials Design," *Chem. Rev.,* vol. 116, *(7)*, pp. 4558-4596, 04/13, 2016.

[114] C. Seth and D. Khushalani, "Non-Perovskite Hybrid Material, Imidazolium Lead Iodide, with Enhanced Stability," *ChemNanoMat,* vol. 5, *(1)*, pp. 85-91, 01/01; 2021/08, 2019.

[115] A. Thirumurugan and C. N. R. Rao, "Supramolecular Organization in Lead Bromide Salts of Imidazolium-Based Ionic Liquids," *Crystal Growth & Design,* vol. 8, *(5)*, pp. 1640-1644, 05/01, 2008.

[116] F. Coleman *et al*, "Lead(ii) chloride ionic liquids and organic/inorganic hybrid materials – a study of chloroplumbate(ii) speciation," *Dalton Trans.,* vol. 42, *(14)*, pp. 5025-5035, 2013.

[117] A. Abate *et al*, "A polyfluoroalkyl imidazolium ionic liquid as iodide ion source in dye sensitized solar cells," *Organic Electronics,* vol. 13, *(11)*, pp. 2474-2478, 2012. .

[118] B. Haddad *et al*, "Influence of methyl and propyl groups on the vibrational spectra of two imidazolium ionic liquids and their non-ionic precursors," *J. Mol. Struct.,* vol. 1134, pp. 582-590, 2017.

[119] I. Jerman *et al*, "Ionic conductivity, infrared and Raman spectroscopic studies of 1-methyl-3-propylimidazolium iodide ionic liquid with added iodine," *Electrochim. Acta,* vol. 53, *(5)*, pp. 2281-2288, 2008.

[120] Y. Jeon *et al*, "Structures of Ionic Liquids with Different Anions Studied by Infrared Vibration Spectroscopy," *J Phys Chem B,* vol. 112, *(15)*, pp. 4735-4740, 04/01, 2008.

138   Errore. Per applicare Heading 1 al testo
                                                  da visualizzare in questo punto,
                                                  utilizzare la scheda Home.

[121] W. Yang *et al*, "Surface and mechanical properties of waterborne polyurethane films reinforced by hydroxyl-terminated poly(fluoroalkyl methacrylates)," *Polymer,* vol. 133, pp. 68-77, 2017.

[122] G. Socrates, ***Infrared and Raman Characteristic Group Frequencies: Tables and Charts*.** (3rd ed.) Chichester, West Sussex PO19 IUD, England: JOHN WILEY & SONS, LTD, 2001.

[123] A. Abate *et al*, "Anisotropic ionic conductivity in fluorinated ionic liquid crystals suitable for optoelectronic applications," *J. Mater. Chem. A,* vol. 1, *(22),* pp. 6572-6578, 2013.

[124] L. Dimesso *et al*, "Investigation of formamidinium and guanidinium lead tri-iodide powders as precursors for solar cells," *Materials Science and Engineering: B,* vol. 204, 2015.

[125] M. Acik *et al*, "Substitutional Growth of Methylammonium Lead Iodide Perovskites in Alcohols," *Advanced Energy Materials,* vol. 8, pp. 1701726, 09/29, 2017.

[126] P. Wang, "Lyotropic liquid crystalline phases of anisotropic nanoparticles of organic–inorganic metal halide perovskites: photoluminescence from self-assembled ordered microstructures of semiconductors,"*Chem. Commun.* vol. 57, pp. 5051, 2021.

[127] S. Prathapani *et al*, "Experimental evaluation of room temperature crystallization and phase evolution of hybrid perovskite materials," *CrystEngComm,* vol. 19, *(27),* pp. 3834-3843, 2017.

[128] Z. Jian and W. Hejing, "The physical meanings of 5 basic parameters for an X-ray diffraction peak and their application," *Chinese Journal of Geochemistry,* vol. 22, *(1),* pp. 38-44, 01/01, 2003.

[129] G. P. Nagabhushana et al., "Direct calorimetric verification of thermodynamic instability of lead halide hybrid perovskites," *Proceedings of the National Academy of Sciences,* vol. 113, *(28),* pp. 7717-7721, 07/12; 2022/04, 2016.

[130] L. Zhao *et al*, "Thermal Management Enables Bright and Stable Perovskite Light-Emitting Diodes," *Adv Mater,* vol. 32, *(25),* pp. 2000752, 06/01; 2022/03, 2020.

[131] Michael Yoshpe (2022). Distance between straight lines in 3D (https://www.mathworks.com/matlabcentral/fileexchange/55911-distance-between-straight-lines-in-3d), MATLAB Central File Exchange. Retrieved April 11, 2022.

List of Figures

List of Tables

A. Appendix A

Table A.1 Crystal data and structure refinement for C2ImMet(PbI3) and C3ImMet(PbI3)

Identification code	C$_2$ImMet(PbI$_3$)	C$_3$ImMet(PbI$_3$)
Empirical formula	C$_6$H$_{11}$I$_3$N$_2$Pb	C$_{14}$H$_{26}$I$_6$N$_4$Pb$_2$
Formula weight	699.098	1426.25
Temperature/K	296.15	296.15
Crystal system	orthorhombic	monoclinic
Space group	Pbca	P2$_1$/n
a/Å	17.7073(9)	8.1385(8)
b/Å	8.1808(4)	17.9057(16)
c/Å	19.7984(10)	21.422(2)
α/°	90	90
β/°	90	94.724(5)
γ/°	90	90
Volume/Å^3	2868.0(3)	3111.1(5)
Z	8	4
ϱ_{calc}g/cm^3	3.238	3.045
μ/mm^{-1}	18.191	16.773
F(000)	2386.2	2450.2
Crystal size/mm^3	0.1 × 0.12 × 0.24	0.08 × 0.10 × 0.14
Radiation	Mo Kα (λ = 0.71073)	Mo Kα (λ = 0.71073)
2Θ range for data collection/°	5.86 to 59.34	5.22 to 59.56

Index ranges	$-24 \leq h \leq 20$, $-11 \leq k \leq 11$, $-23 \leq l \leq 27$	$-11 \leq h \leq 11$, $-24 \leq k \leq 23$, $-27 \leq l \leq 29$
Reflections collected	28067	31960
Independent reflections	4046 [$R_{int} = 0.0434$, $R_{sigma} = 0.0325$]	8806 [$R_{int} = 0.0461$, $R_{sigma} = 0.0468$]
Data/restraints/parameters	4046/0/111	8806/24/239
Goodness-of-fit on F^2	1.022	1.025
Final R indexes [$I \geq 2\sigma$ (I)]	$R_1 = 0.0365$, $wR_2 = 0.0865$	$R_1 = 0.0427$, $wR_2 = 0.0914$
Final R indexes [all data]	$R_1 = 0.0621$, $wR_2 = 0.0983$	$R_1 = 0.0785$, $wR_2 = 0.1071$
Largest diff. peak/hole / e Å^{-3}	1.49/-2.74	1.79/-2.88

Table A.2. Crystal data and structure refinement for C_8ImMet lead iodide (uncomplete XRD structure)

Identification code	dr49_T1
Empirical formula	$I_{2.5}Pb$
Formula weight	524.478
Temperature/K	296.15
Crystal system	monoclinic
Space group	$P2_1/n$

a/Å	8.1304(6)
b/Å	18.1537(12)
c/Å	20.5976(14)
α/°	90
β/°	97.658(4)
γ/°	90
Volume/Å^3	3013.0(4)
Z	8
ϱ_{calc}g/cm^3	2.312
μ/mm^{-1}	16.259
F(000)	1687.6
Crystal size/mm^3	0.06 x 0.11 x 0.14
Radiation	Mo Kα (λ = 0.71073)
2Θ range for data collection/°	3 to 59.24
Index ranges	-11 ≤ h ≤ 10, -25 ≤ k ≤ 24, -28 ≤ l ≤ 28
Reflections collected	50880
Independent reflections	8453 [R_{int} = 0.0583, R_{sigma} = 0.0556]
Data/restraints/parameters	8453/0/64
Goodness-of-fit on F^2	1.111
Final R indexes [I>=2σ (I)]	R_1 = 0.0744, wR_2 = 0.2819
Final R indexes [all data]	R_1 = 0.1307, wR_2 = 0.3280
Largest diff. peak/hole / e Å^{-3}	7.28/-3.23

B.   Appendix B

Distance among lead halide chains from crystallographic data obtained from Mercury were obtained with following method (centroid distance was not always possible due to staggered chains in some cases):

1. Selection of unit cell from mercury and file exported as .xyz
2. Filtered coordinates data of lead atoms (as approximation we considered lead atom distances as first approximation for lead halide chains)
3. Creation PB1 matrix 3xn (n number of lead atoms)
4. Application of clustering technique with matlab, with clusterdata function:
   T1 = clusterdata(PB1 ,n);
   where n is the number of expected lead halide chains, this hirearchical clustering technique use ward method. This method it is used for point in 3D space, as shown in Figura B.1. [131]
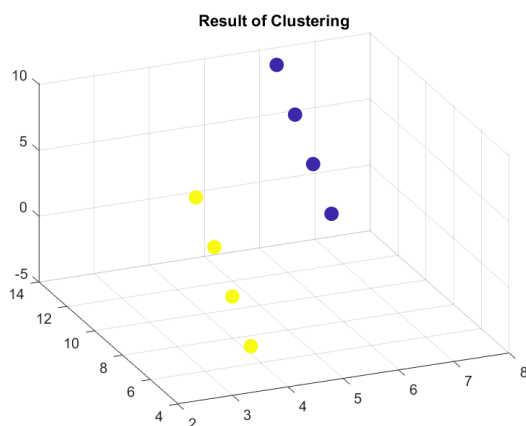

Figura B.1 First cluster of data used for C3ImMetPbBr

5. For each cluster line passing among two points was evaluated selecting two random points or points at the edges (Figura B.2) Normalized vector of every straight line was recorded to check parallel lines.
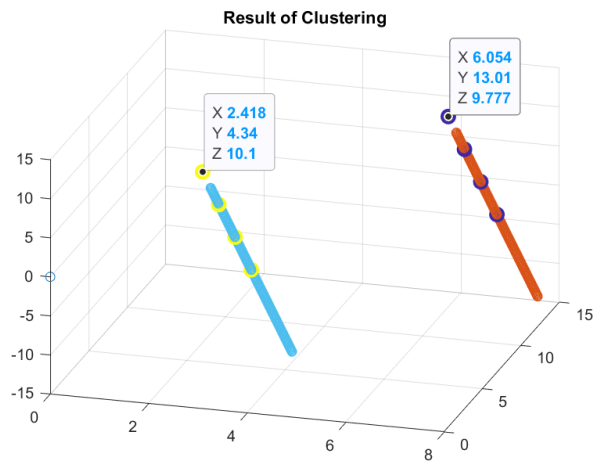
Figura B.2. Line obtained in 3D

6. After this operation for every cluster, distance between two lines was obtained through 3D-line distance algorithm [133]

2. Acknowledgements

A special thanks to my supervisor Prof. Gabriella Cavallo for her unvaluable contribution to this thesis. I would like to thank to Prof. Federico Bella who accepted to be my co-advisor.

I wish to extend my special thanks to my colleague Alessandra, who accompanied me in this work and all other "thesis" student: Alessandra, Christian, Elisa, Simona, Edoardo and Giorgio.

A special thanks to all SBN lab group that give me the possibility to develop my thesis in their laboratory. A particular thanks to prof. Giancarlo Terraneo for his contribution in XRD analysis, prof. Pierangelo Metrangolo with his intuitions and feedbacks and Maurizio Ursini, with his advice, practical helps, and expertise.

I would like to thank all doctorate students of SBN lab, in particular the contribution of Alessandro, Eleonora, Marta, Pietro and Beatrice.

The assistance for photophysical characterization provided by Dott. Valerio Pinchetti, Matteo Zaffalon and Prof. Sergio Brovelli from University of Milano Bicocca was greatly appreciated.

A special thanks to my family who supported and helped me during these years: my parents and Renato, my brother Michele and my sister Simona also for her help in this work. I wish to thank all my friends and anyone that contribute to this journey.